Generation of Narrowband Photon Pairs at High Brightness within a Hollow-Core Fiber

Erzeugung schmalbandiger Photonenpaare mit hoher Rate innerhalb einer Hohlkernfaser
Dissertation von Alexander Bruns, Juni 2023

TECHNISCHE
UNIVERSITÄT
DARMSTADT

Fachbereich Physik
Institut für Angewandte Physik
Nichtlineare Optik / Quantenoptik

Generation of Narrowband Photon Pairs at High Brightness within a Hollow-Core Fiber

Vom Fachbereich Physik
der Technischen Universität Darmstadt

zur Erlangung des Grades
eines Doktors der Naturwissenschaften
(Dr. rer. nat.)

genehmigte Dissertation von
M.Sc. Alexander Bruns
aus Nastätten

Referent: Prof. Dr. Thomas Halfmann
Korreferent: Prof. Dr. Markus Gräfe

Tag der Einreichung: 16. Juni 2023
Tag der Prüfung: 5. Juli 2023

Darmstadt 2023

Alexander Bruns: Generation of Narrowband Photon Pairs at High Brightness within a Hollow-Core Fiber
Darmstadt, Technische Universität Darmstadt
Jahr der Veröffentlichung der Dissertation auf TUprints: 2023
URN: urn:nbn:de:tuda-tuprints-243805

Tag der mündlichen Prüfung: 05.07.2023

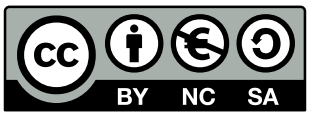

Contents

Introduction **1**

1 Non-Classical Photon Sources for Quantum Information **3**
1.1 Photonic States 4
1.1.1 Two-Mode Squeezed Vacuum 5
1.2 Figures of Merit 7
1.3 Platforms and Protocols 11

2 Photon-Pair Generation via SFWM in an Atomic Ensemble **13**
2.1 Basics and Formalism 13
2.2 Regimes of Photon-Pair Generation 18

3 Cold Rubidium in a Hollow-Core Fiber **20**
3.1 Hollow-Core Photonic Bandgap Fibers 20
3.2 Spectral Properties of Rubidium 22
3.3 Laser Setup 24
3.4 Preparation of Cold Atoms in a Hollow-Core Fiber 26
3.4.1 Magneto-Optical Trapping 26
3.4.2 Transfer of Cold Atoms into the HCPBGF 28
3.5 Characterization of the Medium 33

4 Experimental Implementation of a Photon-Pair Source based on SFWM **38**
4.1 Coupling Scheme and Temporal Sequence 38
4.2 Single Photon Detection 40
4.2.1 Optical Filter Setup 41
4.3 Time-Dependent Normalization in Correlation Measurements . . . 43

5 Generation of Bright and Narrowband Photon Pairs **46**
5.1 Non-Classical and Narrowband Photon Pairs 46
5.1.1 Thermal Photon Statistics of the Individual Fields 48
5.2 Generated Spectral Brightness 50
5.3 Demonstration of Heralding 51
5.3.1 Conditional Auto-Correlation Measurements at Limited Detection Rates 51
5.3.2 Heralding Efficiency 53
5.4 Highest Generated Spectral Brightness per Pump Power 54
5.4.1 Limit of the Spectral Brightness 56
5.4.2 Enhancement of Raman Scattering Rate 58
5.5 Proposed Technical Improvements 59

6 Superfluorescent Emission into a Hollow-Core Fiber **60**
6.1 Experimental Methods for the Observation of SF 61
6.2 Dependence of SF on the Number of Emitters 62

Conclusion and Outlook **65**

Zusammenfassung **67**

A Polarization-Resolved Spatio-Temporal Simulation of SFWM **69**

B Model for the Detected Cross-Correlation **72**

C Model for the Collective Number of Atoms Contributing to Superfluorescence **74**

Bibliography **77**

Publications and Contributions to Conferences **86**

Supervisions and Contributions to Teaching **88**

Introduction

Quantum technologies can exceed the possibilities of classical computation by employing inherently quantum mechanical phenomena [1–3]. In analogy to the classical internet, multiple devices at different remote sites can be interconnected to form a quantum internet [4, 5]. Such a network can, e. g., facilitate inherently secure communication based on quantum key distribution [6]. In optical quantum communication, single photons are used to transfer the quantum information over macroscopic distances. Photons are well suited quantum information carriers due to their easily manipulated internal degrees of freedom. They do not interact with each other and can be well isolated from the environment. Furthermore, they allow fast propagation at the speed of light, and are compatible with established fiber network technology [7].

Consequently, single photon sources are of paramount importance for optical quantum communication [8, 9]. Key requirements for these sources are high single-photon purity and high brightness, which are typically difficult to achieve simultaneously. If these photon sources are to be interfaced with atomic or solid-state quantum memories, spectrally narrow single photons in the MHz regime are required to match the relevant atomic transitions [10]. In the context of quantum networks and moving towards real-life applications [5], the integrability of the technology into optical waveguides becomes crucial [11]. This, e. g., has the advantage of better scalability, lower pump powers, and improved efficiency due to better mode-matching as compared to free-space setups.

While deterministic photon sources include the timing information by design, probabilistic sources require an additional heralding mechanism. It is commonly realized by implementing a probabilistic source of correlated photon pairs and using one of the photons as a herald to obtain timing information about the second photon [10]. Such correlated photon pairs are typically generated by nonlinear optical processes such as spontaneous parametric down-conversion (SPDC) [12] or spontaneous four-wave mixing (SFWM) [13]. SPDC sources are typically implemented in nonlinear crystals and can be operated continuously, but they generate intrinsically broadband photons and, thus, require additional optical cavities in order to achieve narrow photons compatible with atomic transitions [14]. SFWM sources implemented in atomic ensembles can directly generate narrowband photons, though at the cost of technical complexity to prepare the atomic sample. Especially in free-space experiments, the spatial mode matching and overlap with the atomic ensemble can be technically challenging.

In this research project, we implemented the first photon-pair source using SFWM in an ensemble of cold Rubidium atoms confined within a hollow-core fiber [15]. We demonstrate the non-classical nature of the generated photon pairs by measuring a cross-correlation that violates the Cauchy-Schwartz inequality by four standard deviations. Furthermore, when we analyze our source as a heralded single photon source, we observe anti-bunching, i. e., a suppression of the multi-photon component. By using cold atoms we achieve an order of magnitude lower biphoton bandwidth as compared to fibers filled with warm gases [16, 17]. This

was first shown by Corzo *et al.*, who interfaced cold atoms with a nanofiber to generate narrowband single photons on-demand [18]. However, using a hollow-core fiber instead of a nanofiber has the benefit that all light fields, including the pump, are guided in the same optical mode. Thus, we obtain intrinsically optimal mode-matching as well as strong light-atom coupling at orders of magnitude lower pump powers. This results in a generated spectral brightness per pump power of up to $2 \times 10^9\,\mathrm{pairs\,s^{-1}\,MHz^{-1}\,mW^{-1}}$, which is a 10-fold increase over the previous record [19] at 100-fold reduced pump power and 10-fold lower bandwidth of $2\pi\times$ 6.5 MHz, which is directly compatible with atomic quantum memories. Moreover, we show that by tuning the brightness of our source even higher, we reach a fundamental limit of the generated spectral brightness, at which successive photon pairs start to overlap in time. In this regime, the cross-correlation approaches a limit expected for thermal statistics.

This thesis is structured as follows: We begin with a general introduction into non-classical photon sources in Chapter 1 and give an overview over different implementations and platforms to lay out the broader context for our work. Next, in Chapter 2 we introduce SFWM and the corresponding theoretical formalism. In Chapter 3 we introduce the experimental setup and techniques required to prepare cold atoms within a hollow-core fiber while in Chapter 4 we show the details on our implementation of SFWM in such medium. Subsequently, in Chapter 5 we turn to the main results of this work. To characterize our photon-pair source, we present thorough measurements on the cross- and auto-correlations, bandwidth, and brightness of the photon pairs. Where possible, we compare our experimental results to theoretical simulations for a quantitative analysis. Finally, we address current technical limitations and propose future improvements.

In addition to the work on the SFWM photon-pair source, we investigated superfluorescent (SF) scattering in cold atoms within a hollow-core fiber. Under suitable conditions, i. e., a strong coupling between the atoms and weak decoherence, an initially inverted ensemble of emitters can decay collectively and spatially directed at a rate that exceeds the expected one for individual emitters [20–23]. Such collective scattering has been observed in a gas filled hollow-core fiber [24], free-space ensembles of cold Rubidium atoms [25], and individual atoms in the vicinity of a photonic crystal waveguide [26]. In our medium, the strong coupling between light and matter facilitates the cooperative emission and allows us to observe SF at a low number of emitters compared to free-space experiments. Furthermore, by employing an effective two-level system using meta-stable ground states, we can implement an artificial decay rate for the individual emitters via Raman scattering [27]. We can, thus, avoid the limitations typically given by the optical coherence time of the medium. When we determine the effective number of atoms N_{coll} that contribute to the SF process, we observe the expected $\propto N_{\mathrm{coll}}$ dependence for the enhanced SF scattering rate as well as the $\propto N_{\mathrm{coll}}^2$ dependence of the SF intensity. We present these experiments on SF in Chapter 6.

Chapter 1

Non-Classical Photon Sources for Quantum Information

In quantum information, the most fundamental unit of information is a qubit, i. e., the quantum analogon of the classical bit. In general, a qubit is a two-level quantum system whose state can be represented by the superposition

$$|\psi\rangle = \alpha\,|\uparrow\rangle + \beta\,|\downarrow\rangle \tag{1.1}$$

of the two orthogonal basis states $|\uparrow\rangle$ and $|\downarrow\rangle$. To connect separated nodes in the context of quantum networks, the qubit information has to be transported robustly. A qubit moving between different nodes of a quantum network is sometimes termed a flying qubit to distinguish it from stationary qubits, where the later are qubit representations within a localized network node and are typically used to implement quantum gates or to store quantum information. For flying qubits, photons have emerged as the quasi-standard implementation [7]. Alternative approaches such as semiconductor-based flying electron qubits are still in a very early research stage and the expected coherence times are in the regime of nanoseconds only [28].

Photonic qubits can be sent through free space over large distances, though the application for ground based networks is severely limited by the required line-of-sight. Unaffected by this limitation is free-space transmission in between satellites or satellite-ground links [29]. In contrast to that, optical fibers allow technically simple, robust, high-speed, and low-loss transport of photons over macroscopic distances (from meters within one laboratory to continent spanning telecommunication networks). For longer distances in the range of kilometers additional quantum repeaters are required which can be implemented based on quantum memories [30, 31].

For either approach, the state (1.1) has to be imprinted onto the photon. There are various possible encodings, i. e., different physical degrees of freedom of a photon that are used to implement the basis states $|\uparrow\rangle$ and $|\downarrow\rangle$ in. Possible choices include the photons polarization, arrival time (time-bin qubits), spatial mode, or orbital angular momentum [7]. Independent of the specific choice of encoding, we require sources of single photons.

Single photon sources either work deterministic or probabilistic by design. Deterministic sources are based on a single quantum emitter. It is excited by a pumping mechanism and subsequently emits precisely one photon. In contrast to single emitters, probabilistic sources emit photons based on a given photon number probability distribution. They are usually excited very weakly to avoid multi-photon emission, resulting in a high probability to emit no photon at all. As the information about when a photon is generated is crucial for any further use of the source, probabilistic sources require an additional *heralding* mechanism.

Typically, the heralding is realized by generating correlated pairs of photons, also termed *biphotons*. One of the two photons is detected and thus provides the timing information about the creation of the second photon. In this sense, any photon pair source can be interpreted as a heralded source of single photons. We note, that in real life experiments this distinction between deterministic and probabilistic sources is not necessarily a sharp criterion. Real single emitter sources are affected by probabilistic noise and loss mechanisms making them less deterministic while probabilistic sources can be operated in a more deterministic fashion by using, e. g., multiplexing or storage schemes [32, 33].

1.1 Photonic States

To identify what actually defines a suitable photon source for quantum information, we have to look at the photon statistics of the generated fields. Our approach and formalism in this section follows [34] when not stated otherwise.

Number States A single-mode *number* (or *Fock*) state defined as

$$|n\rangle = \frac{\left(\hat{a}_k^\dagger\right)^n}{\sqrt{n!}}|0\rangle \tag{1.2}$$

has the energy eigenvalue $E_n = \hbar\omega_k\left(\hat{a}_k^\dagger\hat{a}_k + \frac{1}{2}\right)$ and describes the quantized electromagnetic field with frequency ω_k in a mode k containing exactly n photons. We identify the photon number operator $\hat{n}_k = \hat{a}_k^\dagger\hat{a}_k$, where $\hat{a}_k$ $\left(\hat{a}_k^\dagger\right)$ is the bosonic annihilation (creation) operator of the mode. An ideal single photon source would generate a field in state $|1\rangle$ on demand, i. e., it deterministically emits a single photon at a chosen time while never emitting undesired noise photons or multiple photons at the same time. Today, such an ideal single photon source does not exist.

Coherent States A laser operating above threshold emits a field that can be described by a *coherent state*

$$|\alpha\rangle = \exp\left(-\frac{1}{2}|\alpha|^2\right)\sum_{n=0}^{\infty}\frac{\alpha^n}{\sqrt{n!}}|n\rangle\,, \tag{1.3}$$

where we used the number states (1.2) as a basis. The parameter α satisfies $\hat{a}\,|\alpha\rangle = \alpha\,|\alpha\rangle$ and is related to the mean photon number $\bar{n} = |\alpha|^2$. The probability to find n photons in the field is given by a Poissonian distribution $P_n = (\bar{n}^n/n!)\cdot \mathrm{e}^{-\bar{n}}$. We calculate P_n for different regimes of $\bar{n}$ in Figure 1.1. The fluctuation in the photon number is given by $\Delta n = \sqrt{\bar{n}}$. The coherent state has symmetric and minimal uncertainties in its quadrature components, it thus describes a quantum state that closely resembles a classical state. We can easily attenuate a laser field to create a coherent state with arbitrary low $\bar{n} \lesssim 1$, i. e., a weak coherent state. However, as illustrated in Figure 1.1, for a negligible probability to generate more than one photon, we obtain only a low probability for $|1\rangle$ and the highest

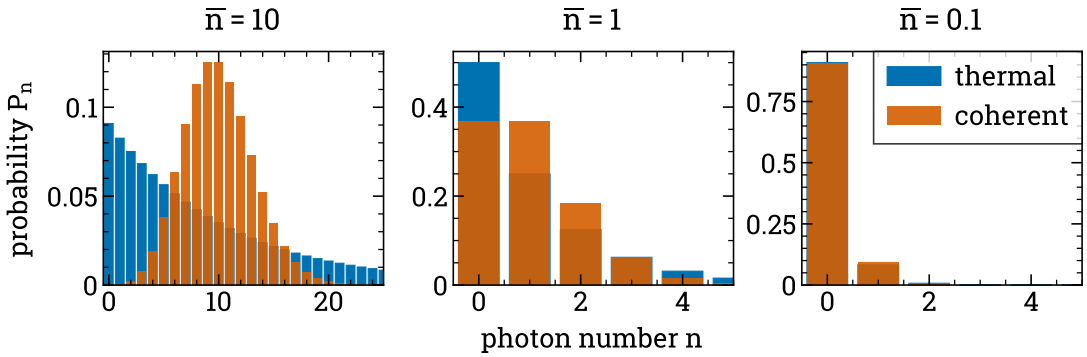

Figure 1.1: Exemplary photon number distributions P_n for single-mode thermal (Bose-Einstein-distributed) and coherent (Poisson-distributed) fields versus the average photon number $\bar{n}$. For $\bar{n} \ll 1$ both distributions become indistinguishable.

probability to remain in $|0\rangle$. As we have no means of predicting when exactly the photon will be emitted and the photon is absorbed in the detection process, a weak coherent states is no suitable carrier of quantum information.

Thermal Light The same argument holds for attenuated thermal light. Thermal light describes the incoherent radiation emitted from a hot body at some defined temperature. For a single mode of a thermal field containing an average photon number of $\bar{n}$ the Bose-Einstein distribution

$$P_n = \frac{\bar{n}^n}{(1+\bar{n})^{n+1}} \tag{1.4}$$

gives the probability to find n photons in the field. We compare this probability distribution to the Poissonian distribution in Figure 1.1. While they deviate significantly for $\bar{n} \gtrsim 1$, the thermal distribution converges to the Poissonian case in the regime of $\bar{n} \ll 1$. The fluctuations in the number of photons for a thermal field are given by $\Delta n = \sqrt{\bar{n} + \bar{n}^2}$, i. e., the fluctuations are larger than for a coherent state.

1.1.1 Two-Mode Squeezed Vacuum

We can overcome the problem of not knowing when a probabilistic source will emit a photon by implementing a heralding mechanism. When we generate correlated pairs of photons instead of single photons, one of the photons can be detected to obtain information on the presence of the second photon. We can describe such photon pairs by the *two-mode squeezed vacuum* state

$$|\xi\rangle_2 = \hat{S}_2(\xi)\,|0,0\rangle = \exp\left(\xi^* \hat{a}\hat{b} - \xi \hat{a}^\dagger \hat{b}^\dagger\right)|0,0\rangle \tag{1.5}$$

that we generate by applying the two-mode squeezing operator $\hat{S}_2(\xi)$ to the two-mode vacuum state $|0,0\rangle = |0\rangle_a \otimes |0\rangle_b$. Here, we labeled the two involved modes a and b. We can rewrite the state $|\xi\rangle_2$ in terms of the two-mode number states

$|n,m\rangle = |n\rangle_a \otimes |m\rangle_a$ as

$$|\xi\rangle_2 = \frac{1}{\cosh r} \sum_{n=0}^{\infty} (-1)^n \mathrm{e}^{\mathrm{i}n\theta} (\tanh r)^n \, |n,n\rangle \,, \tag{1.6}$$

where we rephrased the complex squeezing parameter as $\xi = r\mathrm{e}^{\mathrm{i}\theta}$. It is obvious, that only number states with the same number n of photons in both modes contribute to the squeezed state (1.6) and the single photon component is suppressed. The probability to find n photons in one of the individual modes i (without regarding the other mode respectively) is given by the thermal probability distribution we defined in Equation (1.4) with $\bar{n} = \langle \hat{n}_i \rangle^n = \sinh^2 r$. Therefore, we also expect a thermal distribution for the number of correlated pairs in state $|\xi\rangle_2$. For small $\bar{n} \ll 1$ the higher order terms with $n > 1$ in Equation (1.6) can be neglected (compare the $\bar{n} = 0.1$ case in Figure 1.1). In this situation, a detection in one of the modes reliably heralds the presence of a photon in the other mode.

Experimentally, we can realize a two-mode squeezed vacuum state $|\xi\rangle_2$ in a nonlinear frequency mixing process. In particular, we will focus here on spontaneous non-degenerate four wave mixing corresponding to the experiments we present in this work. We note, however, that the argument can easily be adapted to, e. g., (degenerate or non-degenerate) spontaneous parametric down-conversion.

The fully quantized Hamiltonian for a non-degenerate four-wave mixing process where two pump fields c and d generate two signal fields a and b reads

$$\hat{H} = \hbar\omega_a \hat{a}^\dagger \hat{a} + \hbar\omega_b \hat{b}^\dagger \hat{b} + \hbar\omega_c \hat{c}^\dagger \hat{c} + \hbar\omega_d \hat{d}^\dagger \hat{d} + \mathrm{i}\hbar\chi^{(3)} (\hat{a}\hat{b}\hat{c}^\dagger \hat{d}^\dagger - \hat{a}^\dagger \hat{b}^\dagger \hat{c}\hat{d}), \tag{1.7}$$

with the third-order nonlinear susceptibility $\chi^{(3)}$. The last term includes also the reversed mixing process and assures the hermiticity of the operator. When we pump the process with strong coherent fields with negligible depletion, we can apply the parametric approximation and replace $\hat{c}$ and $\hat{d}$ with their classical analogons $C\mathrm{e}^{-\mathrm{i}\omega_c t}$ and $D\mathrm{e}^{-\mathrm{i}\omega_d t}$ respectively. When we transform Equation (1.7) into the interaction picture and apply energy conservation written in terms of the frequencies $\omega_c + \omega_d = \omega_a + \omega_b$, the Hamiltonian for the case of non-degenerate four wave mixing becomes

$$\hat{H}_I = \mathrm{i}\hbar \left(\eta^* \hat{a}\hat{b} - \eta \hat{a}^\dagger \hat{b}^\dagger \right) \tag{1.8}$$

with the short notation $\eta = \chi^{(3)} CD$. The corresponding time-evolution operator is given by

$$\hat{U}_I(t) = \exp(-\mathrm{i}\hat{H}_I t/\hbar) = \exp\left(\eta^* t \hat{a}\hat{b} - \eta t \hat{a}^\dagger \hat{b}^\dagger \right). \tag{1.9}$$

When we identify $\xi = \eta t$, $\hat{U}_I(t)$ resembles a two-mode squeezing operator as defined in Equation (1.5).

We conclude here, that non-degenerate SFWM can be employed to generate correlated photon pairs. We will pick up the definition (1.8) again in Chapter 2 and extend it to a more detailed treatment of the SFWM process in our specific experimental implementation.

1.2 Figures of Merit

Different implementations of non-classical photon sources usually focus on coming close to the ideal case in a selected aspect of the source. To be able to quantify the performance of photon sources, we will now introduce the figures of merit that we will use throughout the remainder of this work. We note, that this list does not intent to be conclusive. An extensive list can be found, e. g., in [32]. Subsequently, we will give an overview over different experimental platforms for photon sources in Section 1.3.

Non-classical Correlations The fundamental difference between non-classical single photons and a weak coherent pulse attenuated to the single photon level lies in the photon statistics. We perform correlation measurements to quantify these statistics. In particular, we measure the second-order intensity correlation between two detection channels i and j that is generally defined as

$$g^{(2)}_{i,j} = \frac{\langle \hat{a}^\dagger_i \hat{a}^\dagger_j \hat{a}_j \hat{a}_i \rangle}{\langle \hat{n}_i \rangle \langle \hat{n}_j \rangle} = \frac{p_{i,j}}{p_i \cdot p_j} \tag{1.10}$$

where, in the second step, we connect the formal definition with the experimentally accessible detection probabilities per time bin. Here, p_i and p_j are the probabilities for a detection in the individual fields and p_{ij} the probability for a coincidence, i. .e., a detection in both channels within a suitable temporal coincidence gate. The denominator corresponds to the statistically expected *accidental* coincidences. We can interpret the correlation as a measure of how much the observed coincidences deviate from the expected accidental coincidences.

When we are interested in the photon statistics of a single field, we perform an *auto-correlation* measurement, i. e., we measure $g^{(2)}_{i,i}(\tau)$ via two detectors that monitor the outputs of a balanced beamsplitter in a Hanbury Brown and Twiss [35] (HBT) setup as sketched in Figure 1.2. Here, τ is the delay between the two detection events of a coincidence. For a coherent state with Poissonian statistics, we expect $g^{(2)}_{i,i} = 1$ for all τ as it corresponds to randomly distributed photons. The expected auto-correlation for thermal photon statistics is $1 \leq g^{(2)}_{i,i}(\tau) \leq 2$ [36]. We can interpret $g^{(2)}_{i,i}(\tau = 0) = 2$ as a higher than random probability to find multiple photons that converges to the random case of $g^{(2)}_{i,i} = 1$ for τ larger than the coherence time of the system.

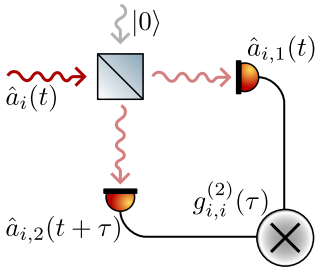

Figure 1.2: Hanbury Brown and Twiss setup.

Probably the most intuitive evidence of a single photon is the observation of *anti-bunching*, i. e., the absence of two photons at the same time which manifests in an auto-correlation $g^{(2)}_{i,i} \simeq 0 < 1$. As introduced in the previous section, we have to include a heralding mechanism to obtain such single photons. We thus have to measure the auto-correlation conditioned on the detection of a heralding photon

in channel j. From this we can define an anti-bunching parameter [37] as

$$\alpha = g^{(2)}_{i,i|j} = \frac{p_{i,i|j}}{p_{i|j}p_{i|j}} = \frac{p_{i,i,j}p_j}{p_{i,j}p_{i,j}}. \tag{1.11}$$

For $\alpha < 1$ we observe non-classical, anti-bunched (heralded) photons and $\alpha \leq 1/2$ confirms a non-zero projection onto the single-photon Fock state [38]. We emphasize here, that it is only through the heralding process, that we can observe anti-bunched photons in channel i. The same field exhibits thermal photon statistics when observed without taking the heralding channel into account.

For photon pair sources, an alternative metric is the *cross-correlation* between two detectors i and j observing the two generated fields of the generated pair. It is defined by Equation (1.10) in the case of $i \neq j$. For classical fields, the possible values for the cross correlation between the two modes are bound by the auto-correlations of the respective fields. We can formulate this as the Cauchy-Schwarz inequality [39]

$$\mathcal{R} = \frac{\left[g^{(2)}_{i,j}\right]^2}{g^{(2)}_{i,i}\, g^{(2)}_{j,j}} \leq 1. \tag{1.12}$$

We call correlations that violate this inequality, *non-classical correlations* and the corresponding state of the fields a *non-classical state*. For the two-mode squeezed vacuum state defined in Equation (1.6) we expect thermal autocorrelations of the individual fields, i. e., $g^{(2)}_{i,i} = g^{(2)}_{j,j} = 2$. Hence, we observe a non-classical violation of (1.12) for $g^{(2)}_{i,j} > 2$. For a perfect realization of state $|1,1\rangle$, there is no principle upper limit for $\mathcal{R}$. In a real experiment, though, small contributions of the higher order number states to the two-mode squeezed state (1.6), the finite measurement duration, and unavoidable experimental noise limit the observable violation of Inequality (1.12).

Photons that fulfill the criteria for non-classicality introduced in this paragraph are (at least in principle) suitable implementations of photonic qubits.

Heralding Efficiency Another method to quantify the experimentally introduced imperfections is the heralding efficiency η_{H} defined as the ratio of coincidences and heralding events when we interpret a pair source as a source of heralded single photons. While it would become unity for an ideal source, it is reduced in any real source by noise in the heralding channel that produce false heraldings and imperfect correlation between the heralding and signal photons.

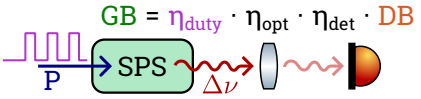

Figure 1.3: Necessary quantities for the calculation of different brightnesses as defined in the main text for a single photon source (SPS) with bandwidth $\Delta\nu$, pumped in a pulsed sequence with power P.

Brightness Not only the photon statistics but also the rate of the generated photons is relevant. We call the photon flux, i. e., the number of emitted photons per time, *brightness* B. This general definition is ambiguous when we consider a real life experiment. To be more precise, we first distinguish between the *detected brightness DB* and the *generated brightness GB* as sketched in Figure 1.3. The $GB = DB/\eta$ refers to the rate of photons emitted by experimental medium itself during (for a pulsed experiment) the active time period of the experiment and it is inferred from the *DB* by compensating it for all technical losses η such as optical transmission η_{opt}, detection efficiency η_{det}, and the duty cycle of the experiment η_{duty}. The *GB* is useful whenever we want to compare sources based on different fundamental generation mechanisms or implemented in different media without taking into account the technical details of the specific implementation. In contrast, the *DB* is relevant when one considers a specific implementation of a photon pair source as a black-box device in a larger scale application. In that case, technical details of the source are not of interest and relevant photon rate is that of the photons available for a subsequent application. To allow for a comparison between photon sources with significantly different spectral properties, we further define the *generated spectral brightness* as $GSB = GB/\Delta\nu$. Finally, we additionally calculate the *generated spectral brightness per pump power* $GSBP = GSB/P$ to include the conversion efficiency from a classical pump field with power P into non-classical output photons.

Spectral Properties Various applications can have significantly different requirements on the absolute wavelength as well as the bandwidth of single photons. For a single-peaked, e. g., Lorentzian, emission spectrum we can quantify the spectral width as the full width at half-maximum (FWHM) $\Delta\omega = 2\pi\Delta\nu$ of that peak. For a multi-peak or otherwise irregular spectrum, however, this definition might not be sufficient. The photon's spectrum directly determines its temporal shape. Depending on the planned application, e. g., temporal versus frequency multiplexing, one might have to trade off between temporal photon duration and frequency bandwidth.

For long range transmission within the existing telecommunication fiber network, photons at a wavelength of about 1300 nm or 1550 nm, known as the telecommunication O-band and C-band [40] are required. For these wavelengths, the attenuation in fused silica fibers is minimized. As the transmission windows span several 10 nm, the required precision in the absolute wavelength and the acceptable photon bandwidth are both in the nm regime. The situation for free-space satellite links is similar, though a larger number of atmospheric transmission windows exist including also visible wavelengths [29]. For closer range transmission, e. g., within a single laboratory we have no practical restrictions on the photon's wavelength or bandwidth.

To interface the photons with other nodes in a quantum network, they typically

have to match the transition frequencies and line widths exhibited by the specific media. For cold alkali atoms, these are given by the medium's natural line width in the regime of a few MHz. In hot vapor the transition lines are Doppler broadened to multiple 100 MHz. As another example, quantum memories implemented in solid-state media exhibit memory bandwidths in the range of a few 10 kHz to a few GHz [41–43] depending on the specific medium, the storage protocol, and its experimental implementation.

To match the absolute wavelengths, we can either use photon sources and nodes implemented in the same medium, or use additional quantum frequency conversion stages [44]. These conversions can also be used to shift a photons wavelength to the telecommunication band and back for efficient long-range transport [45].

Integrability Towards large scale quantum networks and real-life applications we have to consider the integrability of a photon source. Photon sources that emit into free space require an additional (lossy) step to deliver fiber based photons. Furthermore, free-space setups are inherently susceptible to misalignment and typically require significant maintenance to retain their performance. They also have only limited potential for miniaturization.

There is no established quantity to access the level of integration for a given photonic device but we can group the different approaches in classes depending on their depth of waveguide integration. In free-space sources the generation process itself is not performed in a waveguide environment. In intra-fiber or, more generally, waveguide-based sources the fundamental process that generates the single photons takes place within the waveguide environment. Still, such a source may include free-space components, e. g., in the preparation of the medium, to generate or apply the driving fields for the generation process, or in a subsequent separation or filtering stage to achieve the required photon properties. Fully integrated sources include all of the necessary stages in the waveguide environment. We note, that these classes are not sharply defined so not every source can be clearly assigned to one of them. Nevertheless they will be helpful when we discuss the variety of approaches to generate single photons in the following section.

1.3 Platforms and Protocols

In this section, we give a brief overview over the various implementations of single photon sources in different experimental media and classify them according to the previously introduced quantities. We limit ourselves here to a summary in order to contextualize the results of our work and refer the reader to the various in-depth reviews [10, 32, 46] for more details and further references.

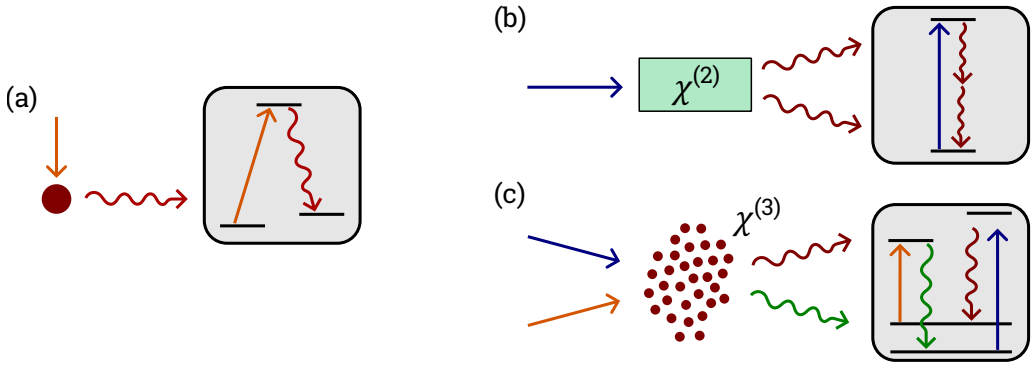

Figure 1.4: Different types of single photon sources: Single emitters (a) and Photon pair sources implemented in nonlinear media. As examples, we show degenerate SPDC in a bulk medium (b) and non-degenerate SFWM in an ensemble of emitters (c).

We sketch two fundamentally different concepts for single photon sources in Figure 1.4. The first type of sources are isolated individual emitters which can be implemented in various media including semiconductor quantum dots, single atoms or ions, and color centers in diamonds [10]. These sources are typically operated by exciting the emitter by some external pumping mechanism and collect the photon emitted in the subsequent relaxation. For an efficient collection of the photons most experimental implementations include optical cavities. By design, these sources sources are probably the most deterministic single photons sources to date. However, they can not directly create non-classical photon pairs and the distinguishability of photons generated at different sites might limit some applications such as quantum repeaters [47]. Semiconductor based sources offer large potential for fully integrated sources [48].

The second type of sources are photon pair sources based on nonlinear processes that can be implemented either in bulk material such as nonlinear crystals or in ensembles of emitters. In bulk material, spontaneous parametric down-conversion (SPDC) is widely employed for the generation of non-classical photon pairs. A pump field is converted into two photons of lower frequency which are typically collected under (matched) angles. While the bandwidth in standard SPDC experiments is typically in the nm regime [12], these sources can reach the highest photon rates with a *DB* in the regime of $10^6\,\text{pairs}\,\text{s}^{-1}\,\text{mW}^{-1}$ and can currently exceed the detection limit for state-of-the-art single photon detectors [49]. Cavity-enhanced SPDC can generate narrowband photons in the MHz regime [14], though at the cost of a reduced brightness. In [50], a Rubidium compatible source with a *GSBP* of $3.7 \times 10^5\,\text{pairs}\,\text{s}^{-1}\,\text{MHz}^{-1}\,\text{mW}^{-1}$ at a bandwidth of 4.5 MHz is reported. We refer the reader to [51] for an overview of current results in

narrowband cavity-SPDC.

Atomic ensembles can enhance the generation process due to phase-matched collective effects [13]. Photon pairs are generated in a SFWM-type scheme, where two pump fields generate two signal fields with frequencies defined by energy conservation. Due to spatial phase matching, the photons can be effectively collected without a cavity. SFWM is typically implemented in alkali atoms, either in hot atomic vapor or in cold atoms. Hot vapor is technically less challenging to implement but in general the photon bandwidth suffers from Doppler broadened transitions and short coherence times. However, using a phase-mismatch free scheme, sub-MHz line widths were reported in [52]. Cold atoms have the advantage of longer coherence times in the µs regime that facilitate the generation of temporally long and, therefore, spectrally narrowband photons. In [53], the authors report on a bandwidth of 50 kHz at a *GSBP* of 1.2×10^6 pairs s^{-1} MHz^{-1} mW^{-1}, the current record for narrowband photon generation. The drawback of cold atomic systems is the required preparation of the sample that adds technical complexity and can severely limit the duty cycle of the experiment. Depending on the experimental geometry, filtering out the strong pumping beams required for the SFWM process can also be challenging.

The DLCZ protocol [54] is a time-delayed version of SFWM in which the probabilistic generation of a single collective excitation of the atomic medium is heralded by the detection of a *write* photon. Subsequently, this excitation can be *read* out deterministically and (in principal) with unit efficiency within the coherence time of the system. DLCZ sources can generate narrowband photons with sub-MHz line widths when implemented in a cold ensemble but the *GB* is limited by the probabilistic and intrinsically pulsed write process [55]. A modified version of the DLCZ protocol has also been implemented in a solid state ensemble, i. e., a rare-earth-ion doped crystal [56]. DLCZ has also been implemented in a partially integrated experiment where an ensemble of trapped atoms is coupled to a nanofiber [18]. While the photons are emitted into the waveguide mode, the write and read fields are still applied from free space.

High *GSBP* in excess of 1×10^5 pairs s^{-1} MHz^{-1} mW^{-1} combined with narrowband emission was achieved using a variety of different experimental systems. These are waveguides combined with cavities [19, 57], a bulk crystal inside a cavity [51], and room-temperature as well as cold atomic ensembles [53, 58]. The bandwidths of these photon-pair sources ranged from 50 kHz [53] to around 100 MHz [19] and the *GSBP* ranged from 3×10^4 pairs s^{-1} MHz^{-1} mW^{-1} [57] to 2×10^8 pairs s^{-1} MHz^{-1} mW^{-1} [19].

Finally, sources based on driving SPDC or SFWM in a waveguide within a nonlinear material have a very high degree of integration. However, these experiments are typically designed at telecommunication wavelength and exhibit bandwidths in the regime of nm which makes them incompatible with atomic transitions [11].

Chapter 2

Photon-Pair Generation via Spontaneous Four-Wave Mixing in an Atomic Ensemble

In our experiments, we generate correlated photon pairs in an atomic ensemble via SFWM [59, 60]. In this chapter, we extend the very general treatment of the two-mode squeezed vacuum state introduced in Section 1.1.1 in the context of our experimental implementation. We introduce the formalism to describe the nonlinear SFWM process based on experimental parameters and discuss characteristic regimes in the resulting biphoton spectra. Our mathematical treatment follows [61].

2.1 Basics and Formalism

We consider an ensemble of identical atoms that exhibit the level scheme shown in Figure 2.1(a). The double-Λ coupling scheme consists of two ground states and two excited states with the angular transition frequencies ω_{ij} between levels $|i\rangle$ and $|j\rangle$. We assume that the medium is initially fully prepared in state $|1\rangle$.

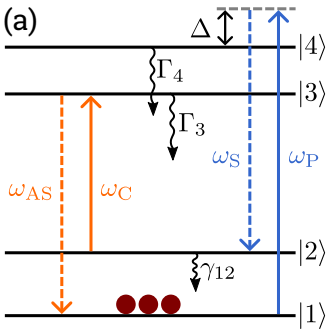

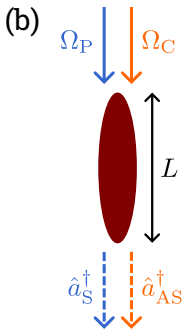

Figure 2.1: (a) Double-Λ coupling scheme for SFWM in a four level medium. The pump (blue) and control (orange) fields (solid arrows) generate correlated Stokes (blue) and anti-Stokes (orange) photons (dashed arrows). The excited states decay with rates Γ_i and the ground state dephasing rate is γ_{12}. (b) Co-propagating forward configuration in a cylindrical medium.

We apply a pump field with frequency $\omega_P = \omega_{14} + \Delta$ where the detuning Δ is chosen to minimize optical pumping. Simultaneously, we apply the control field (frequency ω_C) resonantly to the transition $|2\rangle \leftrightarrow |3\rangle$. The two fields drive a coherent SFWM process and generate temporally correlated Stokes (S) and anti-Stokes (AS) photons at frequencies ω_S and ω_{AS} respectively [60]. The control field also creates a spectral transparency window via electromagnetically induced transparency (EIT) [62] that allows the AS photon to propagate through the medium, though at a reduced group velocity v_g due to the slow light effect.

As we will implement the SFWM process experimentally in an atomic medium confined within a long hollow-core fiber, we further restrict ourselves now to the configuration sketched in Figure 2.1(b). We assume a cylinder shaped ensemble with length L and atomic density $\mathcal{N}$, elongated along the lights propagation axis z. Furthermore, we only consider a forward generating scheme in which all

four fields propagate colinearly through the medium. We note, however, that generally also a backward configuration is possible (compare, e. g., [60, 63]), but was not implemented in our experiment for technical reasons (as explained further in Section 5). We consider only a single transversal mode (corresponding to the guided fiber mode in the experiment) and neglect polarization effects for simplicity. The polarization dependence of the SFWM process in our medium will be treated separately in Appendix A.

We describe the strong driving fields, i. e., pump and control, classically by their electric fields $E_i(z,t)$ that we separate into their positive and negative frequency components $E_i^{(+/-)}$ as (for $i = \mathrm{P}, \mathrm{C}$)

$$E_i(z,t) = \frac{1}{2}\left[\mathcal{E}_i \mathrm{e}^{\mathrm{i}(k_i z - \omega_i t)} + \mathrm{c.c.}\right] = \frac{1}{2}\left[E_i^{(+)} + \mathrm{c.c.}\right] \tag{2.1}$$

with the field envelopes $\mathcal{E}_i$. Note, that the envelopes are in general slowly (compared to ω_i and k_i) varying but we omit this dependence here for clarity. The vacuum wave numbers (in our one dimensional simplification) are given by $k_i = \omega_i/c_0$ where c_0 is the speed of light in vacuum. To quantify the coupling of the fields to the medium, we define the Rabi frequencies $\Omega_\mathrm{C} = \mu_{23}E_\mathrm{C}/\hbar$ and $\Omega_\mathrm{P} = \mu_{14}E_\mathrm{P}/\hbar$ with the transition dipole matrix elements μ_{ij}.

We model the generated S and AS fields including their continuous spectral components[1] as (for $j = \mathrm{S}, \mathrm{AS}$)

$$\hat{E}_j(z,t) = \frac{1}{2}\left[\frac{1}{\sqrt{2\pi}}\sqrt{\frac{2\hbar\omega_{j,0}}{c_0\epsilon_0 A}}\int \mathrm{d}\omega_j \hat{a}_j(\omega_j)\mathrm{e}^{\mathrm{i}(k_j(\omega_j)z-\omega_j t)} + \mathrm{h.c.}\right] = \frac{1}{2}\left[\hat{E}_j^{(+)} + \mathrm{h.c.}\right], \tag{2.2}$$

i. e., as quantized radiation fields in a single transverse mode with their respective bosonic annihilation operators $\hat{a}_j(\omega_j)$ that are subject to the commutator $\left[\hat{a}_j(\omega'), \hat{a}_j^\dagger(\omega'')\right] = \delta(\omega' - \omega'')$, the mode diameter A and the vacuum permittivity ϵ_0. We also introduced the notation $\omega_{j,0}$ for the fixed S and AS central frequencies.

The Hamiltonian describing the four-wave mixing process in the interaction picture is given by

$$\hat{H} = \frac{\epsilon_0 A}{4}\int_{-L/2}^{L/2} \mathrm{d}z\, \chi^{(3)} E_\mathrm{C}^{(+)} E_\mathrm{P}^{(+)} \hat{E}_\mathrm{AS}^{(-)} \hat{E}_\mathrm{S}^{(-)} + \mathrm{h.c.}, \tag{2.3}$$

where the creation of the S and AS photons is connected to the annihilation of pump and control photons via the third-order nonlinear susceptibility $\chi^{(3)}$ that depends on experimental quantities as will be detailed in Equation (2.14). As we plan to work in the low excitation regime to generate single photon pairs, we neglect here higher-order mixing terms. With the definitions (2.1) and (2.2) and by introducing the nonlinear parametric coupling coefficient $\kappa = -\mathrm{i}\frac{\sqrt{\omega_{AS,0}\omega_{S,0}}}{2c_0}\mathcal{E}_\mathrm{P}\mathcal{E}_\mathrm{C}\chi^{(3)}$ and the phase mismatch $\Delta k = (k_\mathrm{AS} + k_\mathrm{S} - k_\mathrm{C} - k_\mathrm{P})$, we may rewrite the Hamiltonian

[1] The continuous frequency spectrum can be obtained from the usual sum over discrete modes via the replacement $\sum_k \to 2\pi c_0/L \int \mathrm{d}\omega$ and $\hat{a}_k \to \sqrt{2\pi c_0/L}\hat{a}(\omega)$. See [36] for details.

as

$$\begin{aligned}\hat{H} &= \frac{\mathrm{i}\hbar}{2\pi}\int \mathrm{d}\omega_{\mathrm{AS}}\mathrm{d}\omega_{\mathrm{S}}\kappa\hat{a}^{\dagger}_{\mathrm{AS}}(\omega_{\mathrm{AS}})\hat{a}^{\dagger}_{\mathrm{S}}(\omega_{\mathrm{S}})\mathrm{e}^{-\mathrm{i}(\omega_{\mathrm{P}}+\omega_{\mathrm{C}}-\omega_{\mathrm{AS}}-\omega_{\mathrm{S}})t}\int_{-L/2}^{L/2}\mathrm{d}z\mathrm{e}^{-\mathrm{i}\Delta kz}+\mathrm{h.c.}\\ &= \frac{\mathrm{i}\hbar L}{2\pi}\int \mathrm{d}\omega_{\mathrm{AS}}\mathrm{d}\omega_{\mathrm{S}}\kappa\hat{a}^{\dagger}_{\mathrm{AS}}(\omega_{\mathrm{AS}})\hat{a}^{\dagger}_{\mathrm{S}}(\omega_{\mathrm{S}})\mathrm{e}^{-\mathrm{i}(\omega_{\mathrm{P}}+\omega_{\mathrm{C}}-\omega_{\mathrm{AS}}-\omega_{\mathrm{S}})t}\mathrm{sinc}\left(\frac{\Delta kL}{2}\right)+\mathrm{h.c.}, \quad (2.4)\end{aligned}$$

where, in the second step, we carried out the z integration to obtain the sinc function.

Using perturbation theory [61], one can write the state at the end of the medium as the sum $|0\rangle + |\Psi\rangle$ of the biphoton state

$$|\Psi\rangle = -\frac{\mathrm{i}}{\hbar}\int_{-\infty}^{\infty}\mathrm{d}t\hat{H}\,|0\rangle \quad (2.5)$$

and the vacuum state $|0\rangle$. When we insert Equation (2.4) and carry out the temporal integration we obtain

$$|\Psi\rangle = L\int \mathrm{d}\omega_{\mathrm{AS}}\mathrm{d}\omega_{\mathrm{S}}\kappa\hat{a}^{\dagger}_{\mathrm{AS}}(\omega_{\mathrm{AS}})\hat{a}^{\dagger}_{\mathrm{S}}(\omega_{\mathrm{S}})\delta(\omega_{\mathrm{P}}+\omega_{\mathrm{C}}-\omega_{\mathrm{AS}}-\omega_{\mathrm{S}})\mathrm{sinc}\left(\frac{\Delta kL}{2}\right)|0\rangle\,. \quad (2.6)$$

The δ function describes the entanglement in frequency due to the conservation of energy. We can thus rewrite the state using only the AS frequency component ω as our variable. Hence, the final form of our biphoton state becomes

$$|\Psi\rangle = L\int \mathrm{d}\omega\kappa\mathrm{sinc}\left(\frac{\Delta kL}{2}\right)\hat{a}^{\dagger}_{\mathrm{AS}}(\omega)\hat{a}^{\dagger}_{\mathrm{S}}(\omega_{\mathrm{P}}+\omega_{\mathrm{C}}-\omega)\,|0\rangle\,. \quad (2.7)$$

The experimentally accessible quantities are the temporally resolved photons at the exit surface of the medium at $z = L/2$. To predict the observable temporal correlations, we express the annihilation operators on the surface in the time domain as (for $j = \mathrm{S}, \mathrm{AS}$)

$$\hat{a}_j(t) = \frac{1}{\sqrt{2\pi}}\int \mathrm{d}\omega'\hat{a}_j(\omega')\mathrm{e}^{\mathrm{i}\left(k_j(\omega')L/2-\omega' t\right)}. \quad (2.8)$$

The joint probability to detect a S photon at time t_{S} and an AS photon at time t_{AS} at their respective detectors is defined as [64]

$$\begin{aligned}G^{(2)}(t_{\mathrm{AS}}, t_{\mathrm{S}}) &= \langle\Psi|\,\hat{a}^{\dagger}_{\mathrm{S}}(t_{\mathrm{S}})\hat{a}^{\dagger}_{\mathrm{AS}}(t_{\mathrm{AS}})\hat{a}_{\mathrm{S}}(t_{\mathrm{S}})\hat{a}_{\mathrm{AS}}(t_{\mathrm{AS}})\,|\Psi\rangle\\ &= |\Psi(t_{\mathrm{AS}}, t_{\mathrm{S}})|^2 = |\psi(\tau)\mathrm{e}^{-\mathrm{i}(\omega_{\mathrm{C}}+\omega_{\mathrm{P}})t_{\mathrm{S}}}|^2 \quad (2.9)\\ &= |\psi(\tau)|^2, \quad (2.10)\end{aligned}$$

where we separated the biphoton wave function Ψ into the *relative biphoton wave function* $\psi(\tau)$ that only depends on the time difference $\tau = t_{\mathrm{AS}} - t_{\mathrm{S}}$ between the S and AS detections, and an arbitrary phase factor depending on the absolute detection time t_{S}. We call $|\psi(\tau)|^2$ the (temporal) *biphoton wave form* and $|\kappa(\delta)\Phi(\delta)|^2$

the corresponding *biphoton spectrum* in the frequency domain.

By introducing the single photon detuning of the AS frequency components ω as $\delta = \omega - \omega_{\mathrm{AS}}$, we can write the relative biphoton wave function in the compact form

$$\psi(\tau) = \frac{L}{2\pi} \int \kappa(\delta)\Phi(\delta)\mathrm{e}^{-\mathrm{i}\delta\tau}\mathrm{d}\delta \tag{2.11}$$

with the *nonlinear parametric coupling coefficient*

$$\kappa(\delta) = -\mathrm{i}\frac{\sqrt{\omega_{\mathrm{AS},0}\omega_{\mathrm{S},0}}}{2c}\chi^{(3)}(\delta)\mathcal{E}_{\mathrm{P}}\mathcal{E}_{\mathrm{C}} \tag{2.12}$$

and the *longitudinal detuning function*

$$\Phi(\delta) = \mathrm{sinc}\left(\frac{\Delta k L}{2}\right)\mathrm{e}^{\mathrm{i}(k_{\mathrm{AS}}+k_{\mathrm{S}})L/2}, \tag{2.13}$$

where the width of the sinc function determines the phase matched bandwidth of SFWM process. These two quantities each describe different aspects of the created photon pairs. The nonlinear parametric coupling coefficient $\kappa(\delta)$ describes the strength of the four wave mixing process and thus determines the generation rate of the photon pairs. It is determined by the third-order nonlinear susceptibility for the AS field given by

$$\chi^{(3)}(\delta) = \frac{\mathcal{N}\mu_{13}\mu_{32}\mu_{24}\mu_{41}/(\epsilon_0\hbar^3)}{(\Delta + \mathrm{i}\frac{\Gamma_4}{2})\left[|\Omega_{\mathrm{C}}|^2 - 4(\delta + \mathrm{i}\frac{\Gamma_3}{2})(\delta + \mathrm{i}\gamma_{12})\right]}. \tag{2.14}$$

The longitudinal detuning function controls the biphotons spectral and temporal shape determined by the spatial phase matching due to the experimental geometry and the influence of the medium on the created individual S and AS fields. It is determined by the respective linear susceptibilities

$$\chi_{\mathrm{S}}(\delta) = \frac{\mathcal{N}|\mu_{24}|^2(\delta - \mathrm{i}\frac{\Gamma_3}{2})/(\epsilon_0\hbar)}{|\Omega_{\mathrm{C}}|^2 - 4(\delta - \mathrm{i}\frac{\Gamma_3}{2})(\delta - \mathrm{i}\gamma_{12})} \times \frac{|\Omega_{\mathrm{P}}|^2}{\Delta^2 + \left(\frac{\Gamma_4}{2}\right)^2}, \tag{2.15}$$

$$\chi_{\mathrm{AS}}(\delta) = \frac{4\mathcal{N}|\mu_{13}|^2(\delta + \mathrm{i}\gamma_{12})/(\epsilon_0\hbar)}{|\Omega_{\mathrm{C}}|^2 - 4(\delta + \mathrm{i}\frac{\Gamma_3}{2})(\delta + \mathrm{i}\gamma_{12})}, \tag{2.16}$$

that are connected to the longitudinal detuning function via the complex wave numbers $k_j(\delta) = \frac{\omega_{j,0}}{c_0}\sqrt{1+\chi_j(\delta)}$ of the created fields. Using this definitions, we can identify the refractive index $n_j(\delta) = \mathrm{Re}\left[\sqrt{1+\chi_j(\delta)}\right] \approx 1 + \frac{1}{2}\mathrm{Re}\left[\chi_j(\delta)\right]$ and absorption coefficient $\alpha_j(\delta) = 2\mathrm{Im}\left[k_j(\delta)\right] \approx \frac{\omega_{j,0}}{c_0}\mathrm{Im}\left[\chi_j(\delta)\right]$. The absorption coefficient describes the intensity attenuation of a light field propagating through the medium by

$$I/I_0 = \mathrm{e}^{-\alpha_i(\delta)L} \tag{2.17}$$

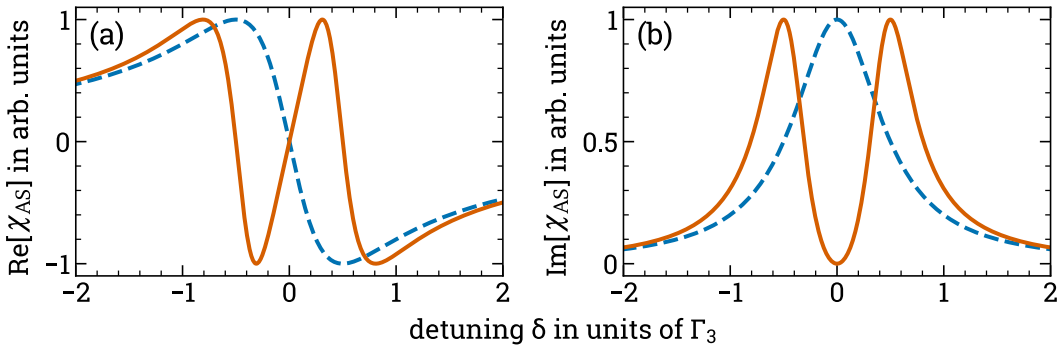

Figure 2.2: Real and imaginary part of the linear susceptibility defined in Equation (2.16) versus the relative detuning of a probe field from the AS transition, . The reference (dashed blue line) with $\Omega_C = 0$ shows anomalous dispersion and a Lorentzian absorption line. In the presence of a control field (solid orange line), the medium exhibits normal dispersion and the absorption line splits up by $\Omega_C = \Gamma_3$ due to EIT. We assume $\gamma_{12} = 0$ here.

and we can define the resonant *optical depth*

$$OD = \alpha_{AS}(\delta = 0)L = \frac{2\mathcal{N}\mu_{13}^2\omega_{AS,0}L}{\Gamma_3 c_0 \epsilon_0 \hbar} \tag{2.18}$$

on the AS transition as the characterizing quantity for our medium throughout this work.

In Figure 2.2 we plot the real and imaginary part of the linear susceptibility on the AS transition. In the presence of a control field the Lorentzian absorption line splits up into two lines and exhibits a transmission window for the AS photon on resonance $\delta = 0$. This effect is called EIT and it allows the propagation of the AS photon through the medium even though it couples resonantly to the populated ground state $|1\rangle$. Simultaneously, the normal dispersion $\mathrm{d}n/\mathrm{d}\omega > 1$ for $\Omega_C \neq 0$ leads to a reduced group velocity given by [62]

$$v_g = \frac{c_0}{n_{AS} + \omega_{AS}(\mathrm{d}n_{AS}/\mathrm{d}\omega)}. \tag{2.19}$$

Due to this *slow light* effect, the AS field acquires a temporal group delay of

$$\tau_g = \frac{L}{v_g} = \frac{OD \cdot \Gamma_3}{|\Omega_C|^2} \tag{2.20}$$

when propagating through the medium compared to vacuum.

2.2 Regimes of Photon-Pair Generation

We now analyze the spectral and temporal properties of the photon pairs generated via SFWM by applying the formalism developed in the previous section. In Figure 2.3 we show the calculated biphoton spectrum and temporal wave form using Equations (2.11) to (2.14) for varying *OD* over three orders of magnitude and two different control Rabi frequencies Ω_C. For simplicity, we here keep the pump Rabi frequency Ω_P and Δ fixed. As long as they satisfy $\Omega_P \ll \Delta$, these parameters only influence the biphotons generation rate but not their spectral properties.

For low *OD* the phase-matched bandwidth in Equation (2.13) is large compared to the control Rabi frequency and natural line width, i. e., the longitudinal detuning becomes approximately constant $\Phi(\delta) \simeq 1$ and the biphoton properties are controlled by the nonlinear susceptibility $\chi^{(3)}(\delta)$ as defined in Equation (2.14). It is instructive to introduce the effective Rabi frequency $\Omega_e = \sqrt{|\Omega_C|^2 - (\Gamma_3/2 - \gamma_{12})^2}$ and dephasing rate $\Gamma_e = (\gamma_{12} + \Gamma_3/2)$ and rewrite the nonlinear susceptibility as

$$\chi^{(3)}(\delta) = \frac{-\mathcal{N}\mu_{13}\mu_{32}\mu_{24}\mu_{41}/(\epsilon_0\hbar^3)}{4(\Delta + i\Gamma_4/2)(\delta - \Omega_e/2 + i\Gamma_e/2)(\delta + \Omega_e/2 + i\Gamma_e/2)}. \tag{2.21}$$

The biphoton spectrum clearly exhibits two resonances (compare Figure 2.3(a)) which are separated by Ω_e and exhibit spectral widths of Γ_e. The interference between these two possible generation channels leads to damped Rabi oscillations with the effective Rabi frequency Ω_e and effective dephasing rate Γ_e (compare Figure 2.3(d)). As a consequence, this regime of photon-pair generation is termed *damped Rabi regime* [60, 61]. Because the effective dephasing rate has a lower limit $\Gamma_3/2$, even narrower, sub-natural biphoton line widths cannot be obtained in the damped Rabi regime.

In contrast, for large *OD* the biphoton spectrum is dominated by the phase matching condition described by $\Phi(\delta)$ and the double resonance structure is washed out (compare Figure 2.3(b) and (c)). The observed biphoton waveform depends now on the ratio between the phase matched bandwidth and the EIT bandwidth. Whenever the EIT bandwidth is the larger, we obtain an almost rectangular wave form as shown in Figure 2.3(f). Here, the correlation time is determined by the group delay time defined in Equation (2.20) and the biphoton spectrum can become significantly more narrow than the natural line width. This generation regime is called *group delay regime* [65, 66]. The effect of the EIT bandwidth and residual absorption lies in the exponential decay of the biphoton waveform in the time domain. When the EIT bandwidth becomes comparable to or more narrow than the phase matched bandwidth the biphoton wave form transitions from a rectangular into a falling exponential shape (orange curve in Figure 2.3(f) and blue curve in (e)).

The experiments presented in this work are predominantly performed in an intermediate regime in between the two cases we just discussed. Thus, it is crucial that we include both regimes in our analysis. The central panels in Figure 2.3 show spectra and temporal wave forms in this intermediate regime that exhibit features from both fundamental regimes. The resulting biphoton wave form resembles

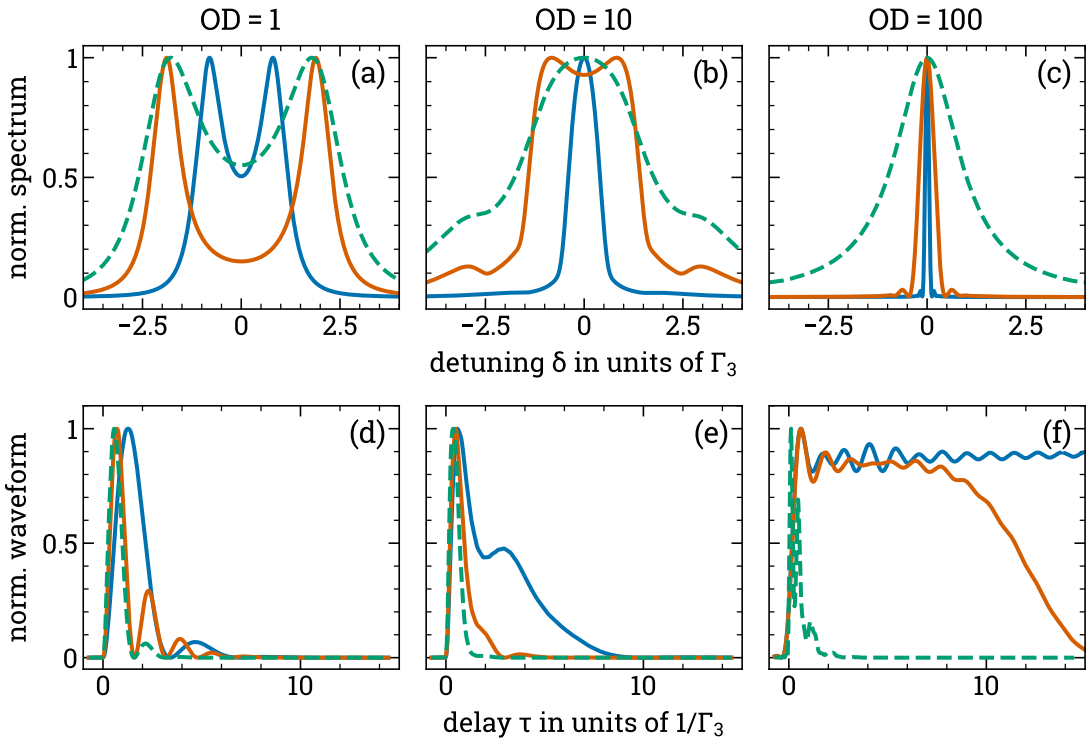

Figure 2.3: Biphoton spectrum $|\kappa(\delta)\Phi(\delta)|^2$ and temporal waveform $|\psi(\tau)|^2$ for different ODs (left to right) and control Rabi frequencies $\Omega_C = 2\Gamma_3$ (solid blue line) and $\Omega_C = 4\Gamma_3$ (solid orange line). Panels (a) and (d) show the damped Rabi oscillation regime and panels (c) and (f) the group delay regime. The fixed parameters are $\Omega_P = \Gamma_4$, $\Delta = 20\Gamma_4$, and $\gamma_{12} = 0$. The dashed green lines are calculated with $\gamma_{12} = \Gamma_3$ and $\Omega_C = 4\Gamma_3$.

an exponential decay with the residual Rabi oscillations still clearly visible. For a further in-depth discussion of the two biphoton generation regimes we refer the reader to [61].

For all calculations shown in Figure 2.3 with solid lines we neglected the ground state dephasing rate γ_{12} as it is only of the order of 1 % of Γ_3 for our experimental realization and has no significant influence on the biphoton's spectral properties. We note, however, that for $\gamma_{12} \simeq \Gamma_3$, the residual absorption within the EIT window as well as the effective dephasing rate of the photon pairs Γ_e are significantly increased. The dashed green lines in Figure 2.3 illustrate that in this case the biphoton coherence time is limited by the ground state coherence time in all the generation regimes we just introduced. The ground state decoherence rate γ_{12} sets a fundamental lower limit for the achievable biphoton line width.

Chapter 3

Cold Rubidium in a Hollow-Core Fiber

The nonlinear optical medium in our experiment is an ensemble of up to 2.5×10^5 cold Rubidium atoms located inside a *hollow-core photonic bandgap fiber* (HCPBGF). In this chapter, we start by summarizing the most relevant properties of our hollow-core fiber and the Rubidium atoms. Next, we introduce the experimental setup to trap, cool, and subsequently transfer the atoms into the fiber core. We conclude with a thorough characterization of our medium with regard to the planned SFWM experiments.

3.1 Hollow-Core Photonic Bandgap Fibers

Hollow-core fibers are optical silica fibers that exhibit a hollow core and an additional air-gaped structure surrounding the core (compare Figure 3.1(a)). In contrast to a standard step-index fiber, guided light is predominantly localized within the hollow core. This offers a number of advantages compared to step-index fibers [67]. Due to the guiding in air or vacuum, hollow-core fibers exhibit extremely low optical nonlinearities, higher power handling capacity and lower latencies [68]. Conversely, they can also be used to enhance nonlinear coupling. Gas filled hollow-core fibers can be employed for, e. g., nonlinear frequency converters, pulse compressors, or Raman spectroscopy [69]. Most important for our work though, hollow-core fibers can facilitate strong light-matter coupling due to the near optimal spatial overlap between the guided optical field and the density distribution of an ensemble of cold atoms confined within the hollow core of the fiber [70]. Additionally, nonlinear effects benefit from the intrinsic spatial mode matching when all involved fields are guided within the same single-mode fiber. Smaller core diameters lead to a larger enhancement of nonlinear processes due to the tight confinement of the guided light. Moreover, it was demonstrated [71] that HCPBGF can be spliced to standard polarization-maintaining single-mode fibers and, thus, can be integrated directly into larger fiber based networks.

Light propagation in hollow-core fibers cannot be explained by means of total internal reflection as this would require a cladding with a lower index of refraction than the air or vacuum within the hollow core. In the case of HCPBGFs, the guiding mechanism is instead based on creating photonic bandgaps transversally around the core, i. e., regions in which light propagation is suppressed and hence only propagation within the hollow core remains possible [73, 74]. Such bandgaps arise in so called *photonic crystals*, i. e., materials with a periodic modulation of their index of refraction n. For simplicity, we now consider a one dimensional photonic crystal and analyze the band structure of light propagating through the crystal. Figure 3.1(b) shows the band structure for a homogeneous medium without any modulation of n. Fields of all frequencies can propagate through the

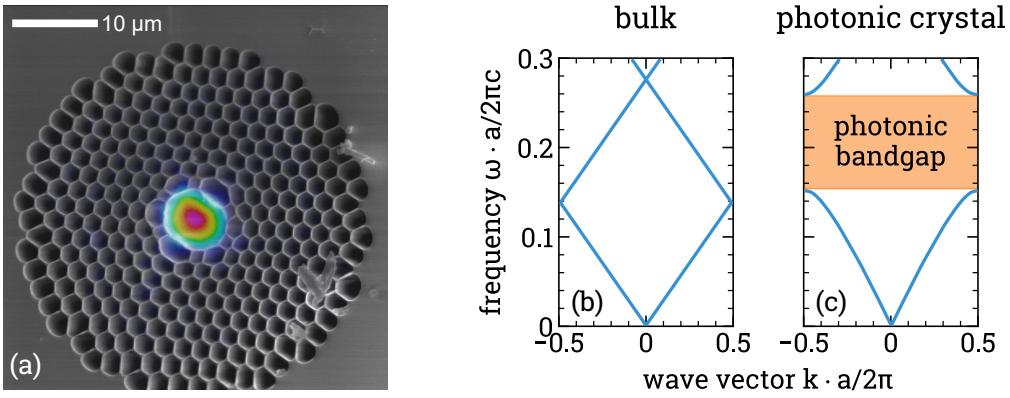

Figure 3.1: (a) Scanning electron image of the HCPBGF's transversal structure overlayed with a false-color plot of the measured intensity distribution of the guided mode. Adapted from [72]. (b)+(c) Photonic band stucture for bulk material (b) and a one-dimensional photonic crystal (c) with alternating index of refraction with periodicity 0.5 a. The photonic crystal exhibits a bandgap of non-transmitted frequencies between the air band and dielectric band. Adapted from [73] (modified).

crystal. In Figure 3.1(c) we plot the band structure for a periodic modulation of n. A bandgap, i. e., a range of frequencies which cannot propagate through the medium, appears. The width of the bandgap increases with a larger variation in n. Naturally, the use of air as the low n medium yields the largest possible bandgap. For frequencies above (below) the bandgap, the energy is predominantly concentrated in low-n (high-n) region. In analogy to solid-state physics, these two bands are referred to as air (dielectric) band. Incident light with a frequency within the bandgap is exponentially attenuated within the photonic crystal. A spatial defect in the photonic crystal lattice however, i. e., a single larger spaced air region, can still transmit frequencies within the bandgap. In the case of a photonic crystal fiber, a periodic structure extends in both transversal directions around a larger air core. The fiber is homogeneous in the third dimension allowing the light to propagate confined within the hollow core perpendicular to the transversal periodic structure. An alternative and perhaps more intuitive picture is that the guided light in the core is reflected, not due to total internal reflection as in solid core fibers, but due to Bragg reflection at the periodic structure surrounding the core [73].

A well established alternative to HCPBGFs are so called *Kagome fibers* [75]. They offer a larger single-mode bandwidth, low birefringence and simplify loading atoms into the fiber [76, 77] due to their low numerical aperture (NA) and larger core diameter of multiple 10 µm. However, for the same reason the enhancement of the light-matter interaction is reduced compared to HCPBGFs and it is a remaining challenge to obtain low-loss, single-mode and polarization-maintaining operation at the same time [78]. A more recent development are hollow core *anti-resonant fibers* [79, 80], where the cladding structure is specifically engineered to improve selected properties of the fiber, such as transmission loss or guiding bandwidth. The core size, though, is similar to that of Kagome fibers [81].

The particular fiber used in our experiments is a 14 cm long HCPBGF[1] with a core diameter of about 7 µm and a NA of ∼ 0.15. Due to the small core diameter, we can achieve Rabi frequencies of the order of the natural line width Γ in Rubidium atoms using nanowatts of optical power only. The transmission bandwidth, defined here as the spectral region with an attenuation $< 250\,\mathrm{dB\,km^{-1}}$, is specified as 820 nm ± 50 nm. Figure 3.1(a) shows a scanning electron image of the actual fiber we use in the experiment. The core and the surrounding crystal structure can be clearly identified. The intensity of the guided Gaussian mode (overlayed in Figure 3.1(a)) exhibits a $1/e^2$ mode field diameter of 5.5 µm. While not specified by the manufacturer, careful analysis of the birefringence of our fiber [82] showed that linear polarization is maintained in our fiber. The measured polarization beat length of our fiber is 8.0(8) mm which is of the same order of magnitude as standard commercial polarization-maintaining step-index fibers. We expect the slight asymmetry due to the ellipticity of the core itself and the two larger holes next to it (see Figure 3.1(a)) to be the reason for these (compared to other HCPBGFs) rather favorable polarization maintaining properties [83]. The ability to guide and maintain two orthogonal linear polarization components will become crucial for the filtering scheme in our SFWM experiments (see Section 4.2.1).

3.2 Spectral Properties of Rubidium

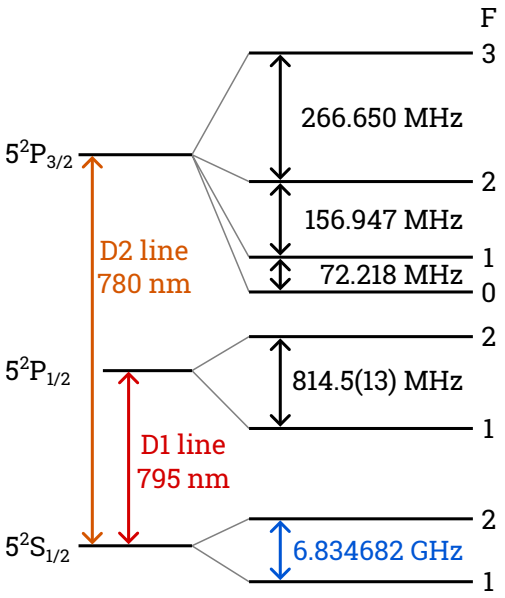

Figure 3.2: Level scheme of the ^{87}Rb D1 and D2 lines including the hyperfine structure. Values from [84] and not shown to full precision.

We perform all our experiments in the Rubidium (Rb) isotope ^{87}Rb, which is quasi-stable due to a nuclear lifetime of 4.88×10^{10} years [84]. As an alkali metal, Rubidium has only a single electron in the outermost (O-) shell and can thus be treated in analogy with the simple hydrogen atom [85].

Figure 3.2 shows the relevant part of the level scheme, i. e., the fine structure doublet of the D line. Due to the spin-orbit coupling, the excited state splits into states $|5^2P_{1/2}\rangle$ and $|5^2P_{3/2}\rangle$. The optical transitions to the common groundstate $|5^2S_{1/2}\rangle$ are termed D1 and D2 line respectively. These near-infrared transitions are separated by about 15 nm and can thus be addressed independently by narrowband lasers. The coupling between the total angular momentum of the electron $\vec{J}$ and the nuclear spin $|\vec{I}| = 3/2$ yields the total atomic angular momentum $\vec{F} = \vec{J} + \vec{I}$. The resulting hyperfine splitting is shown in Figure 3.2. Additionally, each hyperfine state further splits into $2F + 1$ Zeeman states in the presence of a weak magnetic

[1] NKT Photonics, *HC-800-02*

field. For the majority of this work though and whenever not stated otherwise, we do not lift the degeneracy of the Zeeman states. Hence, we can label states by their quantum number $|F\rangle$ and for simplicity introduce $|F'\rangle$ for excited states.

The natural line widths Γ_i of the optical transitions are given in Table 3.1 together with the corresponding life times $1/\Gamma_i$ of the excited state. The natural line widths determine the characteristic frequency scale of our experiments and throughout this work we will typically state (Rabi-) frequencies in units of Γ_i.

transition	D1 line	D2 line
natural line width	$\Gamma_{D1} = 2\pi \times 5.7500(56)\,\mathrm{MHz}$	$\Gamma_{D2} = 2\pi \times 6.0666(18)\,\mathrm{MHz}$
life time	27.679(27) ns	26.2348(77) ns

Table 3.1: Natural line widths (full width at half maximum) and corresponding lifetimes for ^{87}Rb. Values from [84].

As only transitions with $\Delta F = 0, \pm 1$ are allowed [86], the D2 line exhibits a cycling transition $|F = 2\rangle \leftrightarrow |F' = 3\rangle$ that is commonly used to implement magneto-optical cooling and trapping of the atoms (see Section 3.4.1 and Figure 3.6).

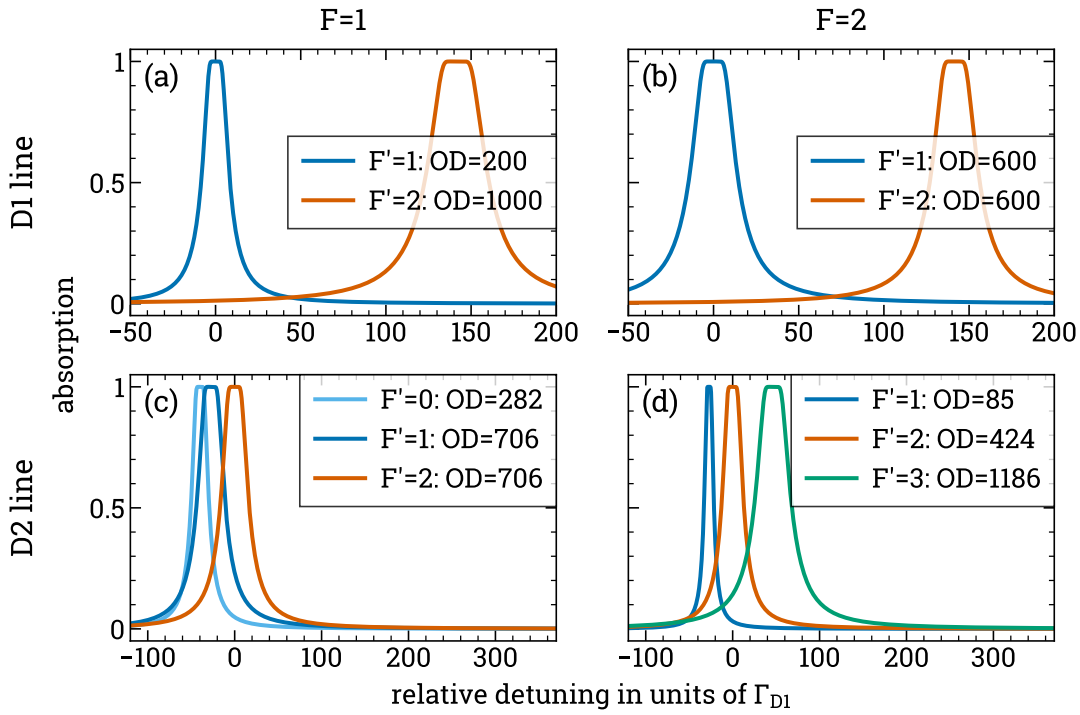

Figure 3.3: Calculated absorption spectra for all allowed hyperfine transitions within the level scheme shown in Figure 3.2. Columns correspond to the same ground state while rows correspond to transitions of the same fine structure line. We assume a reference OD of 200 on the $|F = 1\rangle \leftrightarrow |F' = 1\rangle$ transition on the D1 line. All other ODs are scaled using their respective transition dipole matrix elements given in [84]. We assume equally populated, degenerate Zeeman states.

In Figure 3.3 we compare the relative transition strengths of all allowed transitions within the level scheme shown in Figure 3.2. We observe, that at high

optical depths $\gtrsim 200$ the absorption lines of the different hyperfine transitions on the D2 line overlap significantly. This effect can prevent an efficient application of coherent techniques such as EIT and was avoided in previous work by limiting the *OD* (via the number of atoms) used in EIT-based experiments [87, 88]. This problem can be reduced substantially by performing these experiments on the D1 line [82] due to the larger frequency separation between the two excited states. However, as the preparation of cold atoms and subsequent HCPBGF loading is still performed on the D2 line, this solution requires additional laser systems to be able to drive transitions on both the D lines.

3.3 Laser Setup

We now introduce the laser system required to couple the hyperfine transitions of our medium on both the D1 and D2 line. Due to the large ground state splitting of 6.8 GHz, we use two separate laser systems on each line to be able to couple all relevant transitions. In total we use four external cavity diode lasers (ECDLs) and an additional free running diode laser.

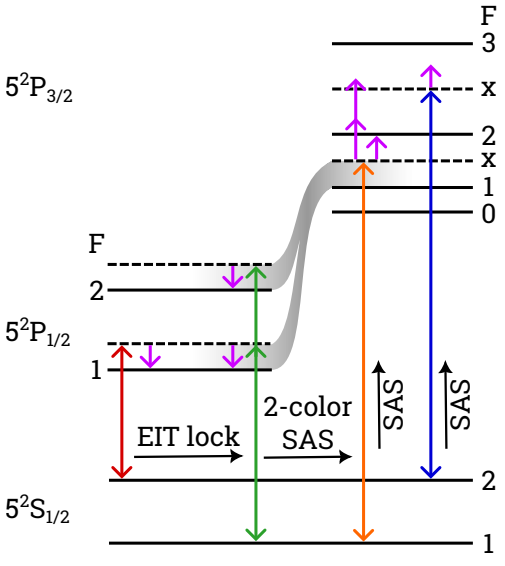

Figure 3.4: Laser locking scheme. The double arrow heads on the D1 line show the two possible locking options on the D1 line. Purple arrows are frequency shifting AOMs.

The ECDLs are home-built using two slightly different variations of the standard Littrow configuration [89, 90]. They each consist of a temperature stabilized laser diode[2] combined with a diffraction grating[3]. The −1st diffraction order of the grating is coupled back to the diode to form an external resonator that provides frequency feedback and tunability via a rotation of the grating. The ECDLs output power is about 100 mW per laser system. They are actively frequency stabilized on Rubdidium-based frequency references using the locking scheme shown in Figure 3.4. Figure 3.5 correspondingly shows the simplified optical setup to obtain the required reference signals. ECDLs 1 and 2 on the D2 line are locked onto the crossover signals $|F = 1\rangle \leftrightarrow |F' = 1\rangle \times |F' = 2\rangle$ and $|F = 2\rangle \leftrightarrow |F' = 2\rangle \times |F' = 3\rangle$ respectively. We obtain these by performing standard Doppler-free saturated absorption spectroscopy (SAS) [91, 92] in two separate heated Rubidium vapor reference cells. To drive the transitions of the D1 line, we lock ECDL 3 via a bichromatic version [93] of the SAS: We combine optical pumping by ECDL 1 at the D2 line with probing by ECDL 3 at the D1 line to transfer the frequency offset of the lock from the D2 to the D1 line. We note, that

[2]ECDL 1+2: Thorlabs, *L785P090*; ECDL 3+4: Thorlabs, *L785H1*
[3]Thorlabs, *GH13-18V*

depending on the planned experiment we can implement the same locking scheme on the D1 line using excited state $|F' = 1\rangle$ or $|F' = 2\rangle$. The measured transmission signals are fed back to FPGA-based laser locking electronics[4] that controls the laser diodes current driver[5] and a piezoelectric actuator that tunes the angle of the diffraction grating. With an optical spectrum analyzer[6] we measured line widths of about 500 kHz for the frequency locked ECDLs [93], i. e., more than order of magnitude below the natural line widths of the Rubidium hyperfine transitions.

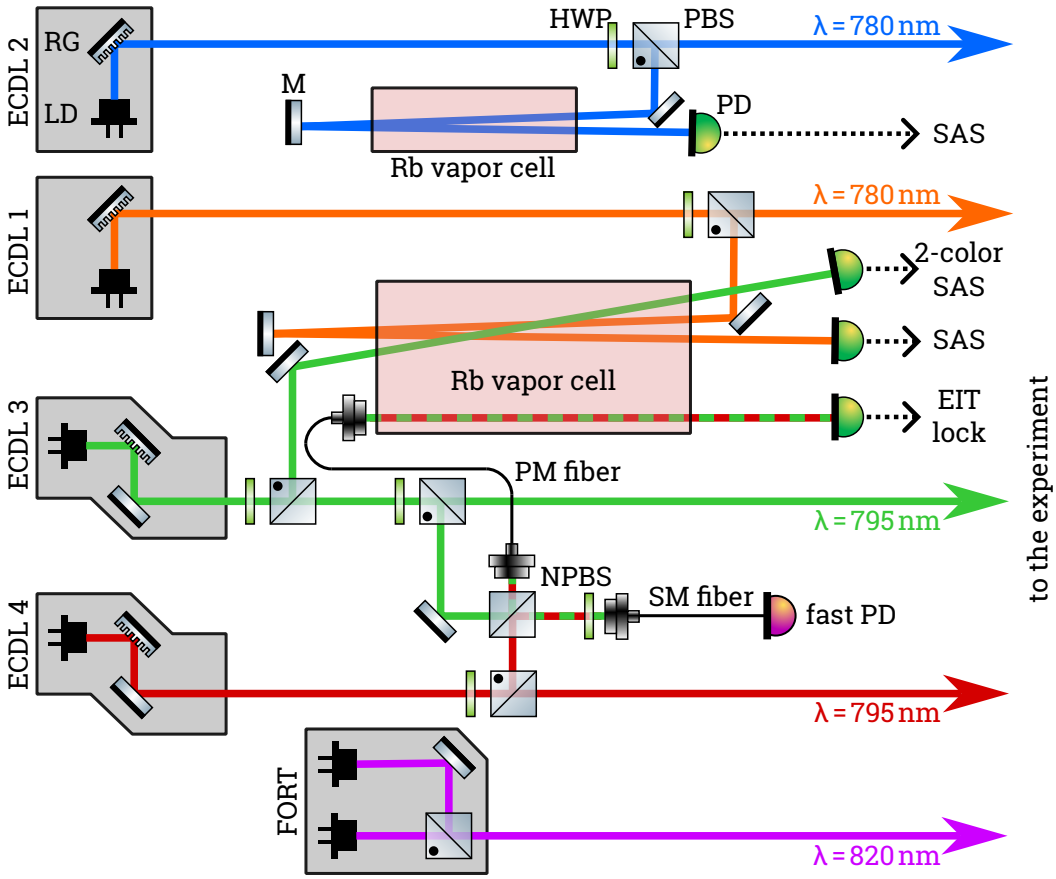

Figure 3.5: Simplified laser and frequency locking setup. Solid arrows depict light beams with the colors corresponding to the locking scheme in Figure 3.4. Dashed black arrows depict electronic signals. For simplicity we omit here the feedback loops of the stabilization signals back to the lasers. LD: laser diode, RG: reflective diffraction grating, HWP: half-wave plate, (N)PBS: (non-)polarizing beamsplitter, M: mirror, PM/SM: polarization-maintaining/single-mode fiber, and PD: photodiode

The locking scheme we described so far serves primarily to prevent drifts of the laser frequencies relative to the Rubidium transition frequencies. It does not, however, provide a fixed phase relation between the different lasers as is required to observe coherent effects involving multiple fields. To observe EIT based effects (used for the characterization of our medium in Section 3.5) on the D1 line, we lock the frequency of ECDL 4 to that of ECDL 3 with a fixed frequency offset of

[4]Toptica, *DigiLock 110*
[5]Home-build low noise diode driver, design by the group of T. Walther, TU Darmstadt
[6]Sirah Lasertechnik, *EagleEye FC*

6.8 GHz corresponding to the groundstate splitting between $|F = 1\rangle$ and $|F = 2\rangle$. To obtain a suitable reference signal we overlap both lasers within a PM fiber and guide them through the Rubidium reference cell before detecting the spectroscopy signal with a PD. In the presence of a second field, EIT renders the medium transparent for the first field. The EIT window can be spectrally narrow compared to the natural line width of Rubidium and is centered on the two-photon resonance (see Section 2.2 for details on EIT). We use a Pound-Drever-Hall stabilization [94, 95] to lock the frequency of ECDL 4 onto this EIT reference. We monitor the spectrum of the microwave beat signal by overlapping the locked lasers on another fast PD[7] and observe a relative line width of a few 10 kHz. For a detailed explanation of this stabilization method we refer the reader to [87, 96].

The additional laser system used for the optical dipole trap is independent of the lasers and locking scheme we described so far and will be introduced in Section 3.4.2.

We choose all setpoints for the frequency stabilization such that acousto-optical modulators (AOMs) [97] can be used to shift the light's frequency from the lock point to the required frequency for the respective beam in the experiment. Depending on the desired frequency shift, we use the AOMs (indicated by purple arrows in Figure 3.4) in standard single- or double-pass [98] configuration or an acousto-optical shutter [99] configuration that allows intensity modulation without changing the lights frequency. Using the AOMs we achieve switching times of about 100 ns.

3.4 Preparation of Cold Atoms in a Hollow-Core Fiber

3.4.1 Magneto-Optical Trapping

Prior to loading atoms into the HCPBGF we trap and cool an ensemble of Rubidium atoms in a magneto-optical trap (MOT). The majority of the setup for preparing cold atoms and subsequently load them into the HCPBGF was designed and implemented by F. Blatt and T. Peters in previous work. We only summarize here the relevant techniques and refer the reader to to textbooks, e. g., [100] for a general introduction into laser cooling and trapping and to [87] for further experimental details of our setup.

Our experiments are performed within an ultra-high vacuum (UHV) cell[8] at a background pressure of $\leq 10^{-9}$ mbar to minimize collisions with background gas. We use a glass cell for full optical access from five directions. Rubidium atoms, i. e., ^{87}Rb and ^{85}Rb in their natural isotopic abundance ratio of 27.8 % to 72.2 %, are introduced into the cell by means of a heated dispenser[9].

We use laser cooling to slow down the atoms, i. e., reduce their temperature. Figure 3.6 (rhs) shows the corresponding coupling scheme. We apply a *cooling and trapping* beam with a red detuning of $-3\,\Gamma_{D2}$ from the transition $|F = 2\rangle \leftrightarrow |F' = 3\rangle$. Due to the Doppler effect the red detuned cooling light is predominantly absorbed

[7] Hamamatsu, *G4176-03*
[8] Japan Cell, 70 × 25 × 25mm
[9] SAES Getters, *Rb/NF3.4/12*

by atoms that are moving in the opposite direction of the light propagation. As the subsequent photon emission by the atom is isotropic, this process of absorption and reemission effectively reduces the atomic velocity. As the initial velocity distribution is isotropic, we apply cooling light from all six spatial directions to effectively cool our sample. Due to selection rules (see Section 3.2), population in state $|F' = 3\rangle$ can only decay into $|F = 2\rangle$ from where the atom can again absorb trapping photons. This so called cycling transition makes the level scheme of the D2 line optimally suited for laser cooling and trapping. Nevertheless, some atoms will be off-resonantly absorbed into $|F' = 2\rangle$ and can subsequently decay into ground state $|F = 1\rangle$. To pump these atoms back into the cooling cycle, we apply a *repumping* beam resonant with the transition $|F = 1\rangle \leftrightarrow |F = 2'\rangle$.

In addition to laser cooling, we use magneto-optical trapping to spatially confine the cold atoms. We use a pair of anti-Helmholtz coils to create a magnetic quadrupole (QP) field with the spatial zero crossing of the field in the center of the six overlapped cooling and trapping beams. We choose the (circular) polarisation of the trapping beams such that the energy levels for atoms away from the traps center are shifted into resonance (due to the Zeeman effect) and predominantly absorb photons with an impulse towards the trap center. This yields an effective force towards the trap center. Combined with laser cooling, the MOT prepares a sample of cold and spatially localized atoms. To shield our experiment from external magnetic fields, i. e., mainly the earths magnetic field and that of the UHV ion getter pump, we use three pairs of shimming coils in Helmholtz configuration. Additionally, we can use the shimming coils to change the position of the zero crossing of the QP field by applying an additional homogeneous field.

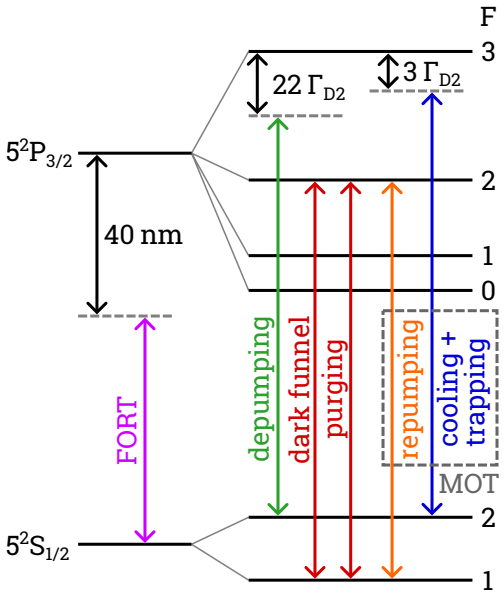

Figure 3.6: Coupling scheme on the D2 line for the MOT and subsequent loading of the cold atom sample into the HCPBGF. The detuning of the depumping beam is chosen so that it is shifted into resonance for atoms inside the HCPBGF due to the AC stark shift induced by the dipole trap (see Section 3.4.2).

In contrast to a standard spherical MOT, we use rectangular QP coils, resulting in field gradients of [87] 8.1 G cm^{-1} (horizontal) and 0.04 G cm^{-1} (vertical). This leads to a prolate shape with $1/e^2$ diameters of about [87] 3.9 mm × 1.4 mm of the cold atom cloud which is favorable for the transfer into the HCPBGF (see the following Section 3.4.2). By monitoring the atoms fluorescence with a calibrated CCD camera, we infer the number of atoms in the cloud to be $7(1) \times 10^6$ after a loading time of 1 s [72]. The temperature of the atomic ensemble prior to loading the HCPBGF can be measured using the established time-of-flight method [101], i. e., we monitor the expansion of the atom cloud versus time after switching off the MOT. The observed temperature is about 30 µK after a 10 ms phase of polarization-gradient cooling [87].

3.4.2 Transfer of Cold Atoms into the HCPBGF

After loading the MOT with cold atoms, we begin the transfer of the atoms into a far-off resonant dipole trap (FORT) guided within the HCPBGF. Figure 3.7(a) shows the relevant part of the setup. The HCPBGF is mounted (upper mount rendered yellow) vertically within the UHV cell at a distance of 5.5 mm below the center of the MOT. Gravity will thus accelerate the atoms towards and, after loading, through the HCPBGF. We can couple light fields (rendered green) into the fiber from both ends. Optimizing the coupling from free space to the Gaussian mode guided in the core of the HCPBGF is not trivial, though. In contrast to a step-index fiber, light can not only be transmitted in the Gaussian mode of the core but also propagate in higher modes through the surrounding structure. Hence, a simple optimization of the transmitted power is not sufficient for good alignment. Instead, we initially use a camera to monitor the transversal profile of the transmitted light and optimize for a clean Gaussian profile. Subsequently, we align another (step-index) single-mode fiber for maximal overlap with the light transmitted through the HCPBGF. Now, the second fiber acts as a spatial filter that isolates the transmission of the Gaussian HCPBGF mode from higher order modes and allows us to maximize the coupling efficiency to the Gaussian mode. Using this optimization technique, we achieve a coupling efficiency of $\gtrsim 90\,\%$ for the FORT coupled into the HCPBGF from below. For the experimental beams coupled into the fiber at the top end we achieve a coupling efficiency of 64 %. The difference can be explained by the spatial limitations of the setup. As shown in Figure 3.7(a), the coupling lens (rendered blue) on the lower fiber end is positioned at an optimized distance within the UHV setup. Above the fiber, however, we have to prepare the MOT and load the atoms into the fiber. Therefore, the coupling lens (rendered blue) on the upper fiber end is positioned above the UHV cell. This leads to imperfect mode matching and, thus, limited coupling efficiency.

Because the fiber core diameter (7 µm) is three orders of magnitude smaller than the diameter of the Rubidium cloud in the MOT (about 1.4 mm), we have to match the position as well as the cloud diameter carefully to obtain a high transfer efficiency of the atoms from the MOT into the HCPBGF. Figure 3.7(b) shows the temporal sequence of this loading process. All timings are controlled by a 24-channel FPGA-based programmable pulse generator[10] and an digital-to-analog output card[11] both controlled via home-made LabVIEW-based software. As explained in the previous section, we start by cooling and trapping an ensemble of atoms in the MOT for about 1 s. Subsequently, we start the transfer process into the HCPBGF by magnetically shifting the atomic clouds position towards the fiber. This shift is implemented by applying a vertical offset field B_z using the shimming coils. To facilitate an efficient transfer into the fiber core, we simultaneously compress the cloud magnetically by linearly increasing the current and, hence, the gradient in the QP coils. This increases the trapping force on the atoms and leads to stronger radial confinement. Simultaneously, we continuously increase the trapping detuning during from $-3\Gamma_{D2}$ to $-6\Gamma_{D2}$ for optimized polarization-gradient

[10] SpinCore, *PulseBlaster PB24-100-4k-PCIe*
[11] National Instruments, *PCI-6110*

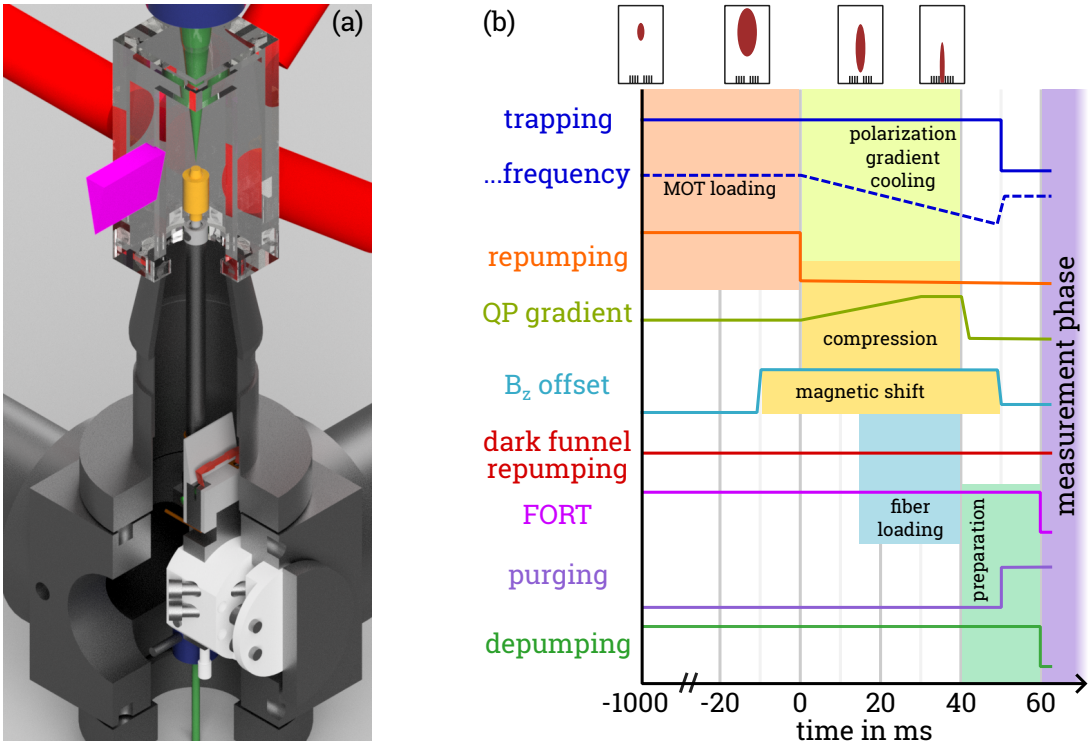

Figure 3.7: (a) Simplified rendered image of the experimental setup for the preparation of cold atoms within the HCPBGF. The cooling and trapping beams (red) are applied from all six directions (we omit here the counterpropagating beams for clarity). The dark funnel repumping beam (pink) is applied from two orthogonal directions. Yellow: fiber mount, red: Rubidium dispenser, green: optical mode coupled through the fiber, blue: coupling optics within and above the UHV setup. Adapted from [87] (modified). (b) Temporal sequence of the HCPBGF loading cycle. The cold atomic ensemble is captured in the MOT and subsequently transferred into the fiber. All solid lines are amplitudes. The shaded areas indicate different phases of the experiment that are explained in detail in the main text. The cycle is repeated at 0.8 Hz.

cooling (PGC) [100] cooling during the compression. In principle, PGC requires a vanishing QP gradient, however, in our prolate MOT geometry the gradient in the longitudinal direction is weak enough for PGC to reduce the temperature of the ensemble and thus increase the number of atoms that we subsequently load into the HCPBGF.

The temporal changes in the magnetic fields between loading the MOT and transferring the atoms into the fiber prevents us from continuously feeding new atoms into the fiber during our measurements. Instead, the whole experiment runs on a periodic *MOT cycle* with a repetition rate of 0.8 Hz. When we compare the 1 s loading time of the MOT to the duration of a measurement phase of a few ms we find a duty cycle of the order of $\eta_{\text{duty}} \approx 0.001$. While acceptable for our principal demonstrations in this work, the duty cycle limits the application of our photon-pair source in the context of larger experiments. We discuss concepts to overcome this limitations in Section 5.5.

In addition to the magnetic shift and compression, we use a *dark funnel* repumping beam to optimize the transfer of atoms into the HCPBGF. The technique is based on the dark-spot [70, 102] MOT technique. By imprinting a shadow in the

center of the beam profile of the repumping beam, atoms within the shadowed region will no longer be pumped back into the trapping cycle and thus accumulate in the *dark* ground state $|F = 1\rangle$. Removing the atoms from the trapping cycle reduces heating due to scattering and collisions and leads to an increased atomic density in within the dark spot region. We use a funnel-shaped dark spot to continuously increase the confinement of the atoms during their transfer towards the fiber tip. Additionally, a counter-propagating *depumping* beam is applied through the HCPBGF. It increases the effect of the dark funnel in increasing the density above the fiber tip by actively pumping the atoms into $|F = 1\rangle$ and out of the pumping cycle [103]. Without the depumping beam light from the cooling and trapping beams scattered from the various cell surfaces into the dark funnel region can still be scattered by the atoms and reduce the effect of the dark funnel. By combining these techniques, we obtain atomic densities of the order of $10^{12}\,\mathrm{cm}^{-3}$ [87]. Note, that the dark funnel repumping beam and the depumping beam are not temporally modulated during the MOT and HCPBGF loading phases. As the dark funnels power is only 1/60 of the standard MOT repumping, the dark funnel only becomes relevant once we block the standard MOT repumping beam with a mechanical shutter. Due to the NA of 0.15, the depumping beam strongly diverges from the fiber tip (compare the FORT intensity distribution over the HCPBGF in Figure 3.8(a)) and, therefore, its intensity is not sufficient to significantly alter the population distribution of atoms still in the MOT at distance from the fiber tip.

Far-off Resonant Dipole Trap For the actual transfer of the atoms into the HCPBGF we use the FORT. In a dipole trap, a strong light field induces an atomic dipole moment. The interaction of this induced dipole with the electric field is described by the interaction potential U_F. When we assume a detuning that is small compared to the light frequency, i. e., $|\Delta| \ll \omega_0$, we can write the FORT potential as [104]

$$U_\mathrm{F}(\vec{r}) = \frac{3\pi c^2}{2\omega_0^3}\frac{\Gamma}{\Delta} I(\vec{r}) \tag{3.1}$$

with the radial intensity distribution $I(\vec{r})$. It is obvious that depending on the sign of the detuning atoms are either attracted or repelled by intensity maxima. However, due to the single-mode guidance in the HCPBGF we are restricted to a red detuned FORT configuration with $\Delta < 0$ and a Gaussian $I(\vec{r})$. For given experimental parameters, we can calculate the resulting trap temperature depth T_F using $U_\mathrm{F} = k_\mathrm{B} T_\mathrm{F}$ with the Boltzmann constant k_B. To consider the influence of both the D1 and D2 lines, we can rewrite Equation (3.1) for the case of a linear polarized FORT as [104]

$$U_\mathrm{F}(\vec{r}) = \frac{\pi c^2 \Gamma_\mathrm{D2}}{2\omega_\mathrm{D2}^3}\left(\frac{2}{\Delta_\mathrm{D2}} + \frac{1}{\Delta_\mathrm{D1}}\right) I(\vec{r}) \tag{3.2}$$

where Δ_D1 (Δ_D2) is the detuning of the FORT from the resonance frequency $\omega_\mathrm{D1}(\omega_\mathrm{D2})$ of the respective line. For a given ensemble temperature T, the resulting

density distribution is given by [104]

$$\mathcal{N}(\vec{r}) = \mathcal{N}_0 \exp\left(-\frac{U_{\mathrm{F}}(\vec{r}) - U_{\mathrm{F}}(\vec{0})}{k_{\mathrm{B}} T}\right), \tag{3.3}$$

where $\mathcal{N}_0$ is the peak atomic density.

We implement the FORT using a separate free running diode laser system (shown in Figure 3.5). It combines the output of two orthogonally linear polarized diodes[12] each emitting a power of about 200 mW at a wavelength of 820 nm. Active stabilization is not necessary for this system as the laser field is far detuned by ~ 25 nm from the nearest Rubidium resonance and hence frequency fluctuations in the GHz regime can be neglected. The combination of two independent laser diodes allows a stable operation at two different frequencies. Such multi-mode operation has been shown to improve the optical depth in the HCPBGF by a factor of 2 to 5 compared to single-mode operation [87]. We assume the following reason: When we couple a Gaussian beam into our HCPBGF a small fraction ($\simeq 1\,\%$) of the radiation is guided not in the Gaussian mode of the core but in surface modes of the surrounding periodic cladding structure [105]. For a single longitudinal frequency mode, these cladding modes can interfere with the Gaussian mode in the core. The interference pattern leads to a periodic variation of the FORTs trap potential which in turn can lead to parametric heating of the atoms when the modulation frequency is close to the trap frequency [106, 107]. For a FORT combined out of two longitudinal modes, this effect is averaged out when the beating between the two FORT modes is fast compared to the atoms movement in the modulated trap potential.

The FORT is aligned through the HCPBGF from below, counter-propagating to the experimental beams, to minimize noise contributions of the strong FORT in our experiments. In Figure 3.8(b) (blue solid line) we plot the trap potential given by Equation (3.2) for a Gaussian intensity distribution and a power of 100 mW that we typically couple into the HCPBGF. The resulting peak trap depth[13] is $T_{\mathrm{F}} \lesssim 7.2\,\mathrm{K}$. As the trap light diverges from the (upper) fiber tip, the potential depth decreases fast with the distance to the fiber tip as visualized in Figure 3.8(a). For an ensemble temperature of 30 µK prior to loading, the atoms are trapped as soon as they enter the colored area. We thus position the atom cloud with a radial (vertical) precision of about 30 µm (400 µm). Once cold atoms with a suitable temperature $\leq T_{\mathrm{F}}$ come close enough to the fiber tip to be trapped in the FORT they will be guided into the fiber core.

In addition to guiding the atoms into the fiber, the FORT also prevents the ensemble from expanding within the fiber core and getting in contact with the (hot) fiber walls. Such collisions with the walls result in losses of atoms and therefore have to be avoided. Figure 3.8(b) shows the FORT potential inside the HCPBGF together with a Gaussian approximation for the atomic density distribution [72, 108]. The intensity of the FORT varies over the spatial extend of the atomic ensemble. This leads to spatially inhomogeneous AC-stark shifts of the

[12] Thorlabs, *L820P200*

[13] We note, that our calculations yield twice the trap depth compared to previous work [72, 87] were an incorrect intensity distribution $I(r)$ was used.

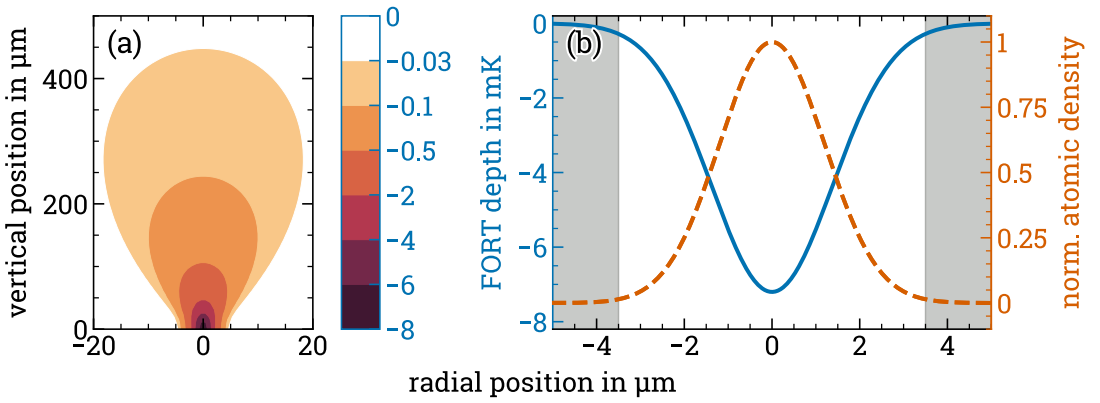

Figure 3.8: Far-off resonant dipole trap. (a) Spatial dependence of the trap depth above the fiber tip positioned at the coordinate origin. (b) Radial dependence of the trap depth (blue solid line) and the resulting atomic density distribution (orange dashed line) within the fiber, calculated using Equations (3.2) and (3.3). We assume a Gaussian intensity distribution $I(r) = I_0 \exp(-2r^2/w_0^2)$ with $I_0 = 2P/(\pi w_0^2)$, $P = 100\,\mathrm{mW}$, and $2w_0 = 5.5\,\mu\mathrm{m}$. The beam waist w_0 is the $1/\mathrm{e}^2$ radius of the intensity and correspondingly the $1/\mathrm{e}$ radius of the Rabi frequency for all fields guided in the HCPBGF. The Gaussian approximation $\mathcal{N}(r) = \mathcal{N}_0 \exp\left(-r^2/\sigma_a^2\right)$ of the atomic density exhibits an $1/e$ radius of $\sigma_a = 1.7\,\mu\mathrm{m}$. The diameter of the hollow core (between grey shaded areas) is $7\,\mu\mathrm{m}$. Adapted from [87] (modified).

atomic transitions which result in significant inhomogeneous line broadening and thus decoherence in our experiments. To avoid this, we periodically switch off the dipole trap for *measurement windows* in which the ensemble is expanding freely before we switch the FORT back on and recapture the ensemble. Due to the finite temperature of the sample, we are limited to measurement window lengths of roughly 2 µs. We choose a modulation frequency of 250 kHz for the FORT intensity to avoid parametric heating when modulating the FORT at frequencies $2\omega_r/n$ with integer n [109]. Here, $\omega_r = \sqrt{4U_\mathrm{F}(0)/(mw_0^2)} \approx 2\pi \times 100\,\mathrm{kHz}$ is the FORTs trap frequency [104] calculated using the atomic mass m [84]. We will introduce the pulsed measurement sequences in detail in their respective sections.

In a last step, after the loading of the HCPBGF and before we start any measurements, we prepare the ensemble inside the HCPBGF for the experiments by pumping all of the population into $|F = 1\rangle$. Any atoms that may have remained above the fiber, however, are pumped into $|F = 2\rangle$ by a strong *purging* beam and thus rendered transparent for a probe beam coupling to $|F = 1\rangle$.

3.5 Characterization of the Medium

We now turn to characterizing the ensemble of cold atoms in the HCPBGF in terms of the number of atoms, temperature, *OD*, coherence time, and EIT conditions. Because we will perform many repetitions of our experiments with the same set of atoms, we include the temporal dynamics in most of these measurements.

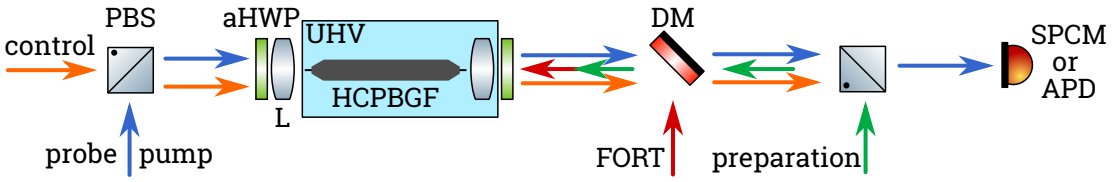

Figure 3.9: Simplified experimental setup to characterize the cold atoms inside the HCPBGF. Depending on the measurement the detector is a single photon counting module (SPCM) or an avalanche photo diode (APD). UHV: ultra-high vacuum cell, aHWP: achromatic half-wave plate, L: lens, DM: dichroic mirror, PBS: polarizing beamsplitter.

Figure 3.9 shows the optical setup we use for the measurements presented in this section. We couple the measurement beams (i. e., probe, pump, and control, depending on the specific measurement) into the HCPBGF from the top, counterpropagating to the FORT and a preparation beam. The preparation is implemented using the same beam as the depumping introduced in the previous section.

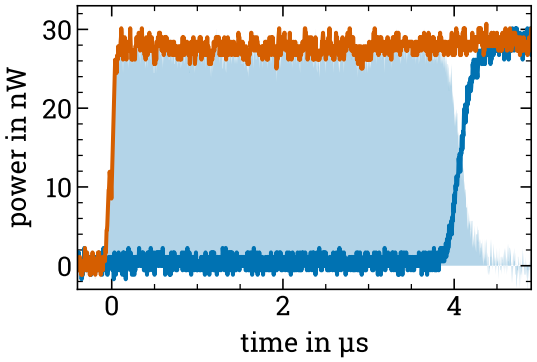

Figure 3.10: Exemplary measurement (blue line) of the transmitted pump power versus time for a number of atoms $N = 215 \times 10^3$. The orange line is the reference signal obtained without loading atoms into the fiber. The signal difference (shaded area) is proportional to N. The plotted power is compensated for all transmission losses from the HCPBGF to the APD.

Number of Atoms To determine the number of atoms N within the HCPBGF we cannot measure the atoms fluorescence due to the restricted optical access. Instead, we perform time-resolved optical pumping [102, 110]. We start with the population fully in state $|F = 1\rangle$. After the MOT and FORT are switched off, we apply a strong purging beam above the fiber to pump any remaining atoms over the HCPBGF into $|F = 2\rangle$ to avoid including them in the counting process. Subsequently, we apply a pump beam resonant with the $|F = 1\rangle \leftrightarrow |F' = 2\rangle$ transition on the D1 line. We monitor the transmission of the beam through the fiber on a calibrated avalanche photo diode[14] (APD). Figure 3.10 shows such a transmission measurement with and without atoms loaded into the HCPBGF. The

[14] Laser Components, *SAR500H1B*

integrated difference of the two signals corresponds to the necessary energy to pump all atoms into $F = 2$ and hence render the medium transparent for the pump beam. As the branching ratio for the decay from $|F' = 2\rangle$ into the two ground states is $1 : 1$, the average atom absorbs 2 photons of energy hc/λ before it is pumped into $|F = 2\rangle$. Using the measured transmission from the HCPBGF to the APD of 0.42 and the APD gain of $8.41 \times 10^6\,\mathrm{V\,W^{-1}}$ we obtain the number of atoms in the HCPBGF. In a typical measurement we load the HCPBGF with up to 250×10^3 atoms which corresponds to a loading efficiency of about 2.5 % for 10×10^6 atoms in the MOT. This value is in good agreement with previous work [70] and the results reported in [76]. To quantify the stability and repeatability of the HCPBGF loading, we measured the number of atoms for 500 consecutive loading cycles and obtained a relative standard deviation of 3.5 % in N.

Ensemble Temperature within the Hollow-Core Fiber We cannot apply the standard method of observing the fluorescence of an expanding atomic cloud within the HCPBGF because the optical access is restricted to observing light propagating along the fiber axis. Instead, we perform an absorption based time-of-flight measurement within in the HCPBGF. We switch of the guiding FORT and perform time-resolved measurements of the reducing number of atoms in the ensemble due to collisions with the fiber walls [111]. Systematic comparison of the experimental data with a calculation based on the Gaussian atomic density distribution yields a steady-state temperature of 1.0(4) mK [72].

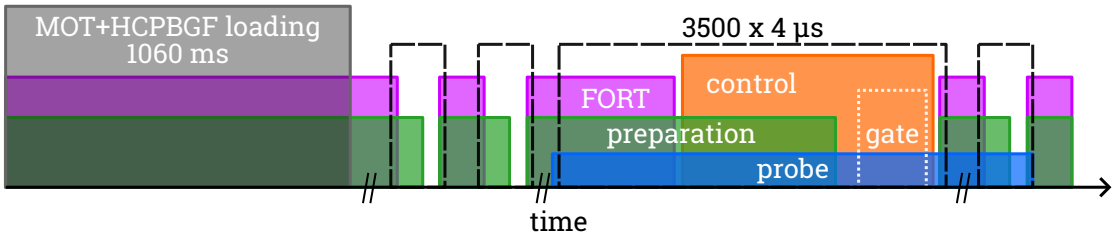

Figure 3.11: Simplified temporal sequence for absorption spectroscopy. With the control pulse active we measure an EIT spectrum, without it an absorption spectrum to determine the OD. We repeat this sequence alternating between loading and not loading the HCPBGF with atoms to include a reference measurement for each loading cycle. The probe frequency is repeatedly chirped over the resonance with a period of 200 µs, i. e., 50 measurement windows. We hence acquire 70 consecutive spectra per loading cycle. We only acquire data during the visualized gate period.

Optical Depth The *OD* can be measured directly via absorption spectroscopy. We use a weak probe pulse on the $|F = 1\rangle \leftrightarrow |F = 1\rangle$ transition to not alter the population distribution. Due to the small mode diameter of the guided fiber mode, this requires us to use probe powers of only a few pW. Therefore, we use a single-photon counting module[15] (SPCM) to detect the transmitted light. As our medium exhibits an $OD \gg 10$, a simple resonant probe pulse would be fully absorbed in the medium. We, therefore, have to acquire a full spectrum by

[15] Excelitas, *SPCM-AQRH-13*

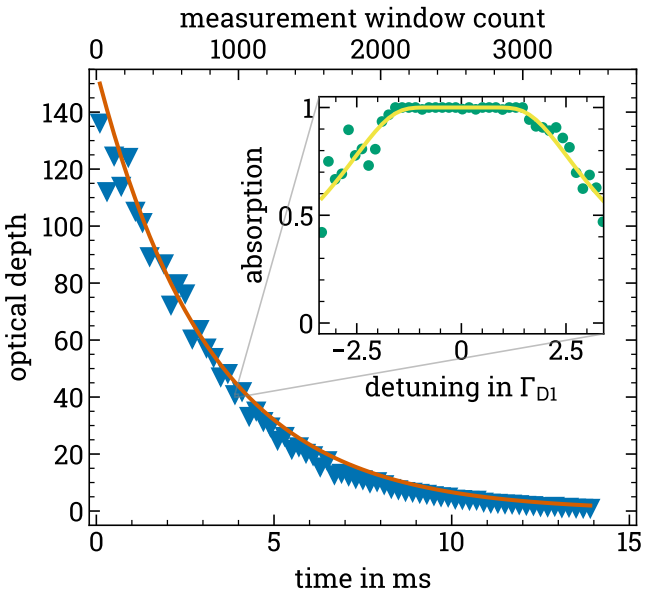

Figure 3.12: OD versus time after loading the HCPBGF (blue triangles) fitted with an exponential decay (orange solid line) yielding a time constant of $\tau_{OD} = 3.2(2)\,\mathrm{ms}$. The upper axis depicts the number of $4\,\mu\mathrm{s}$ measurement window periods. The inset shows one example of a measured absorption spectrum (green dots) with an OD of 45 determined by a fitted Lorentzian line shape (yellow solid line).

chirping the probe frequency over the resonance frequency. The experimental sequence is shown in Figure 3.11. Note, that the control pulse shown in the figure is required only to measure EIT spectra and remains switched off to measure a standard absorption spectrum. As explained in Section 3.4.2, we have to avoid the perturbing influence of the strong FORT by periodically switching it off. For each of these windows, we prepare the population in $|F = 1\rangle$ via the strong preparation beam. We subsequently detect transmitted probe photons in a defined temporal gate within the FORT window only.

The inset of Figure 3.12 shows an example of such a spectrum. We fit the measured absorption spectra with a Lorentzian line shape and subsequently use Beer's law (2.17) to obtain the resonant *OD* defined in Equation (2.18). To quantify the loss of atoms due to the pulsed FORT over time, we repeat the *OD* measurement within a single MOT and HCPBGF loading cycle (i. e., with the same ensemble of atoms) until all atoms are lost due to expansion and collisions with the fiber wall. In Figure 3.12 we show the decay of the *OD* over 3500 FORT windows. An exponential fit yields a 1/e decay time of $\tau_{OD} = 3.2(2)\,\mathrm{ms}$. We thus limit all our measurements to 14 ms (corresponding to 3500 windows) to include the full range of available *OD*s. As the *OD* is proportional to N, we can also obtain the *OD* indirectly by measuring the number of atoms as described in the previous section. On the $|F = 1\rangle \leftrightarrow |F = 1\rangle$ transition of the D1 line we require about 1050 atoms for an $OD \approx 1$. In the HCPBGF the atoms are not equally distributed over the whole fiber length. Instead the ensemble with a length $L \approx 6\,\mathrm{cm}$ propagates through the fiber [72]. We neglect here the axial density distribution within the ensemble.

Ground State Coherence Time As introduced in Chapter 2, SFWM relies crucially on creating and maintaining a coherent superposition of the ground states $|1\rangle$ and $|2\rangle$. To quantify this ability for our medium, we measure the groundstate decoherence rate γ_{12} via EIT light storage (LS) [62, 82].

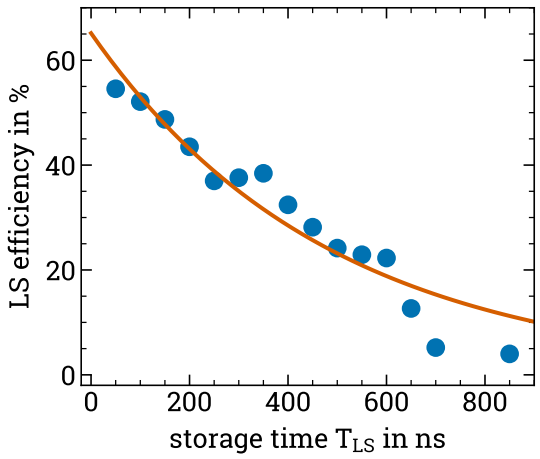

Figure 3.13: Light storage efficiency versus storage time (blue dots) with a fitted exponential decay (orange line). The resulting time constant is $\tau_{LS} = 483(48)\,\mathrm{ns}$.

In this protocol, we first apply a strong control field to render the medium transparent for a weak probe field via EIT. Once the probe pulse is inside the medium, the control field is switched off adiabatically and the probe field is converted into a collective coherence distributed over the atomic ensemble. After a storage time T_{LS} we switch the control field on again. The coherence is converted back into into a light field and can be detected after exiting the medium. We measure the storage efficiency, i. e., the fraction of the stored light that is read out again. In Figure 3.13 we show the resulting exponential decay of the storage efficiency. From the decay we extract a decoherence rate of $\gamma_{12} = 1/\tau_{LS} = 0.057(6)\,\Gamma_{D1} \approx 2\pi \times 330\,\mathrm{kHz}$. As introduced in Section 2.2, this is a fundamental limit for the line width of narrowband biphotons that could be generated in our medium. The observed deviations from an ideal exponential decay could be explained by residual magnetic fields. They lead to small Zeeman shifts that lift the degeneracy of the magnetic sub-levels and give rise to periodic dephasing and rephasing of read-out LS signals stored at slightly different frequencies in multiple Λ schemes [112]. We note here, that the value for γ_{12} measured by LS is a can increase due to inhomogeneous broadening of the ground state transition, e. g., due to spatially inhomogeneous AC Stark shifts induced by other light fields such as the FORT or the SFWM pump fields.

Electromagnetically Induced Transparency In our SFWM experiments, the EIT conditions determine the biphoton spectrum as introduced in Chapter 2. In addition, EIT allows the propagation of the generated AS photon through the otherwise opaque medium. To minimize absorption losses in the AS channel, we thus desire high transmission. At the same time, as we have to average over many repetitions of our experiment within one MOT loading cycle, we require comparable experimental conditions.

We measure EIT spectra using the same technique as in the measurement of the *OD*. We apply the same experimental sequence introduced in Figure 3.11 and add now the strong control field during the probing. In addition, the pump beam for the SFWM experiment (that will be introduced in the subsequent Chapter) is active to measure the EIT spectra under the same conditions as in the main experiment. In Figure 3.14 we show EIT spectra for four different *OD*s. We fit all spectra using Equation (2.17), with Ω_C as the only free parameter. In the upper row, we performed the experiment a fixed control power of 17 nW and obtain a Rabi frequency of $\Omega_C = 3.9\,\Gamma_{D1}$ from the fits. From left to right, we observe an increase in the width as well as the depth of the EIT window due to the decreasing

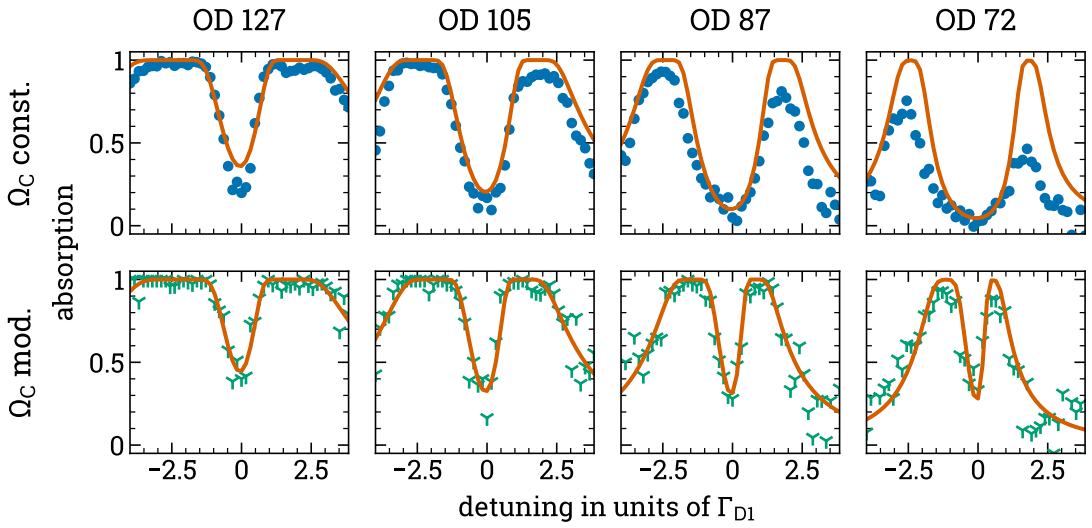

Figure 3.14: Electromagnetically induced transparency. Left to right: Decreasing OD following the decay measured in Figure 3.12. Upper row: A constant control Rabi frequency of $\Omega_C = 4.2\,\Gamma_{D1}$ leads to a broader EIT window with decreasing OD. Lower row: The temporally modulated $\Omega_C(t)$ maintains the line shape of the EIT window over a larger range of ODs. The solid lines are fits based on Equation (2.17). We use the measured values from Figures 3.12 and 3.13 for the OD and γ_{12}. A frequency offset of $-0.6\,\Gamma_{D1}$ for both the probe and control field accounts for the AC Stark shift induced by the SFWM pump beam.

OD. To be able to generate biphotons with similar spectral properties over a larger range of *OD*s, we temporally modulate $\Omega_C(t)$ to maintain an fixed width of the EIT window. For $|\delta| \ll \Omega_C^2/\Gamma_{D1}$ we can approximate the EIT bandwidth as [113] $\Gamma_{EIT} = \Omega_C^2\sqrt{\ln 2}/\Gamma_{D1}\sqrt{OD}$. To keep Γ_{EIT} fixed, we thus implement an exponential decay $\Omega_C(t)^2 \propto e^{-((t-t_0)/\tau_\Omega)}$ with $\tau_\Omega = 2\tau_{OD}$ where the factor of 2 accounts for the square root. We found experimentally, that it is beneficial to begin the modulation at $t_0 = 3.2\,\text{ms}$ because the *OD* dependence of the EIT width is larger for smaller *OD*s. In the lower row of Figure 3.14 we show the EIT spectra we observed using the modulated $\Omega_C(t)$. In comparison with the reference data, the *OD* dependence of the EIT width is significantly reduced. However, we still observe a slight narrowing of the EIT window with the decreasing *OD*. This can be explained by extracting the actual $\Omega_C(t)$ from fits of Equation (2.17) to the measured spectra. With $\tau_{\Omega_C} = 7.5\,\text{ms}$ the observed value is slightly larger than the theoretically optimal value of 6.4 ms leading to a narrowing of the EIT window over time. Still, the measurement confirms an improved stability of the EIT conditions on typical ranges of *OD*s we choose for averaging in our experiments.

In conclusion, the characterization measurements presented in this section confirm that our medium is a suitable platform to implement a nonlinear process such as SFWM that relies on EIT conditions. We obtained experimental values for all the relevant parameters of the SFWM scheme introduced in Chapter 2. When we compare our SFWM data to numerical calculations, the time-resolved measurements of the *OD* and the EIT conditions allow the use of experimental parameters for the whole range of accessible *OD*s.

Chapter 4

Experimental Implementation of a Photon-Pair Source based on SFWM

In this chapter, we present the implementation of SFWM in cold Rubidium confined within the core of the HCPBGF. We introduce the coupling scheme and temporal experimental sequence as well as the optical filter setup and the detection apparatus for our coincidence measurements. Subsequently, we give details on how we evaluate the experimental data in order to obtain the correlation functions required to proof the non-classical properties of the generated photons.

4.1 Coupling Scheme and Temporal Sequence

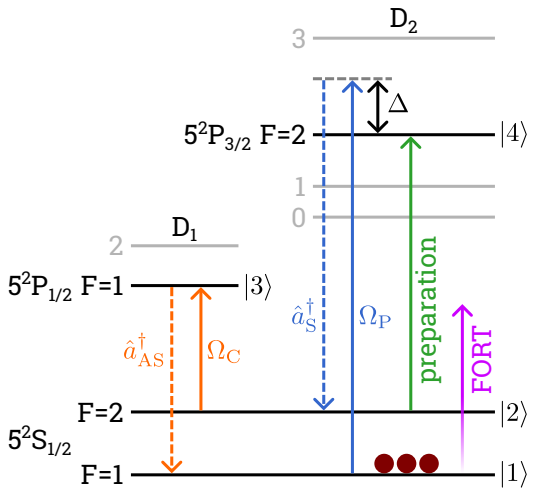

Figure 4.1: Coupling scheme for SFWM in ^{87}Rb. Solid (dotted) arrows depict applied (generated) fields. The excited states decay at rates $\Gamma_3 = \Gamma_{D1} = 2\pi \times 5.75\,\mathrm{MHz}$ and $\Gamma_4 = \Gamma_{D2} = 2\pi \times 6.07\,\mathrm{MHz}$. The ground state decoherence rate is $\gamma_{12} = 0.057\,\Gamma_{D1}$ (see Section 3.5). We apply the pump beam with a detuning $\Delta = +53\,\Gamma_{D2}$

The coupling scheme we implement in ^{87}Rb is shown in Figure 4.1. As we do not intentionally lift the degeneracy of the Zeeman states, we show only the hyperfine states. We generate the S photon on the D_2 line and the AS photon on the D_1 line. This choice allows the efficient attenuation of pump (control) noise in the AS (S) channel due to the 15 nm line splitting.

The temporal sequence of the SFWM experiment is depicted in Figure 4.2. After the atoms are captured in the MOT and subsequently loaded into the HCPBGF as introduced in detail in Section 3.4, we start at time $t_0^{\mathrm{cyc}} = 1060\,\mathrm{ms}$ to periodically switch off the FORT for periods of 2.4 µs before switching it on again for 1.6 µs to recapture the atoms and prevent collisions with the fiber wall. In the first four windows we prepare all the atoms in the groundstate $|1\rangle$ by optical pumping with the SFWM control beam and an additional orthogonally-polarized preparation beam on the D_2 line to address all magnetic sublevels of ground state $|2\rangle$. We do not prepare the atoms in a single Zeeman state.

After the preparation windows we begin applying our SFWM sequence shown in the lower panel of Figure 4.2. During each window, the atoms are first reprepared in the ground state $|1\rangle$ by optical pumping for 1 µs with the control and preparation beam. Subsequently, while keeping the control beam on, we simultaneously apply

the pump beam to drive the SFWM process for a duration of 1.2 µs. In the evaluation, we use a virtual temporal gate with duration $T_{\text{gate}} = 1.27\,\mu\text{s}$ to only include detections from the SPCMs while driving the SFWM process. The duty cycle within each window is thus about 0.3.

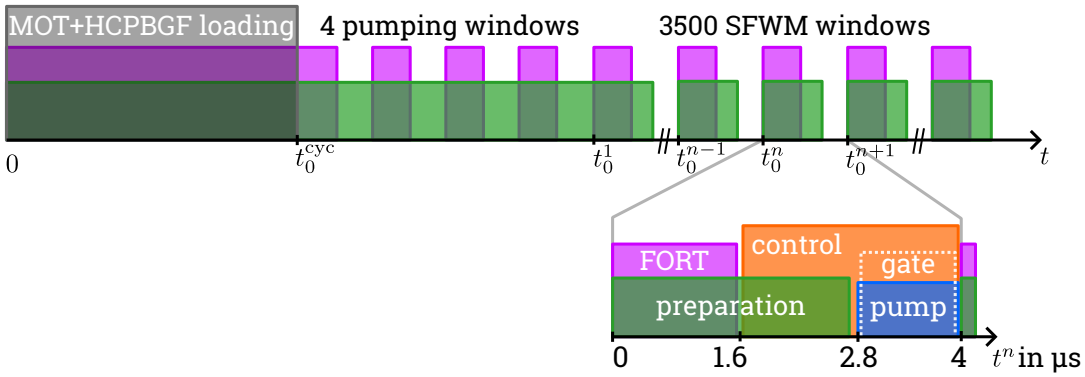

Figure 4.2: Simplified temporal sequence for SFWM on the MOT cycle scale (upper) and SFWM window scale (lower). The full cycle has a period of $T_{\text{cyc}} = 1.25\,\text{s}$ and consists of the HCPBGF loading followed by 4 pumping windows and 3500 measurement windows (numbered with label n) during which the FORT is switched off.

In Section 3.5 we characterized the reduction of the medium's *OD* versus the window count n. By post-selecting the range of experimental windows in the evaluation we can thus select the range of *OD*s included in a specific evaluation. Narrow ranges lead to sharply defined experimental conditions, while wider ranges increase the detection rates at the cost of averaging over changing conditions. The duty cycle, i. e., the ratio of SFWM data acquisition phases to the total duration of the experiment depends on the number of post-selected windows and is given by $\eta_{\text{duty}} = \frac{T_{\text{gate}}}{T_{\text{cyc}}}(n_{\text{stop}} - n_{\text{start}})$. The cycle and gate durations remain constant for all presented measurements and for typical ranges of, e. g., 500 included windows we thus obtain a duty cycle of $\eta_{\text{duty}} \approx 1/2000$. As detailed in Section 1.2, the generation rates (in contrast to the detection rates) given throughout this work are corrected for the respective duty cycle.

4.2 Single Photon Detection

Building on the general setup described in Chapter 3, we now introduce the more specific setup for experiments at the single photon level. To detect and characterize the generated photon pairs, we analyze temporal correlations of the photons within the S or AS channel as well as between the two channels. For that purpose, as shown in Figure 4.3, we implement HBT setups for both the S and AS photonic channels by splitting the respective signals with 50:50 fiber beamsplitters[1] before guiding them to single-photon counting modules[2] (SPCMs). We refer to the four channels as S1, S2, AS1, and AS2 while we use the labels S and AS for the sum of the events in both detectors of the respective channel.

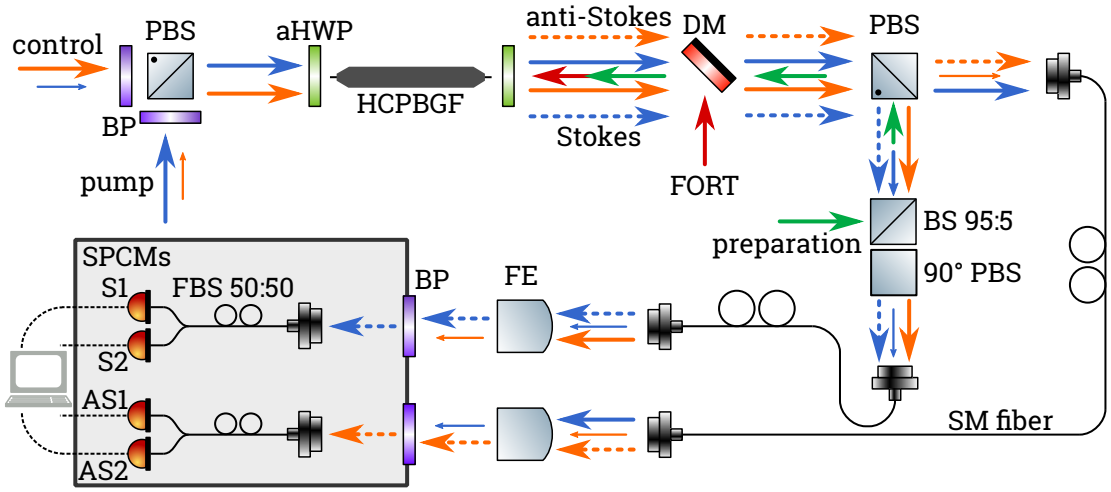

Figure 4.3: Simplified filter and detection setup. Solid (dotted) arrows depict applied (generated) light fields. Colors match those in the level scheme in Figure 4.1. Small arrows indicate optical noise before sufficient filtering. The shaded area is an opaque enclosure against stray light. (P/F)BS: (polarizing/fiber) beamsplitter, aHWP: achromatic half-wave-plate, L: lens, DM: dichroic mirror, FE: filter etalon, BP: optical bandpass filter. Solid lines represent optical single-mode (SM) fibers and dotted lines electronic signals.

Our SPCMs are fiber-coupled, non-number-resolving silicon avalanche photodiodes operated in Geiger-mode [10]. They emit TTL pulses with a duration of 10 ns when absorbing a photon and have a subsequent dead time of 32 ns until they can detect another photon. For count rates $\gtrsim 5\,\mathrm{Mcts\,s^{-1}}$ saturation of the detector can no longer be neglected and leads to an underestimation of the actual count rate. Within the linear regime, the intrinsic quantum efficiency of the SPCMs is specified as 63 % at the relevant wavelengths. When we include the transmission through all optical elements and filters (optics: 50 %, etalons: 30 %, fiber beamsplitter 90 %, SPCM fiber coupler: 95 %) after the HCPBGF, we obtain the total detection efficiency of both channels as $\eta_{\mathrm{det}} = 8\,\%$. Our detectors have measured dark count rates between $350\,\mathrm{cts\,s^{-1}}$ and $2500\,\mathrm{cts\,s^{-1}}$, depending on the detector.

We acquire the timings of all detected photons with FPGA-based time-tagging

[1] Thorlabs, *TW805R5F1*
[2] Excelitas, *SPCM-AQRH-13-FC*

electronics[3] (TT) for further analysis. The TT generates a list of timestamps based on the timing of the incoming TTL pulses from all four photon counters, as well as temporal markers that we include in the sequence to identify the HCPBGF-loading cycle as well as the measurement windows in the data. The combined timing jitter of the detection system is specified as $< 400\,\mathrm{ps}$ and limited by the SPCMs. As we will see in Chapter 5, the temporal dynamics of the generated photon pair are on a timescale of a few 10 ns (compare, e. g., the biphoton waveform in Figure 5.1). Hence, we neglect the timing jitter in our analysis. For maximal flexibility in the analysis, we do not apply any temporal gating during the data acquisition. This allows us to perform different measurements on the same data set, which would be impossible using analog signal processing.

4.2.1 Optical Filter Setup

A major concern in single photon experiments is optical noise that leads to false counting events. Optical noise not originating directly from the SFWM process is mainly stray light from the surrounding (e. g., originating from the laboratory lights, computer screens, status indicators) and light from the laser fields not directly involved in the SFWM process, i. e., the MOT and HCPBGF loading beams. We use fiber coupled detectors and the single-mode fibers to the detection serve as spatial filters and are aligned for maximum overlap with the guided mode of the HCPBGF. This spatial filter alone is not enough, though, to filter out the stray light to a level below the detectors dark counts. As both our generated photons have wavelengths in the near infrared, we can effectively block the optical noise in the visible spectrum with a combination of an opaque housing for our detection setup and the use of optical bandpass filters in front of the coupler into the single-mode detection fibers. The infrared beams of the MOT and HCPBGF loading are switched off with their respective AOMs or shutters during data acquisition. Together with the spatial filtering of the fiber-based detection, this provides sufficient attenuation of the stray light to well below the detectors intrinsic dark count levels.

The main challenge, however, is to filter out the colinear pump and control fields. Typically we work with powers of about 100 nW corresponding to a photon flux of about $4 \times 10^{11}\,\mathrm{s}^{-1}$. Depending on the specific experiment, our signals include a photon flux between 10 and $10\,000\,\mathrm{s}^{-1}$. Another benchmark for the suppression of optical noise are the detectors intrinsic dark counts. We require an attenuation of at least 80 dB to reach an optical noise level comparable with the SPCM dark counts. Both of the driving fields in the SFWM process are active during the detection of the generated photons and they both propagate colinear with the S and AS photons in the same single guided mode of the HCPBGF. Therefore, the use of spatial filtering is impossible for the SFWM driving fields.

Our filter setup is depicted in Figure 4.3. Measurements of the emission spectra of our ECDLs using an optical spectrum analyzer[4] showed non-negligible frequency components 15 nm separated from the central wavelength with a relative power of about −50 dB compared to the central wavelength. We show an example of this

[3] Swabian Instruments, *Timetagger 20*
[4] *Yokogawa*, AQ6373B

measurement in Figure 4.4. As a consequence, we implement a pre-filtering of the pump and control fields using narrow bandpass filters[5]. Subsequently, we combine the orthogonally linearly polarized pump and control fields in front of the HCPBGF using a polarizing beamsplitter (PBS). As the involved wavelengths (together with the FORT at 820 nm) span 40 nm we use achromatic half-wave plates to align the polarization axes of the linearly polarized laser fields to the optical axis of the HCPBGF at the input. This allows the highest degree of polarization at the output and thus optimizes the efficiency of polarization filtering. As confirmed by numerical simulations of the SFWM process including the Zeeman structure and laser field polarizations (see Appendix A), the generated S (AS) field is orthogonally polarized to the pump (control) field. Due to their orthogonal polarizations, the two generated fields can be separated by a PBS which simultaneously serves as the first filter stage. The optical noise originating from residual pump (control) light in the S (AS) channel separated by 6.8 GHz is attenuated by up to 40 dB. To achieve this attenuation in both channels, we add a second PBS in transmission in the S channel. After polarization filtering the photons are coupled into single-mode fibers which serve as spatial filters to isolate the HCPBGF's optical mode.

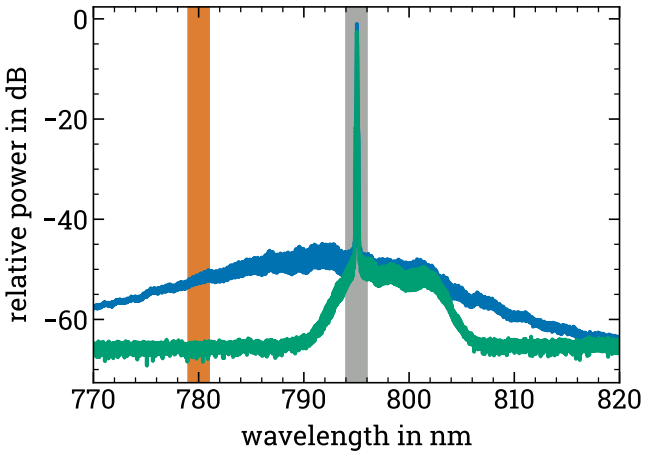

Figure 4.4: Power spectrum of the control laser (ECDL 4). The laser is stabilized to the D1 line (grey shaded area) and emits a broad background (blue solid line) due to amplified spontaneous emission within the gain profile of the laser diode. The relative power at the wavelength of the D2 line (orange shaded area) is about −50 dB. The green solid line corresponds to the power spectrum after filtering with an optical bandpass.

As a second filtering stage we use two home-built temperature-tuned monolithic etalons [114, 115]. They consist of commercial lenses with a dielectric high-reflectivity coating. Their free spectral range of 15.7 GHz is optimized for the attenuation of the optical noise in the S (AS) channel that originates from the pump (control) beam (separated by 6.8 GHz). We reach an attenuation of up to 45 dB and a fiber to fiber transmission of 30 %. Additionally, the etalons also attenuate the optical noise by the control (pump) beam (separated by 15 nm) ins the S (AS) channel, though not as efficient as the 6.8 GHz separated noise. Therefore, as a third stage, we employ narrowband optical filters (attenuation > 25 dB) to further attenuate the 15 nm separated optical noise as well as the broadband noise originating from stray light. The laser beams required within the HCPBGF in addition to the SFWM process, i. e., preparation beam and FORT, are aligned counter-propagating to the pump and control beams to protect the photon counting equipment and to minimize optical noise.

[5]Thorlabs, *FBH780-10* (pump) and *FBH800-10* (control), 10nm FWHM, $OD > 5$

Measurement of the Residual Optical Noise The remaining optical noise rate $\mathfrak{R}_j$ in channel j depends significantly on the applied pump power P. We model it as the sum

$$\mathfrak{R}_j = r_j^0 + r_j^0(P) + r_j(P), \tag{4.1}$$

where r_i^0 is the noise rate with no atoms loaded in the HCPBGF and no pump beam present, i. e., optical noise from stray light, residual control light and the dark counts of the SPCMs. The additional optical noise caused by the pump beam itself, but still measured without atoms present in the HCPBGF, is denoted by $r_j^0(P)$. The remaining contribution $r_j(P)$ accounts for the noise originating from the cold atoms and it is dominated by S photons generated in a Raman scattering process, i. e., without the corresponding AS photon, and residual optical pumping.

We measured the contributions without atoms to be $r_\mathrm{S}^0 = 2800\,\mathrm{s}^{-1}$, $r_\mathrm{AS}^0 = 1200\,\mathrm{s}^{-1}$, $r_\mathrm{S}^0(P) = 84\,\mathrm{s}^{-1}\,\mathrm{nW}^{-1}\cdot P$ and $r_\mathrm{AS}^0(P) = 7.6\,\mathrm{s}^{-1}\,\mathrm{nW}^{-1}\cdot P$. We cannot independently measure $r_j(P)$ without driving the SFWM process at the same time. Hence, we will neglect it in our analysis. The agreement of our model with the experimental data that will be presented in Section 5.4.1 supports this simplification. In that section, we will also give additional details of how we include the noise model in our theory model.

4.3 Time-Dependent Normalization in Correlation Measurements

A $g^{(2)}$ (auto- or cross-) correlation function as introduced in Section 1.2 compares measured coincidences between two channels to the number of coincidences expected statistically from the two individual count rates, i. e., the accidental coincidences. For the correct determination of the correlation, it is crucial to not only precisely measure the number of coincidences but also reliably identify the accidental coincidences that are required for the normalization. The determination of the normalization factor becomes non-trivial whenever the involved detection rates vary on a time scale similar to the coherence time of the generated photons.

We illustrate this in Figure 4.5. In panel (a), we first show the simple case of a cw experiment. Because the individual count rates R_i (orange and blue) are constant over all times t, we observe a fixed accidental rate of $R_{12}^\mathrm{acc}(\tau) = R_1 \cdot R_2$ for any delay τ between the detections in the two channels (green). The individual rates R_i can be directly measured. When we pulse the excitation (b) with a pulse duration T, the resulting histogram of the accidentals becomes triangular shaped. This can be understood as follows: For simplicity, we assume that the histogram has $2\cdot n+1$ discrete bins with width T/n. Because coincidences with a delay of $\tau = 0$ can happen during the full duration T of the pulse, there are events at n absolute times t each contributing with a probability $R_1 \cdot R_2 \cdot T/n$ to the central bin of the histogram. In contrast, there is only a single configuration of events contributing to the bin for $\tau = +T$, i. e., a detection in channel 1 exactly at the start and a detection in channel 2 exactly at the end of the pulse. In (c), we now consider a finite pulse train of these excitation pulses repeating with period P. We obtain multiple triangular peaks in the histogram, where the shape of

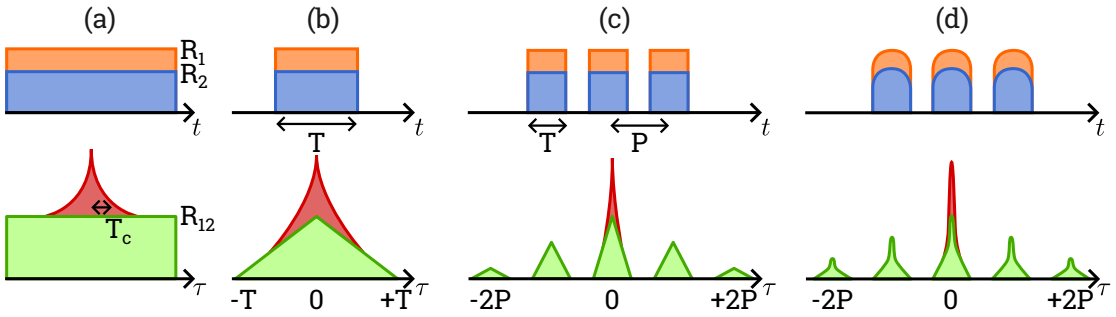

Figure 4.5: Sketch of time dependent count rates R_1 and R_2 of two individual channels (upper panels) and corresponding histogram R_{12} of accidental coincidences (green) and actual coincidences (red) within the systems coherence time T_c versus the time delay τ between the two events (lower panels). (a) cw excitation, (b) pulsed excitation with pulse duration T, (c) excitation by a finite pulse train with period P, and (d) with temporally modulated rates. All amplitudes are in arbitrary units, chosen for illustration, and not calculated to scale.

each individual peak can be explained as in (b). All peaks but the one centered around $\tau = 0$ correspond to coincidences between different excitation pulses. Thus, we observe them with a spacing of $\tau = P$ in the histogram. Due to the finite number of pulses in the pulse train, we again have to consider the number of pulse pairs that can contribute to each histogram peak and obtain a triangular envelope with a width dependent of the number of pulses. So far, we could still include all the effects of the pulsed experiment mathematically and calculate the (now time dependent) normalization factor from the observed individual rates for a known timing of the pulsed experiment. In panel (d), however, we add now a temporal variation of the individual rates $R_i(t)$ within the duration of the pulses. The resulting histogram of the accidental coincidences exhibits a distorted triangular shape and can in general not be described analytically.

Now, we additionally consider the non-accidental coincidences R_{12}^{act} that, because they origin from physical correlation in our system, can only be observed for a relative delay τ below some coherence time T_c. The dynamics of $R_{12}^{act}(\tau)$ is generally independent of the dynamics of the count rates $R_i(t)$. We draw an example in red in Figure 4.5. In the experiment, we can only access $R_{12}(\tau) = R_{12}^{act}(\tau) + R_{12}^{acc}(\tau)$. In the cw case (a) it is simple to distinguish between the accidental and non-accidental coincidences because $R_{12} \to R_{12}^{acc}$ for $\tau \gg T_c$. The effects of the pulsed but unmodulated cases (b) and (c) can be included mathematically from the observable count rates.

However, to identify the accidental coincidences for temporally modulated (and pulsed) case (d), i. e., the situation in our experiment, we have to use the fact that the measurement windows in our experiments represent physically unrelated repetitions of the experiment. This assumption is justified due to the repreparation by optical pumping between the individual windows. Therefore, only accidental coincidences can occur for delays $\tau > T$ as illustrated in Figure 4.5 (d) in the lower panel. The peaks in the histogram centered at $\tau = \pm P, \pm 2P, \ldots$ only include accidental coincidences and we can use them to extract $R_{12}^{acc}(\tau)$.

In Figure 4.6 we show an example of this procedure with actual experimental data. The individual rates shown in panel (a) are strongly time dependent. In

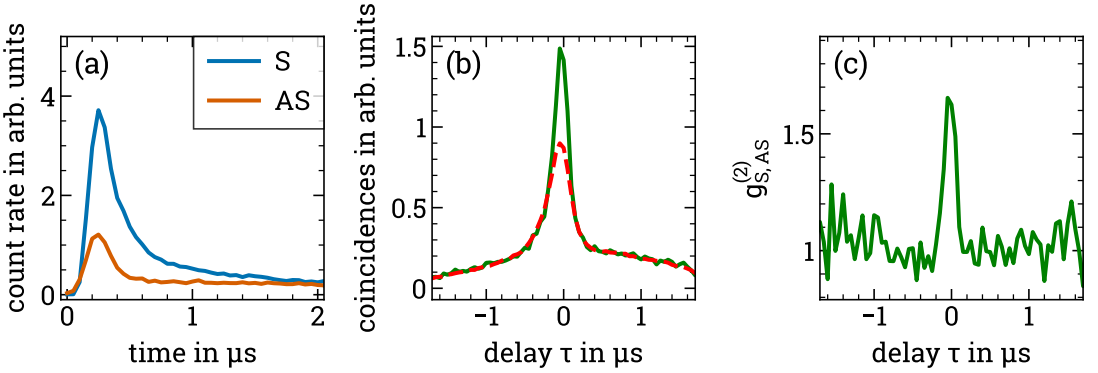

Figure 4.6: Example for the delay-dependent normalization. (a) Time dependent count rates $R_i(t)$. (b) Measured coincidences (green solid line) and delay-dependent accidental coincidences (dashed red line) extracted from averaging the correlations between 10 combinations of physically uncorrelated windows. (c) Resulting cross-correlation.

panel (b), we show the histogram of the coincidence counts (green solid line). The triangular shaped accidental background (compare Figure 4.5) is visible, but the fraction of the central peak originating from accidental coincidences cannot be estimated from the histogram alone. When we use the coincidences between uncorrelated windows to extract the delay-dependent accidentals, we indeed observe a modulation in the accidentals on the timescale given by the dynamics of the rates (red dashed line). In panel (c), we additionally show the resulting cross-correlation after (delay-dependent) normalization.

We note, that for clarity we choose here a data set with a particularly strong temporal variation in the individual rates. In general, constant photon rates over the duration of one measurement window are desired but can not always be fully achieved. However, our method allows a reliable determination of the correct normalization, independent of the temporal dynamics of the photon rates as well as the biphoton coherence time.

Chapter 5

Generation of Bright and Narrowband Photon Pairs

By implementing the experiment as described in the previous Chapter 4, we generate correlated S-AS photon pairs for a wide range of the experimentally controllable parameters *OD* and pump power. This allows for tuning the spectral brightness and cross-correlation of our photon-pair source. We published the main results presented in this chapter in [15].

5.1 Non-Classical and Narrowband Photon Pairs

First, we restrict ourselves to a single set of experimental parameters that provides highly non-classical pairs at a good signal-to-noise ratio at a *GSBP* of about $300\,\text{pairs}\,\text{s}^{-1}\,\text{MHz}^{-1}\,\text{nW}^{-1}$ (will be discussed in detail in Section 5.2) which is comparable to the largest *GSBP* reported in [19]. Thus, we choose it for a detailed analysis of the generated biphoton properties. In the subsequent sections, we will then investigate the dependence of these properties on the experimental parameters.

Figure 5.1(a) shows the measured cross-correlation $g^{(2)}_{\text{S,AS}}(\tau)$ of the photon pairs as a function of the time delay τ between S and subsequent AS detection events. Here, positive delays correspond to the S detection before the AS detection. We obtained the data by normalizing the coincidences to the delay-dependent background of accidental coincidences as described in detail in Section 4.3. The asymmetry with regard to the delay (we observe events only for positive delays) is expected because the AS photon is delayed by the slow light effect with regard to the S photon. When we evaluate the group delay defined in Equation (2.20), we find $\tau_g \approx 50\,\text{ns}$ in agreement with the observed delays in Figure 5.1. We include measurements in the range of $OD = 40$ to 80 in the evaluation to obtain good statistics within an effective (i. e., duty-cycle corrected) integration time of 3.5 s. This corresponds to a real-time measurement duration of 7200 s which is well within the technical limits given by the stability of our system. We apply a pump power of $P = 14\,\text{nW}$ and a control power of 17 nW corresponding to (resonant) Rabi frequencies of $\Omega_\text{P} = 3.1\,\Gamma_{\text{D1}}$ and $\Omega_\text{C} = 2.8\,\Gamma_{\text{D1}}$.

Clearly, the cross-correlation exceeds the classical limit of $g^{(2)}_{\text{S,AS}}(\tau) = 2$ (red dotted line) for a range of delays. We verified experimentally that the individual S and AS fields exhibit thermal statistics, i. e., $g^{(2)}_{\text{S,S}}(0) = g^{(2)}_{\text{AS,AS}}(0) \approx 2$. These measurements will be presented in the following Section 5.1.1. As introduced in Section 1.2, we quantify the violation of the Cauchy-Schwarz inequality (1.12) by calculating $\mathcal{R} = (g^{(2)}_{\text{S,AS}})^2/(g^{(2)}_{\text{S,S}}\, g^{(2)}_{\text{AS,AS}})$. For the data shown in Figure 5.1, the peak value is $\mathcal{R} = 97(24)$, which clearly violates the classical limit of $\mathcal{R} \leq 1$ by

4 standard deviations and demonstrates the non-classical nature of the photon pairs. The small damped oscillations visible in the waveform indicate that we work in the transition region between the damped Rabi oscillation and the group delay regimes, as introduced in Section 2.2 (compare especially Figure 2.3).

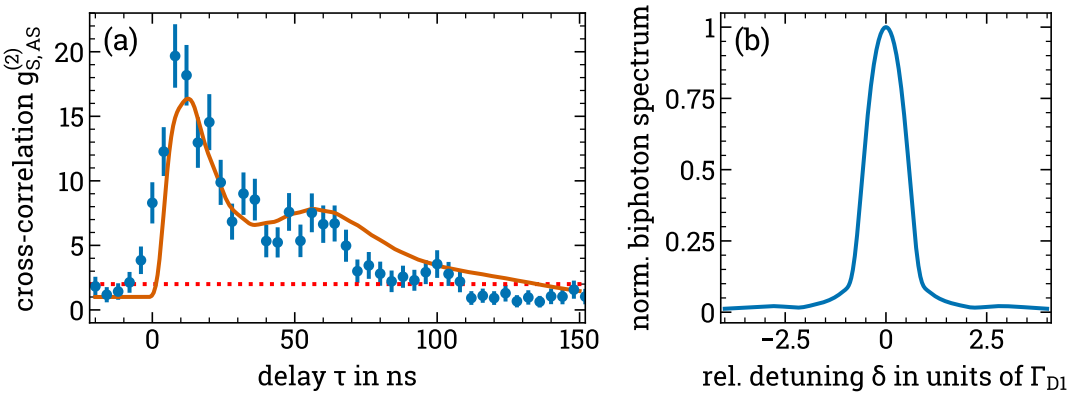

Figure 5.1: Biphoton waveform and spectrum. (a) Cross-correlation $g^{(2)}_{S,AS}$ versus the delay τ between AS and S detection events. The error bars depict the propagated Poissonian error of the photon counts. The red dotted line indicates the upper limit of the classical regime $g^{(2)}_{S,AS} = 2$. The bin size is 4 ns. The solid line shows the results of a numerical simulation of Equation (2.11) using parameters OD $= 15$, $\Omega_C = 2.8\,\Gamma_{D1}$ and $P = 14$ nW. A fixed factor of $g^{(2)}_{S,AS} = 1$ is added to the simulation to account for the uncorrelated background and we vertically scaled the simulation result to fit the data points. (b) Normalized biphoton spectrum extracted from the same simulation.

To obtain the bandwidth of the photon-pair source, we compare the experimental data shown in Figure 5.1(a) to a simulated waveform using the theoretical model introduced in Chapter 2. The relevant equations are introduced in Section 2.1. First, we evaluated Equation (2.11) starting with parameters determined from other measurements and subsequently optimized these parameters for the best agreement between simulation and experimental data. The features of the experimental data (blue circles) can be reproduced by the simulation (orange solid line). The discrepancy between the parameter sets of experiment and simulation might be explained by deviations of our experiment from the assumptions in the theory. There, homogeneous atomic density and pump/control intensities are assumed, which is clearly not the case inside the HCPBGF. Moreover, the simulation neglects the Zeeman substructure of the level scheme. We use the simulated waveform to extract the biphoton spectrum as shown in Figure 5.1(b). The spectral bandwidth (FWHM) is $2\pi \times 6.5$ MHz $\approx 1.1\,\Gamma_{D1}$ with a corresponding biphoton coherence time of $\tau_c = 24$ ns. Our results confirm the compatibility of our source with other Rubidium-based experiments and are in good agreement with similar experiments, e. g., [18, 60].

5.1.1 Thermal Photon Statistics of the Individual Fields

In addition to cross-correlations, we also measured the auto-correlations of the individual S and AS fields $g^{(2)}_{S,S}$ and $g^{(2)}_{AS,AS}$ to be able to calculate the violation of the Cauchy-Schwarz inequality (1.12) using only measured quantities.

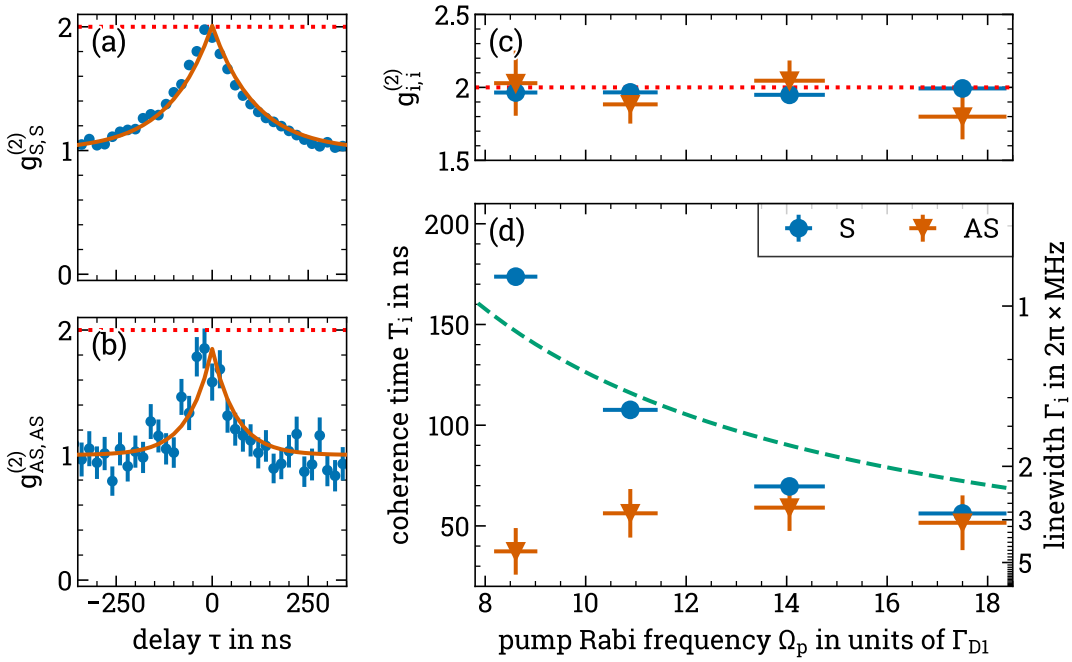

Figure 5.2: Measured auto-correlations of the individual S (a) and AS (b) photons versus the delay τ between events detected in the two detectors of a HBT setup. The solid orange lines show a fitted symmetrical exponential decay and and we shifted the data vertically to assure $g^{(2)}_{i,i} \to 1$ for $\tau \gg T_i$. The red dotted line corresponds to the thermal $g^{(2)}_{i,i} = 2$. The error bars depict the propagated Poissonian error of the photon counts. (c) Peak auto-correlation and (d) coherence time and spectral line width versus the resonant Pump Rabi frequency Ω_P. The dashed green line corresponds to a fit of Equation (5.1) to the S photon data. The control Rabi frequency is $\Omega_C = 2.8\,\Gamma_{D1}$ and the included range of ODs $d \approx 30 - 50$. The bin width is 20 ns. The error bars depict the uncertainties from the individual fits and a 5 % uncertainty in the pump Rabi frequencies.

As introduced in Section 1.1.1, we expect thermal photon statistics, i. e., an auto-correlation of $g^{(2)}_{AS,AS} = g^{(2)}_{S,S} = 2$ for the individual (unheralded) S and AS fields. In Figure 5.2(a)+(b) we show an example of the measured auto-correlation for both channels. The uncertainties for the AS channel are larger compared to the S channel because a successful AS detection depends on an accompanying S creation. Hence, the AS rate is limited by the S rate and further reduced by residual absorption (compare the EIT spectra in Figure 3.14). For a delay of $\tau = 0$ we observe the expected thermal statistics while for longer delays $\tau \gg 200$ ns the auto-correlation converges to 1 resembling only random coincidences. We repeated this measurement for different pump Rabi frequencies, i. e., photon generation rates, to check for variations in the individual fields statistics. As shown in Figure 5.2 (c), the measured peak auto-correlation agrees well with the expected thermal value over the whole parameter range.

Additionally, as shown in Figure 5.2(a)+(b), we fit the autocorrelation data with a symmetrical exponential decay of form $g^{(2)}_{i,i}(\tau) = g^{(2)}_{i,i} e^{-|\tau|/T_i}$ and obtain very good agreement with the experimental data. In Figure 5.2 (d) we plot the individual S and AS photons coherence time T_i extracted from the fits and the corresponding line width Γ_i versus the pump Rabi frequencies. The S photon is systematically narrower compared to the AS photon, especially for weak pump Rabi frequencies. For stronger pumping, the difference becomes negligible. While the AS line width remains approximately constant within the uncertainties, the S line width increases systematically with the pump Rabi frequency. As a reason for this increase of the line width we suspect power broadening due to the pump beam. To confirm, we fit the measured line widths with a function of form [116]

$$\Gamma_S(\Omega_P) = \Gamma_{s,0}\sqrt{1 + 2\left(\frac{\Omega_P}{\Gamma_{D1}}\right)^2}. \tag{5.1}$$

The dependence of the S line width on the pump Rabi frequency can be well described by power broadening and we obtain an unbroadened line width of the S photon of $\Gamma_{s,0} = 2\pi \times 89(9)\,\mathrm{kHz}$ from the fit. This value is in good agreement with the line width of the pump laser system. We currently cannot fully explain the observed individual AS line width of about $\Gamma_{AS} \approx 0.5\,\Gamma_{D1}$. We suspect a combination of two effects to be relevant here. The radially inhomogeneous AC Stark shift $\Omega_P(r)^2/(4\Delta)$ of ground state $|1\rangle$ induced by the Pump field leads to an inhomogeneous broadening of about 0.1 to $0.5\,\Gamma_{D2}$. However, we do not observe the expected systematic dependence on Ω_P^2. In addition, the AS photons are intrinsically frequency filtered due to the finite bandwidth of the EIT window, also of the the order of Γ_{D1} (compare Figure 3.14).

The observed coherence times of the individual fields are significantly shorter than, and thus not limited by, the ground state coherence time of about 480 ns measured by the EIT LS measurements we presented in Section 3.5. They are, however, longer than the observed biphoton coherence time τ_c of a few 10 ns (compare, e. g., the biphoton wave form in Figure 5.1). This indicates, that τ_c is not limited by the individual fields, but rather by the internal biphoton generation mechanisms described in Chapter 2.

We note here, that the parameter range in which we can perform the autocorrelation measurement with a sufficient signal-to-noise ratio is limited compared to the cross-correlation measurement. Because we split up the photons in the HBT setup in each channel, we require about twice the total number of detected photons to reach similar uncertainties as in a cross-correlation measurement. While the reduction in the number of detected events is uncritical for higher pump Rabi frequencies $\Omega_P \gtrsim 8\,\Gamma_{D2}$, it leads to prohibitively large uncertainties for lower pump Rabi frequencies. A further increase of the integration times to counteract this effect is, however, not possible due to practical limitations.

Nevertheless, as we did not observe a significant systematic deviation from thermal statistics over the whole accessible measurement range, we conclude that our measurement confirmed the expected thermal statistics for the individual S and AS fields.

5.2 Generated Spectral Brightness

We now turn to the analysis of the generated brightness and how the non-classical properties of the photon pairs presented in the previous section change when we vary the photon generation rates. As the simplest way to affect the generation rates, we vary the pump power P over three orders of magnitude.

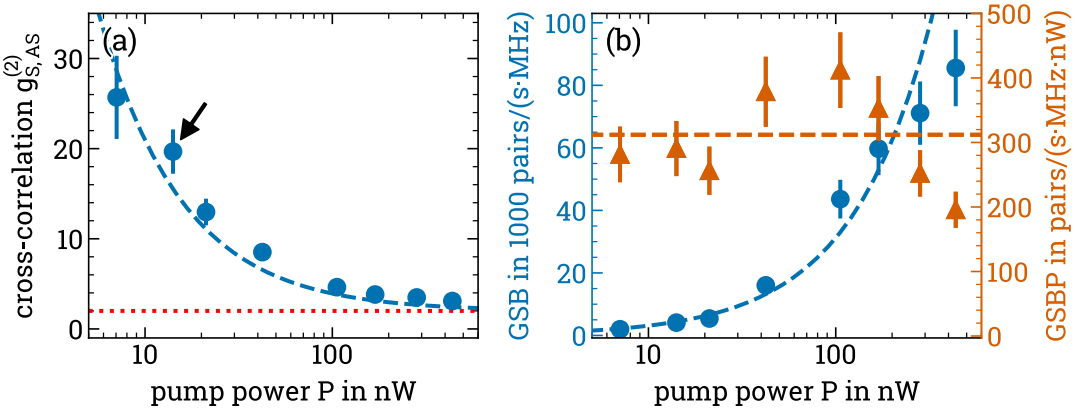

Figure 5.3: (a) Peak cross-correlation $g^{(2)}_{S,AS}$ (blue circles) versus pump power. The data point indicated by an arrow corresponds to the measurement in Figure 5.1. The dotted red line visualizes the classical boundary set by the Cauchy-Schwarz inequality. The dashed blue line corresponds to a numerical model including noise contributions. The parameters are the same as for the model shown in Figure 5.7. (b) GSB (left axis, blue circles) and GSBP (right axis, orange triangles). The dashed blue line corresponds to a linear fit to the GSB in the low pump power regime. The dashed orange line shows the same fit additionally normalized to the pump power. The error bars include the Poissonian error of the photon counts and a 10 % variation in the total detection efficiencies. The experimental parameters are OD $= 40 - 80$ and the control Rabi frequency $\Omega_C = 2.8\,\Gamma_{D1}$. The effective integration times range from 0.6 s to 3.5 s.

Figure 5.3(a) shows the measured peak cross-correlation $g^{(2)}_{S,AS}$ (blue circles) as a function of P. With increasing pump power the cross-correlation, i. e., the purity of the photon pairs, reduces following the expected $1/P$ dependence [117]. Nevertheless, we observe non-classical correlations over the full range of pump powers. We use the model described in Appendix B to calculate the peak cross-correlation that includes the measured unconditional as well as pump power-dependent optical noise in the S and AS channel (dashed line). The same parameter set determined in Figure 5.7 is also used for the simulation shown in Figure 5.3(a) without any additional fitting parameter. We use a linear dependence between the generated brightness and the pump power as shown in 5.3(b) (see next paragraph). Experiment and theory agree well over the whole range of pump powers.

In Figure 5.3(b) we show the corresponding *GSB* (blue circles, left hand side axis). We obtain this rate from the detected rate by correcting it for optical background, transmission losses, detection efficiencies, and the duty cycle of the experiment. The dashed blue line is a linear fit of type $GSB = GSBP \cdot P$. The fit confirms the expected linear dependence for pump powers up to 200 nW. For higher pump powers, the spectral generation rate increases slower. We suspect that

in this regime population redistribution due to optical pumping is no longer negligible. When we normalize the spectral generation rate with regard to the pump power, we obtain the *GSBP*. The experimental values (orange triangles, right hand side axis) range from $200\,\mathrm{s^{-1}\,MHz^{-1}\,nW^{-1}}$ to $410\,\mathrm{s^{-1}\,MHz^{-1}\,nW^{-1}}$. The orange dashed line represents the fitted value $GSBP = 312(24)\,\mathrm{pairs\,s^{-1}\,MHz^{-1}\,nW^{-1}} \approx 3\times10^{8}\,\mathrm{pairs\,s^{-1}\,MHz^{-1}\,mW^{-1}}$. In this intermediate parameter regime the *GSBP* of our source is comparable to the highest reported value $2\times10^{8}\,\mathrm{pairs\,s^{-1}\,MHz^{-1}\,mW^{-1}}$ using a waveguide coupled to an on-chip micro-ring cavity [19]. This very efficient conversion of pump power into narrowband photon pairs is enabled by the intrinsically large overlap between the cold atomic ensemble and the light fields in the HCPBGF as well as the optimal mode matching between the four involved fields due to all of them being guided in a single optical mode.

5.3 Demonstration of Heralding

We now turn to interpreting our photon-pair source as a heralded single photon source. One photon is detected and heralds the presence of a second photon. We are interested in the single-photon nature of this heralded signal photon. As introduced in Section 1.2, we can measure the degree of photon anti-bunching to quantify the single photon nature of the generated signal field.

Instead of using the S for heralding the AS detection events, as it is typically done, we use the AS to herald the S events for the following reason: As the Raman gain is not negligible compared to the SFWM gain for our current parameters, uncorrelated photons can be generated which act as additional noise. This process is mainly relevant for the S channel as the pump is coupled to the populated state $|1\rangle$, whereas the control is coupled to the unpopulated state $|2\rangle$. Using the AS detection events as heralding events for the creation of single photons in the S channel, we evade the influence of Raman noise on the heralding itself. As the AS photon is delayed by the slow-light effect of EIT (as introduced in Section 2.1) and thus exits the medium after the S photon, choosing the AS as heralding photon is somewhat counter-intuitive. If necessary, however, the temporal order of S and AS detection events could be easily changed by sending the S photons through a fiber optical delay line.

5.3.1 Conditional Auto-Correlation Measurements at Limited Detection Rates

The established method to observe anti-bunching is a measurement of the conditional auto-correlation function $g^{(2)}_{\mathrm{S,S|AS}}$ as it is defined in Equation (1.11). However, this definition includes a measurement of the triple coincidences between both the signal detectors and the heralding detector. While less critical for a cw experiment, the required integration times would be prohibitively long in our pulsed experiment, i. e., of the order of 24 h for a single data point.

To obtain data of sufficient quality within a reasonable acquisition time, we use the following method based on [118, 119] and illustrated with an example in Figure 5.4. We chose a heralding gate of 24 ns corresponding to the duration of

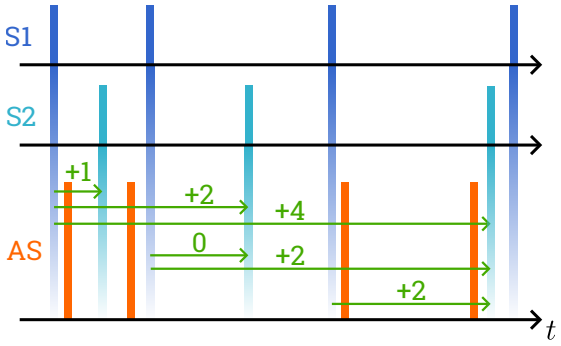

Figure 5.4: Scheme to observe anti-bunching at low detection rates. For every S1-S2 pair, we count the AS detections in between to construct the histogram. For simplicity, we omit here the S2-S1 pairs leading to negative histogram indices. More details in the main text.

the generated biphotons (compare Section 5.1). Any heralded S1(S2) detection event (dark blue marker), i. e., it is registered together with an AS event within the gate duration, is used as a start trigger. For any subsequent S2(S1) detection event (light blue marker), we record the number of additional AS events (orange marker) n between the two S events. The number of S1-S2(S2-S1) pairs with n AS events in between gives the amplitude of the n-th ($-n$-th) bin in the resulting histogram. Our example data would yield three counts in the +2-bin and one count in each of the 0,1, and 4-bin (depicted by green arrows). The zero bin of the constructed histogram corresponds to more than one S photon being heralded by the same AS photon. Such events contradict the single photon nature of the generated field. We determine the anti-bunching parameter $\alpha = g^{(2)}_{\mathrm{S,S|AS}}(0)$ as the amplitude of the zero bin normalized to the expected value that we get from a linear fit to the remaining bins [118].

In Figure 5.5(a) we plot the auto-correlation of the S photons conditioned on the detection of an AS photon, $g^{(2)}_{\mathrm{S,S|AS}}$. We observe anti-bunching of the heralded S photons with $g^{(2)}_{\mathrm{S,S|AS}}(0) = 0.16(2)$, clearly violating the classical bound of $g^{(2)}_{\mathrm{S,S|AS}}(0) \geq 1$ [37] and confirming a non-zero projection onto the single-photon Fock state for $g^{(2)}_{\mathrm{S,S|AS}}(0) \leq 0.5$ [14]. The conditional auto-correlation $g^{(2)}_{\mathrm{S,S|AS}}$ and the cross correlation $g^{(2)}_{\mathrm{S,AS}}$ are two different methods to quantify the non-classical nature of the generated photons. In 5.5(b) we compare both quantities, i. e., we evaluated the same set of data independently using both methods. We additionally plot the classical limits (dotted lines) for both methods. We generally observe agreement between both figures of merit. As expected, the anti-bunching effect becomes more pronounced for an increased cross correlation, i. e., a stronger violation of the Cauchy-Schwarz inequality. Additionally, we plot the expected dependence

$$g^{(2)}_{\mathrm{S,S|AS}} = \frac{4}{g^{(2)}_{\mathrm{S,AS}}} - \frac{2}{\left(g^{(2)}_{\mathrm{S,AS}}\right)^2} \tag{5.2}$$

for a two-mode squeezed state [18, 117] and find a good agreement with the experimental data.

Our results show that both the non-classical cross correlation as well as the heralded auto-correlation confirm the non-classical character of the generated photon pairs. Our source can be interpreted as a heralded source of single photons.

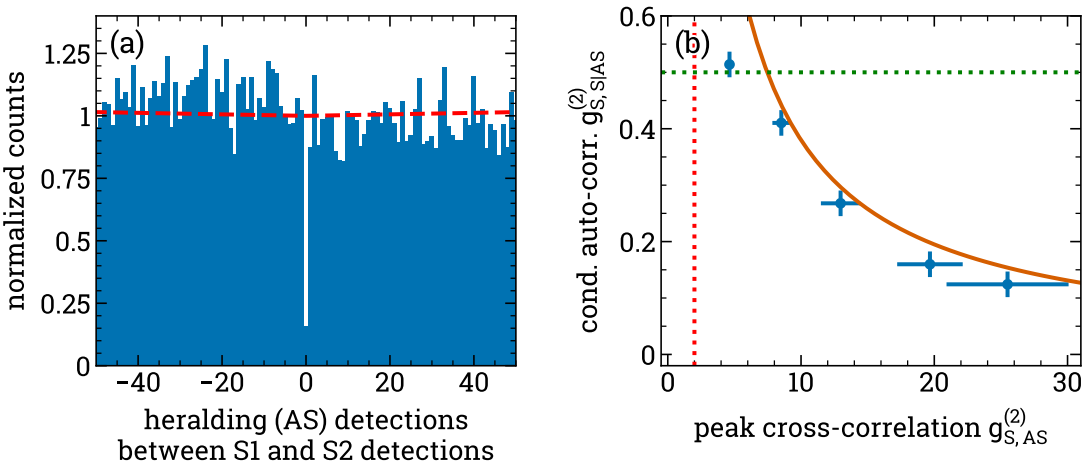

Figure 5.5: (a) Heralded auto-correlation $g^{(2)}_{S,S|AS}$ of the S photon conditioned on the detection of an AS photon. Data set is the same as in Figure 5.1. (b) Heralded auto-correlation $g^{(2)}_{S,S|AS}(\tau = 0)$ versus peak cross-correlation $g^{(2)}_{S,AS}$. The dotted red line is the classical limit of $g^{(2)}_{S,AS} < 2$ and the dotted green line marks the single photon regime $g^{(2)}_{S,S|AS}(0) \leq 0.5$. The solid orange line shows the expected dependence defined in Equation (5.2) without any additional scaling. Data set and parameters are the same as in Figure 5.3.

5.3.2 Heralding Efficiency

We calculate the heralding efficiency $\eta_H = R_{S,AS}/R_{AS}$ as the ratio of the pair generation rate $R_{S,AS}$ and the heralding rate R_{AS} both corrected for transmission losses. Figure 5.6 shows the measured η_H for a range of pump powers P. The efficiency increases with P for $P < 100\,\mathrm{nW}$ (corresponding to $\Omega_P \approx 8.5\,\Gamma_{D1}$) before it saturates for larger powers. We find a steady state value of $\eta_H = 50(2)\,\%$ by averaging the last four data points. The optimal mode matching in the HCPBGF facilitates such efficient heralding. In comparison, in a free-space SFWM experiment implemented in Rubidium vapor [63], a value of $\eta_H = 3.1\,\%$ is reported. In cold Rubidium, however, up to 92 % were observed [120]. We exceed the values reported for another waveguide coupled atomic ensemble source based on a nanofiber [18] or for cavity-enhanced down conversion [121] by about a factor of two. A likely explanation are lower

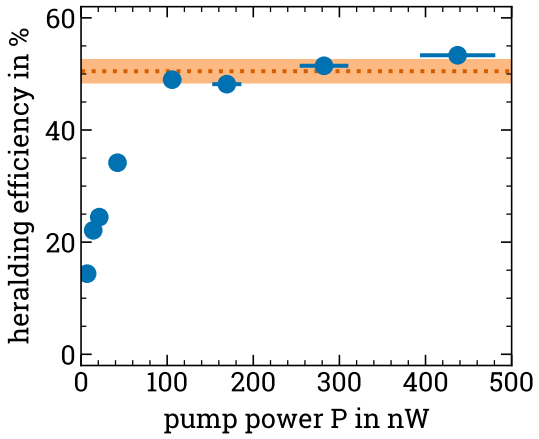

Figure 5.6: Heralding efficiency η_H versus pump power P. The efficiency saturates at $50(2)\,\%$ for $P \gtrsim 100\,\mathrm{nW}$, visualized by the dotted orange line. The experimental data set and parameters are the same as in Figure 5.3.

optical noise contributions by the pump fields in our experiment as we require pump powers of a few 10 nW compared to the mW regime reported in [18, 121]. In both of these experiments, the authors also report a reduction of the heralding efficiency in the weak excitation regime, similar to the behavior we observe. We account this effect to the dark counts in the heralding (AS) channel that create false heraldings and thus reduce η_H. We estimated that for the lowest pump power of 7 nW at least one third of the detected heralds are dark counts. The relative influence reduces with increased photon generation rates until it becomes negligible and η_H converges.

It is possible to formulate a criterion in terms of η_H for the compatibility of a heralded photon source with a given quantum memory [121, 122]. When we characterize a quantum memory by the minimum number μ_I of input photons required for a signal-to-noise ratio of 1 in the retrieved signal, we require a single photon source with a heralding efficiency of $\eta_H > \mu_I$ in order to observe quantum storage and retrieval. In terms of this criterion, our source is compatible with current state-of-the-art quantum memories, e. g., implemented in atomic vapor [123], cold atoms [124], or solid state media [125].

5.4 Highest Generated Spectral Brightness per Pump Power

So far, we only varied the pump power to change the photon generation rates and kept the properties of our medium fixed. We now extend our analysis to a variation of the *OD*. Note, that in this section we again use the nomenclature of photon pairs rather than that of heralded single photons.

In Figure 5.7 we show the dependence of the peak cross-correlation $g^{(2)}_{\mathrm{S,AS}}$ and the *GSBP* on the pump power as well as on the *OD*. As explained in Section 3.5 we can acquire data for *OD*s between the maximum value of about 150 and 0 within the same MOT loading cycle. We then average over data slices of 100 measurement windows each.

Our system allows for an easy tuning of the *OD* over two orders of magnitude. This, combined with a tuning of the pump power results in a tunability of the *GSBP* of our photon-pair source by more than three orders of magnitude. The regimes of high generation rate but low-quality photon pairs (upper right corner at high *OD* and high pump power) and low generation rate with high-quality photon pairs (lower left corner at low *OD* and low pump power) can be clearly identified in Figure 5.7(a) and (b). The parameter range of the data presented in Figures 5.1 and 5.3 lies in between these two regimes and is marked by the blue and green rectangles, respectively. Note, that we averaged over 500 instead of 100 measurement windows in those evaluations to achieve improved statistics. Generally, the highest values for $g^{(2)}_{\mathrm{S,AS}}$ are observed in the low *OD* and low pump power regime. When we restrict ourselves to parameters with $g^{(2)}_{\mathrm{S,AS}} \geq 3$, the highest observed *GSBP* is $2 \times 10^9\,\mathrm{pairs\,s^{-1}\,MHz^{-1}\,mW^{-1}}$. We obtain this value at a pump power of 40 nW and the biphotons have a bandwidth of $2\pi \times 6.5$ MHz. The highest reported value so far [19] was $2 \times 10^8\,\mathrm{pairs\,s^{-1}\,MHz^{-1}\,mW^{-1}}$ with

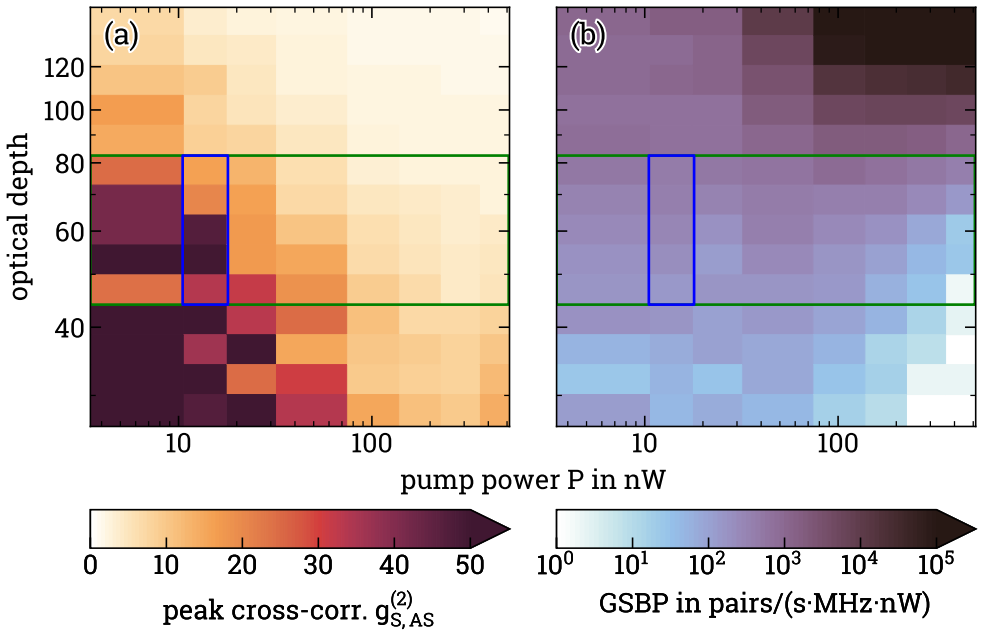

Figure 5.7: (a) Peak cross-correlation and (b) GSBP versus pump power and OD. The control Rabi frequency for OD $\gtrsim 55$ is $2.8\,\Gamma_{D1}$, for smaller ODs it is continuously reduced to maintain a fixed width of the EIT transmission spectrum as introduced in Section 3.5. The blue (green) box marks the data used in Figure 5.1 (Figure 5.3). The open-end color scales visualize the attainable values due to the limited measurement time.

a bandwidth of about $2\pi\times125$ MHz achieved with 50 µW of pump power in an on-chip micro-ring resonator. Hence, to the best of our knowledge, our results are a 10-fold increase over the previous record at 100-fold reduced pump power and 10-fold lower bandwidth. We note, however, that the achieved cross-correlations in [19] are in the range of 300 to 5000 and hence exceed our values by up to two orders of magnitude. We observe values of up to $g^{(2)}_{S,AS}= 117$ but note, that for values $g^{(2)}_{S,AS}\gtrsim 50$, the relative uncertainties become larger than 30 %, due to the low number of counts during the finite measurement duration. We achieve similar magnitudes for the cross-correlations as reported for other Rubidium-based experiments [52, 55, 63, 126].

This measurement demonstrates the versatile nature of our photon-pair source. Depending on the application requirements with regard to non-classicality and brightness, the parameter regime can be easily adjusted. Additionally, one has to choose the included range of *OD*s and can make a trade-off between homogeneous experimental conditions and increased detected brightness, i. e., the number of detected photons per real time.

5.4.1 Limit of the Spectral Brightness

Finally, we investigate what limits the achievable brightness in our system. To this end, we observe now the *GSB*, i. e., we do not normalize the brightness with regard to the pump power.

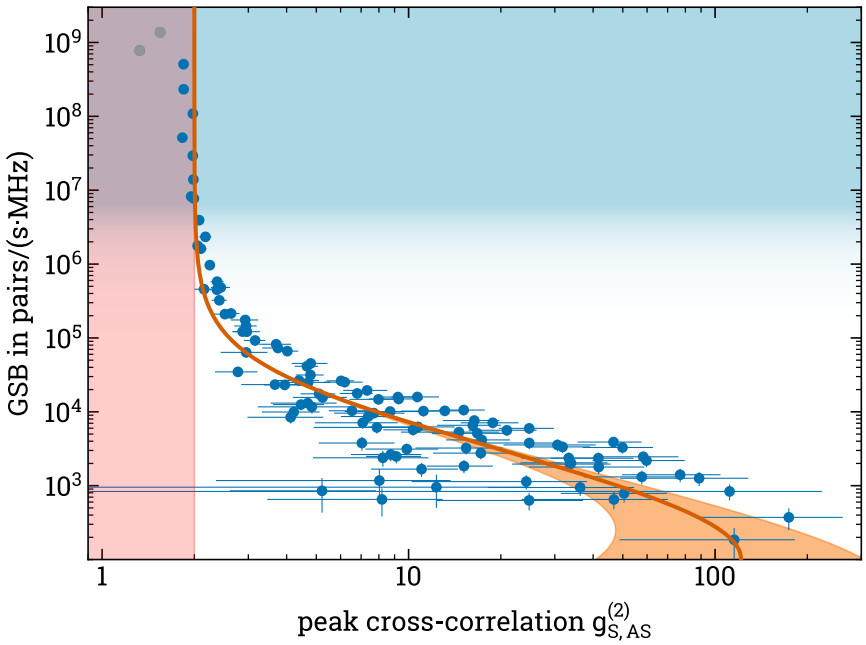

Figure 5.8: GSB versus cross-correlation $g^{(2)}_{S,AS}$. The data is the same as in Figure 5.7. The classical regime of $g^{(2)}_{S,AS} \leq 2$ is marked by the red shaded area. The blue gradient visualizes the increasing temporal overlap between subsequent photon pairs. The error bars of the data points correspond to the propagated statistical error of the photon counts. For the grey data points the saturation of the SPCMs due to high detection rates can no longer be neglected. The solid orange line is a single-mode model described by Equation (5.3). The shaded orange area visualizes the influence of pump-dependent noise as explained in the main text.

In Figure 5.8 we plot the *GSB* versus the peak cross-correlation $g^{(2)}_{S,AS}$. We include data points for all available *OD*s as well as the full range of pump powers in this plot. Note that the grey data points correspond to a count rate where the saturation of the SPCMs cannot be neglected anymore. As we can see, for higher spectral brightnesses the peak cross-correlation decreases and reaches a lower limit near two. We fitted the data using the model described in Appendix B that is based on a single-mode description and thermal statistics. We start from Equation (B.3) and write the pair number as $n = \alpha \cdot GSB$ with a scaling factor α. The solid orange line in Figure 5.8 thus corresponds to a fitted function of the form

$$g^{(2)}_{S,AS} = \left(2 + \frac{1}{\alpha GSB} + \frac{\mathcal{N}_S \mathcal{N}_{AS}}{T_S T_{AS} (\alpha GSB)^2}\right) \Bigg/ \left[\left(1 + \frac{\mathcal{N}_S}{T_S \alpha GSB}\right)\left(1 + \frac{\mathcal{N}_{AS}}{T_{AS} \alpha GSB}\right)\right] \quad (5.3)$$

with noise contributions $\mathcal{N}_j$ and detection efficiencies T_j, where we used measured values as described in Appendix B and Section 4.2.1. The scaling factor

is the only free parameter for our fit and was determined to be $\alpha = 103$. As the dataset includes points obtained with different pump powers, the pump-dependent noise contributions also vary. This is visualized by the orange-shaded area. Non-classical correlations with $g^{(2)}_{\mathrm{S,AS}} > 3$ are maintained up to a *GSB* of around $2 \times 10^5\,\mathrm{pairs\,s^{-1}\,MHz^{-1}}$.

Beyond this brightness, successive photon pairs start to overlap in time. For a given *GB*, the average temporal separation between subsequent pairs is $P = 1/GB$. Further, we write the biphoton bandwidth as $\Delta\omega = 1/(2\pi T)$ with the temporal duration T. By definition we then have $GSB = GB/\Delta\omega = 2\pi T/P$. When we accept a 25 % probability for another photon pair to be generated during the previous one, as it is defined in [58], we obtain a maximum $GSB = \pi/2 \times 10^6\,\mathrm{pairs\,s^{-1}\,MHz^{-1}}$. This transition from temporally separated to overlapping photon pairs is visualized by the blue color gradient in Figure 5.7. It matches very well with the observed convergence of $g^{(2)}_{\mathrm{S,AS}} \to 2$ in the experimental data. The value of 2 indicates that thermal statistics apply while the S and AS fields are still correlated and can each be described by a single mode. In contrast, if the data would be dominated by uncorrelated noise in the high *GSB* regime, we would expect a limit of $g^{(2)}_{\mathrm{S,AS}} \to 1$.

Our data clearly demonstrates that our photon-pair source can be operated near the ultimate limit of generated spectral brightness with a high tunability of the *GSB* as well as cross-correlation $g^{(2)}_{\mathrm{S,AS}}$, narrow bandwidth, and at low pump powers.

5.4.2 Enhancement of Raman Scattering Rate

To further understand the regime of high *GSB*, we calculate the expected effective Raman scattering rate [100]

$$\Gamma_R = \Gamma_{D2} R_B \left\langle \frac{\Omega_P^2(r)}{4\Delta^2 + 2\Omega_P^2(r) + \Gamma_{D2}^2} \right\rangle_r , \tag{5.4}$$

where R_B is the branching ratio into the target state and we take the radial average over the pump Rabi frequency weighted with the atomic density distribution (compare Figure 3.8). One would expect that the rate of generated S photons R_S is proportional to Γ_R.

In Figure 5.9(a) we plot the ratio R_S/Γ_R for our SFWM data. We observe a significant deviation from the expected behavior. For any value of Γ_R, we observe ratios $R_S/\Gamma_R \gg 1$ that increase for larger *OD*s. This becomes even more evident in the one-dimensional cuts shown in Figure 5.9(b).

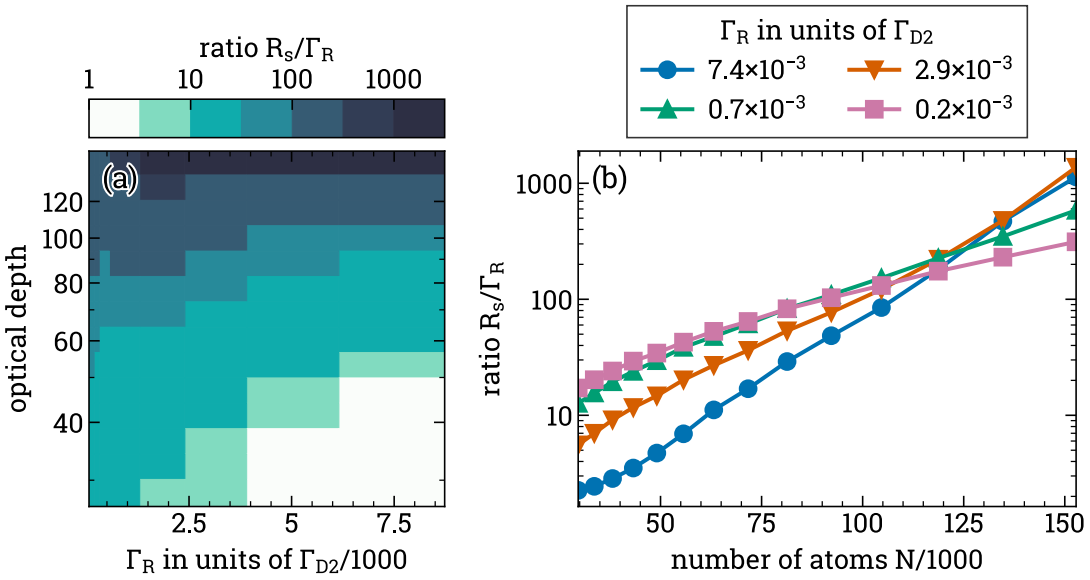

Figure 5.9: Enhancement of Raman Scattering Rate. (a) Ratio of S generation rate R_S and the expected effective Raman scattering rate Γ_R as defined in Equation (5.4) versus Γ_R and OD. (b) Vertical cuts for fixed values of Γ_R. The data is the same as in Figures 5.7 and 5.8. The experimental parameters are $R_B = 1/2$ and $\Delta = +53\,\Gamma_{D2}$.

These results indicate that we work in a regime where collective scattering such as superfluorescence [23] is dominant. Based on the measurements presented in Figure 5.9, we investigated the observed enhancement of the Raman scattering in the HCPBGF further in a separate experiment. We present those measurements, together with an introduction to superfluorescence in the following Chapter 6.

5.5 Proposed Technical Improvements

We conclude this chapter by addressing the current technical limitations in our experiment and propose concepts to reduce or even overcome these in the future.

Currently, the duty cycle of about 1 : 2000 is the most critical limitation towards interfacing our photon source with other experiments. As a simple approach, one might limit the loading time of the MOT to only prepare the amount of atoms necessary for the actually required *OD* range within the HCPBGF. In addition, the next loading cycle could then begin directly when the *OD* falls below a threshold value. From the known temporal dynamics of the number of atoms in the MOT [87] and our characterization measurements of the *OD* presented in Section 3.5, we estimate a possible improvement by a factor of 2 in the duty cycle for the data presented in Figure 2.11 with such an optimized sequence. As a more ambitious approach, intra-fiber magic-wavelength trapping [127, 128] could allow the continuous generation of photon pairs without the need to periodically modulate the guiding potential. This would also remove the main source for the loss of atoms over time, thus prolonging the measurement time per MOT loading cycle. For this technique, we estimate a possible enhancement of the duty cycle by two orders of magnitude by assuming that the atoms could be probed during a free fall through the whole fiber length due to gravity. Ideally, one could omit the periodic cycle of capturing a new MOT and subsequently load the atoms into HCPBGF completely. By periodically accelerating the atoms upwards to counter the effect of gravity, similar to observations in [72], one might be able to provide almost a steady state atomic ensemble within the fiber. An alternative approach could be to replace the loading cycle with continuous loading scheme where a stream of atoms is transferred into the HCPBGF from a constantly maintained MOT. Combined with magic-wavelength trapping, these later concepts might allow a quasi-cw operation of our source.

During this work, we coupled the generated photons from the HCPBGF to free space for subsequent separation and filtering before coupling them back into standard step-index fibers towards the detectors. As the generation of biphotons only requires atoms loaded *into* instead of *through* the fiber (note that in our case only the first 6 cm of the 14 cm long fiber are filled), the output side of the HCPBGF could be spliced directly to a (polarization-maintaining) fiber [71], thereby enabling direct connection to a other fiber based devices. In [129], a transmission 93 % was reported for an UHV compatible interface between a HCPBGF and a solid-core fiber.

Finally, by implementing intra-fiber laser cooling [130] the ensemble temperature could be reduced thereby prolonging the coherence time. In combination with an optimized pumping scheme to minimize inhomogeneous line broadening due to the AC Stark shift we could reduce the biphotons bandwidth further and significantly below the natural linewidth of our medium.

Chapter 6

Superfluorescent Emission into a Hollow-Core Fiber

In this chapter we present an additional experiment investigating superfluorescence (SF) within the HCPBGF. These measurements were motivated by the enhanced Raman scattering rate into the Stokes field that we observed in our SFWM experiments and presented in Section 5.4.2. A publication on the results presented in this chapter is currently in preparation.

SF is a form of superradiant[1] scattering [20, 22, 131] that is typically investigated in a two-level system where an initially completely inverted system decays cooperatively without an initial coherence. The dynamics of this cooperative decay become much faster than observed for individual emitters. As discussed in [27], there is a close analogy between SF [132] in a two-level system and stimulated Raman scattering (SRS) in a three level system. SRS can buildup from spontaneous Raman scattering [27] in a three-level system, where a detuned pump beam spontaneously scatters Raman photons. If the Raman gain is sufficiently high, these photons are then amplified as they propagate through the medium. In an effective two-level system the detuned pump field determines the (tunable) decay rate Γ_R of the "excited" state, which in this case happens to be a meta-stable ground state. In such a system, we avoid any temporal limitations given by the optical decay rate. Due to the SF decay, interesting temporal dynamics occur, manifested by strongly fluctuating radiation bursts with an average intensity scaling as $I \propto N^2$ with the number of emitters. These dynamics can be much faster than expected from the usual non-collective decay. We quantify the enhanced temporal dynamics of the system as the ratio

$$\Gamma_N/\Gamma_R = \mu N \tag{6.1}$$

between the observed scattering rate Γ_N that is enhanced by the collective decay and the expected scattering rate for individual emitters Γ_R. The ratio depends on the number N of emitters and a geometric factor μ that describes the fraction of scattered light that couples to the remaining ensemble. In free-space experiments with an elongated ensemble it is given by [22] $\mu = 3\lambda^2/(8\pi^2 w^2)$ with the wavelength of the emitted radiation λ and the ensemble width w. For a typical MOT with $w \approx 1\,\mathrm{mm}$ we get $\mu \approx 2 \times 10^{-8}$ and thus would require a comparably large minimum atom numbers $N \gg 1 \times 10^7$ to observe a significantly enhanced scattering rate. In the HCPBGF, however, the geometric factor is solely determined by the solid angle that can guide radiation through the waveguide and can be calculated as [133] $\mu = NA^2/4 \approx 2 \times 10^{-3}$ with our fibers $NA \approx 0.09$. These

[1] We note here, that the naming conventions for these collective or cooperative effects vary significantly between different fields and publications. In [23], the authors try to resolve some of these conflicts.

conditions within the HCPBGF allow us to observe SF effects already with a few thousand atoms.

6.1 Experimental Methods for the Observation of SF

Our experimental setup was already introduced in Chapter 3 and is shown in Figure 3.9. We use the APD as our detector and do not apply a control field for all experiments presented in this chapter. Figure 6.1(a) shows our coupling scheme. We apply a pump beam with a Rabi frequency Ω_P on the D1 line with a red detuning of Δ from the $|1\rangle \leftrightarrow |3\rangle$ transition. The pump beam generates the Stokes field via Raman scattering at a rate Γ_R. In Figure 6.1(b), we make the connection to the typical level schemes investigated in SF experiments. We interpret the populated ground state $|1\rangle$ as the "excited" state $|b\rangle$ of an inverted two-level system together with the ground state $|a\rangle = |2\rangle$. In contrast to most experiments, both our levels are meta-stable ground states and we can externally control the decay rate Γ_R. The enhanced decay rate observed in SF experiments, thus correspond to an enhancement of Γ_R in the collective medium over the scattering rate one would expect for individual emitters.

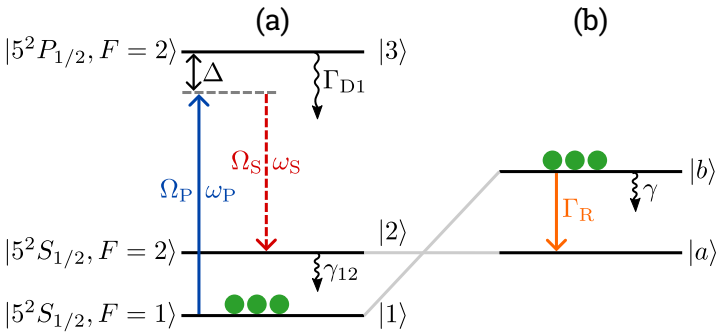

Figure 6.1: (a) Coupling scheme to observe SF implemented on the D1 line of ^{87}Rb. (b) Effective inverted two-level system with the Raman scattering rate Γ_R as a tunable decay rate and a decoherence rate $\gamma > \gamma_{12}$ that is increased by an inhomogeneous Stark shift due to the pump field.

We analyze the scattering process by detecting the generated Stokes field on the transition $|2\rangle \leftrightarrow |3\rangle$. Because it exhibits a linear polarization (mainly) orthogonal to the pump radiation, the pump field can be sufficiently attenuated with a PBS and we require no additional filtering. As the number of atoms in the HCPBGF reduces over time, we can systematically vary the number of atoms N in the ensemble by performing the experiment at different times after the HCPBGF loading process. We implement the variable detuning with an AOM in double-pass configuration.

Figure 6.2 shows an example of a single shot measurement. We observe a sharp signal burst, delayed by a few 100 ns from the switch on time of the pump pulse. For later times, we observe multiple oscillations in the signal. This feature is often referred to as ringing and it is a known feature of SF emission [134]. The ringing is caused by reabsorption and reemission of the generated field in different spatial positions within the medium [133]. Additionally, the generated radiation fluctuates heavily in peak power, delay, and shape from shot to shot. This is another sign of SF [21]. The strong fluctuations arise from vacuum fluctuations, which initialize the process. Due to the strong fluctuations, significant information

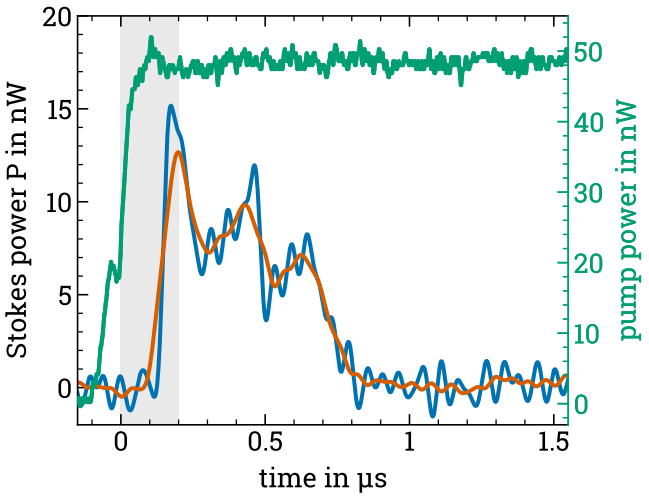

Figure 6.2: Exemplary single shot measurement of the SF signal. We apply a low pass filter to the raw data (blue line) to reliably extract the pulse area, peak amplitude and initial delay automatically from the filtered signal (orange line) for further analysis. The extracted delay for the first peak relative to the start of the pulse (green line, rhs axis) is $t_d = 199\,\mathrm{ns}$ as visualized by the gray shaded area. The plotted power is compensated for all transmission losses from the HCPBGF to the APD.

would be lost in any averaging process. Thus, we implemented an algorithm to extract the first peaks temporal delay t_d (with regard to the switch on time of the pump pulse), the peak power P_{max} of the signal, and the pulse energy E (integrated power) from the single shot data. For every set of experimental parameters, we obtain 100 single shots and then evaluate the mean and standard deviation of t_{d}, P_{max} and E for subsequent analysis. Subsequently, we extract the collective SF scattering rate Γ_{N} from the experimentally observed mean delay $\langle t_d \rangle$ of the first SF pulse as [135]

$$\Gamma_{\mathrm{N}} = \frac{\left(\ln\sqrt{2\pi N}\right)^2}{4\langle t_d \rangle}. \tag{6.2}$$

6.2 Dependence of SF on the Number of Emitters

We perform systematic measurements by observing the SF signal for detunings in the range of $\Delta = -2\,\Gamma_{\mathrm{D1}}$ to $-26.4\,\Gamma_{\mathrm{D1}}$ and vary the number of atoms from $N = 50 \times 10^3$ to 230×10^3. We then compare Γ_{N} (obtained from the measured delays t_d) with the theoretically expected scattering rate for a medium of individual emitters [100]

$$\Gamma_R = R_{\mathrm{B}}\Gamma_{D_1}\frac{\langle\Omega_{\mathrm{p}}^2\rangle_r}{\Gamma_{D_1}^2 + 4(\Delta + \langle S\rangle_r)^2 + 2\langle\Omega_{\mathrm{p}}^2\rangle_r}. \tag{6.3}$$

Here, $R_{\mathrm{B}} = 1/2$ is the branching ratio into the target state and we include the geometry of our medium by using radial averages (denoted $\langle ... \rangle_r$) weighted with the atomic density distribution (compare Figure 3.8) for Ω_{p} and the induced AC Stark shift of the optical transition $S = \Omega_{\mathrm{p}}^2/(2\Delta)$. Figure 6.3(a) shows the ratio $\Gamma_{\mathrm{N}}/\Gamma_{\mathrm{R}}$ of this experimentally determined scattering rate and the expected scattering rate for individual emitters plotted versus the absolute number of atoms within our HCPBGF. The solid line shows the expected linear dependence defined in Equation (6.1). Obviously, our data cannot be directly described by this theory and we do not observe a systematic dependence of the measured ratio $\Gamma_{\mathrm{N}}/\Gamma_{\mathrm{R}}$ on the number of atoms. However, the ratio becomes larger for increased detuning.

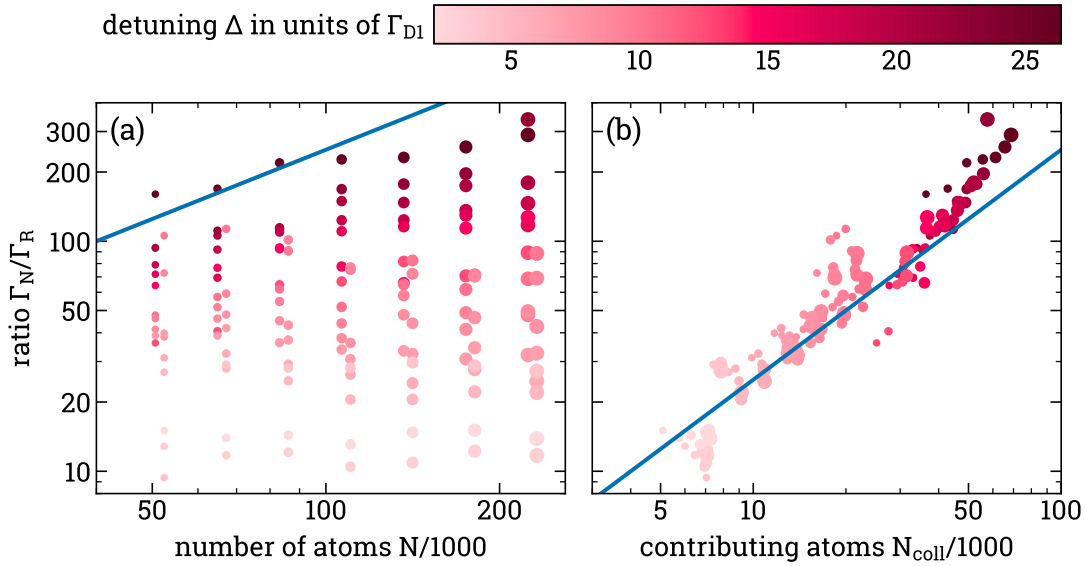

Figure 6.3: Ratio of measured enhanced scattering rate Γ_N and calculated single atom scattering rate Γ_R (defined in Equation (6.3)) versus (a) the total number of atoms in the HCPBGF and (b) the effective number of atoms N_{coll} contributing to the collective enhancement. N_{coll} is calculated using Equation (C.4), where we take into account the shadow effect and the ratio of excitation bandwidth and inhomogeneously broadened line width. The solid blue line corresponds to the expected linear dependence defined in Equation (6.1) with $\mu = 2.5 \times 10^{-3}$. The symbol size visualizes the total number of atoms N. We optimized the factor $\beta = 0.1$ for best agreement between experiment and theory.

Typically it is assumed that the pump beam interacts homogeneously with all atoms in the ensemble which leads to Equation (6.1). When we deviate from this assumption, we have to determine the fraction of emitters that contribute to the collective process [136]. In Appendix C we present a model developed by T. Peters and S. Stryzhenko to include the radial dependence of the atomic density and the pump Rabi frequency as well as the longitudinal attenuation of the pump field due to absorption and conversion into the Stokes field within the medium. Using that model, we can determine the number of atoms that effectively contribute to the collective SF emission N_{coll}. In Figure 6.3(b) we plot the ratio Γ_N/Γ_R as a function of the corrected number of atoms N_{coll}. The data now agrees very well with the expected linear dependence for the whole range of experimental parameters. We thus confirmed, that it is mandatory to include the radial inhomogeneities as well as the longitudinal attenuation of the pump field in order to describe SF in our HCPBGF.

Furthermore, in Figure 6.4(a) we show the dependence of the mean peak power $P_{max} \propto I_{max}$ of the SF signal on N_{coll}. According to [22], the peak intensity for the generated field is given by

$$I_{max} = \frac{1}{2} N^2 \Gamma_R \mu \hbar \omega_S. \tag{6.4}$$

As demonstrated by the exemplary fits in Figure 6.4(a), we observe very good agreement with the expected quadratic dependence for detunings in the range of

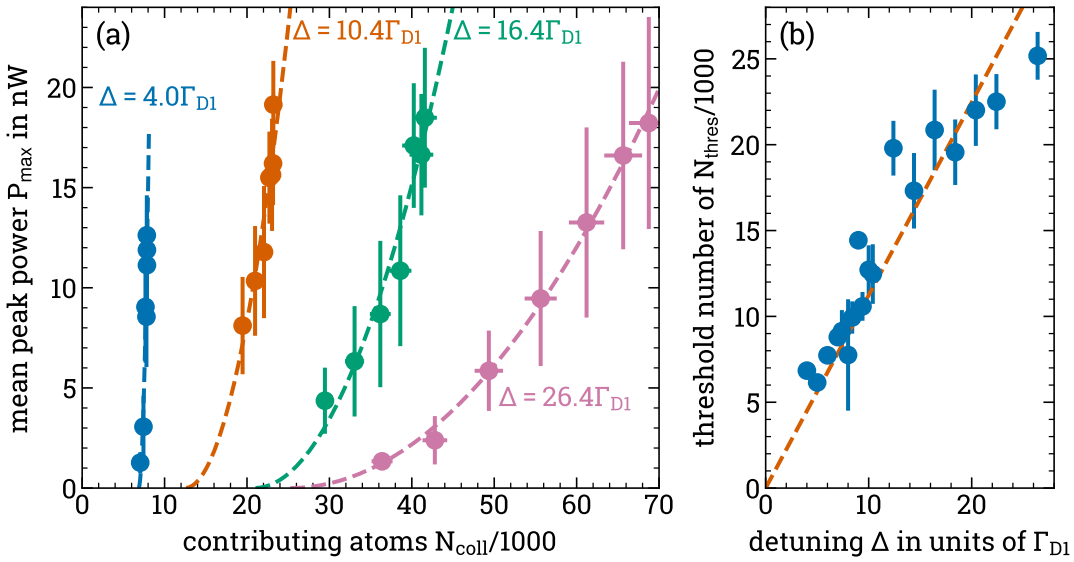

Figure 6.4: (a) Mean of the peak power P_{max} versus the collective atom number N_{coll} for four pump detunings Δ. The error bars correspond only to the uncertainty in the measured number of atoms N and do not include any further contribution from the calculation of N_{coll}. The dashed lines correspond to fits of form $P_{\text{max}} = a(N_{\text{coll}} - N_{\text{thres}})^2$. (b) Threshold number of atoms N_{thres} extracted from quadratic fits as shown in (a) versus the pump detuning Δ. The error bars depict the uncertainty of the best fit. The dashed line corresponds to a linear fit.

$\Delta = 4\,\Gamma_{\text{D1}}$ to $26.4\,\Gamma_{\text{D1}}$. We note, that for even smaller detunings the peak intensity reduces again for larger N_{coll}. A possible explanation could be absorption on the Stokes transition due to population redistribution into $|2\rangle$ by optical pumping that becomes more significant with reduced detuning and a higher total number of atoms. We extract the threshold number of contributing atoms N_{thres} required for SF emission as the minimum of the quadratic fits. In Figure 6.4(b) we plot N_{thres} as a function of the pump detuning Δ and observe a linear dependence. We explain this as follows: To observe SF, we require the dynamics of the process to be faster than the decoherence rate the system, i. e., $\Gamma_{\text{N}} \geq \gamma$ where equality corresponds to the threshold where SF sets on. Using Equation (6.1), we can rewrite the threshold condition in terms of the number of atoms as $\mu N_{\text{thres}} = \gamma/\Gamma_{\text{R}}$. For a decoherence rate dominated by the AC Stark shift, we have $\gamma \propto 1/\Delta$ while for the Raman scattering rate defined in Equation (6.3) we find $\Gamma_{\text{R}} \propto 1/\Delta^2$. Combined together we find $N_{\text{thes}} \propto \Delta$ as observed in the experiment.

In conclusion, we observed superradiant enhancement of the Raman scattering rate in an atomic ensemble confined in a HCPBGF. When taking into account attenuation of the pump field due to residual absorption, Raman gain, and the excitation bandwidth as well as the line broadening due to the inhomogeneous AC Stark shift in our medium, our observations agree well with established theory for SF in inverted two level systems. The strong light-matter coupling in our medium permits the observation of SF effects at low absolute numbers of atoms compared with typical free-space configurations.

Conclusion and Outlook

This research project dealt with the implementation of a non-classical photon-pair source based on spontaneous four-wave mixing (SFWM) in an ensemble of cold Rubidium atoms interfaced with a hollow-core photonic bandgap fiber (HCPBGF). Due to the single-mode guidance of the HCPBGF, we can achieve intrinsically optimal spatial mode matching of all four light fields in the SFWM process as well as optimal overlap between the guided light and the atomic ensemble within the fiber. The strong confinement of atoms and light fields within the HCPBGF leads to enhanced optical nonlinearities as compared to free-space setups.

In this thesis, we summarized the setup for the preparation of cold atoms inside the HCPBGF and presented a thorough characterization of the confined atomic ensemble in terms of the number of atoms, optical depth, coherence time, and EIT conditions. Subsequently, we introduced the extended setup for the detection and analysis of non-classical photons. Because all SFWM fields propagate collinear within the HCPBGF we could not use angular separation to filter the background of the strong pump fields in the photonic fields. Instead, we implemented a three stage filtering system based on polarization, tunable etalons and optical bandpasses. Furthermore, we implemented the detection and data acquisition system based on two HBT setups to measure auto-and cross-correlations of the generated photon pairs. In the analysis, we had to take the pulsed nature of our experiment into account when determining the normalization factors for the various correlation measurements.

In the main part, we presented a detailed analysis of the generated photon pairs [15]. We verified their non-classical nature by measuring the cross-correlation and compare it to the measured thermal auto-correlations of the individual fields. We observed a violation of the Cauchy-Schwarz inequality by a factor of 97(24), i. e., we exceeded the classical limit by about four standard deviations. The use of cold Rubidium atoms as our medium permitted the generation of intrinsically narrow biphotons. We determined the biphoton line width as $2\pi \times 6.5$ MHz which is compatible with atomic quantum memories and similar to the line width achievable with free-space setups. We can also view the photon pair source as a heralded source of single photons. Conditioned on the detection of a heralding event, we observed anti-bunched single photons manifested by a conditional auto-correlation of $0.16 \ll 0.5$. A high heralding efficiency of about 50 % was facilitated by the optimal mode matching and collection efficiency within the HCPBGF. Furthermore, a systematic comparison of the heralded auto-correlation with the cross correlation yielded good agreement with the theoretical expectation for a two-mode squeezed vacuum state.

Furthermore, by optimizing the experimental parameters towards a high generation rate we achieved a generated spectral brightness per pump power *GSBP* of up to 2×10^9 pairs $\mathrm{s}^{-1}\,\mathrm{MHz}^{-1}\,\mathrm{mW}^{-1}$ at pump powers below 100 nW and for a cross-correlation $\geq$3. Our results represent a 10-fold increase of the *GSBP* compared to the previous highest value [19] achieved using a micro-ring cavity. Our photon pairs exhibit a 10-fold reduced bandwidth and due to the pump beams guided

within the HCPBGF we require a 100-fold reduced pump power. Moreover, by increasing the generated spectral brightness even further, we reached the regime where different photon pairs start to overlap in time. Here, we demonstrated that the cross-correlation approaches a limit corresponding to thermal statistics.

Finally, in an additional experiment, we investigated SF scattering in the cold atomic ensemble within the HCPBGF. Such medium facilitates cooperative effects already at comparably low numbers of emitters due to the strong coupling between the guided light and the confined atoms. We developed a model to carefully determine the effective number of emitters involved in the collective scattering and observed the expected scaling for both the ratio between SF and single-atom scattering rate and the SF intensity versus the effective number of atoms.

Prospects for Future Work While our source can *generate* photons at a very high brightness, the *detected* brightness, i. e., the output rate of photons available for any subsequent application is currently limited by the duty cycle of the experiment. However, we believe that these limitations are only of technical nature and can be overcome. One could envision the following improvements: Using in-fiber magic-wavelength trapping [127, 128], the photon pairs could be generated continuously without the need to periodically modulate the guiding potential. Furthermore, the currently pulsed loading of the HCPBGF could be replaced with a continuous loading scheme. We estimate that this could enhance the detected pair rates by up to three orders of magnitude. In addition to that, intra-fiber laser cooling [130] could increase the coherence time and, thus, allow a further reducing of the biphoton bandwidth. Moreover, we note that as the generation of biphotons only requires atoms loaded *into* instead of *through* the fiber. Therefore, the output side of the HCPBGF could be spliced directly to a (polarization-maintaining) fiber [129], thereby avoiding coupling losses and enabling a direct connection to a fiber network or, depending on the application, a quantum frequency converter [44].

Furthermore, a detailed investigation of the photon statistics for the highest spectral brightness, where successive photon pairs overlap in time, may permit the generation of multi-photon states. To investigate this possibility, one has to extend the current analysis to include higher order coincidences. Currently, such measurements are limited by the DB that could be increased as proposed in the previous paragraph.

During this project, we also performed preliminary experiments on a single-step quantum frequency conversion to convert single photons from a wavelength of 795 nm to 606 nm in order to to make our Rubidium-based photon source compatible to Praseodymium-based quantum memories [125]. To that end, we set up a waveguide sum-frequency generation in a periodically-poled nonlinear crystal. The conversion was driven by a strong pump field at 2550 nm generated by a home-built optical parametric oscillator. We achieved a preliminary fiber-to-fiber conversion efficiency of about 10 % for weak coherent pulses that was limited by the pump coupling efficiency [137]. We estimate that a 30 % fiber-to-fiber conversion efficiency should be achievable with our approach. Especially in combination with our proposed improvements to the duty cycle, our source could then be applied in projects towards qubit storage in quantum memories.

Zusammenfassung

Die vorliegende Arbeit beschäftigt sich mit der Implementierung einer nichtklassischen Photonenpaarquelle basierend auf spontaner Vierwellenmischung in einem Ensemble kalter Atome im Inneren einer photonischen Kristall-Faser mit Hohlkern. Durch die Einzelmodenführung innerhalb der Faser wird eine optimale räumliche Modenanpassung aller beteiligter Lichtfelder, sowie optimaler Überlapp mit den kalten Atomen erreicht. Hierdurch kann eine stärkere Wechselwirkung zwischen Licht und Atomen als in Freistrahlexperimenten erreicht werden.

In dieser Arbeit wird zunächst der bestehende Aufbau zur Bereitstellung der kalten Atome innerhalb der Hohlkernfaser eingeführt und das Medium durch Messungen der Atomanzahl, optischer Dichte und Kohärenzzeit charakterisiert. Zudem wird das Vorliegen elektromagnetisch-induzierter Transparenz experimentell überprüft. Anschließend wird der Aufbau um Möglichkeiten zur Detektion und Analyse nichtklassischer Photonenpaare erweitert. Dadurch, dass alle beteiligten Felder in der gleichen räumlichen Mode propagieren, ist eine räumliche Separation der erzeugten Photonen von den starken Pumpfeldern nicht möglich. Stattdessen wird ein mehrstufiges Filtersystem basierend auf Polarisation, durchstimmbaren Resonatoren und schmalbandigen Bandpassfiltern verwendet. Zur Detektion der Photonen werden Hanbury Brown und Twiss Aufbauten in beiden Photonenkanälen implementiert. Im Rahmen der Datenanalyse muss der gepulste Betrieb des Experiments bei der Bestimmung der zeitabhängigen Normalisierungsfaktoren der Korrelationsfunktionen berücksichtigt werden.

Im Hauptteil der Arbeit werden die erzeugten Photonenpaare umfassend untersucht [15]. Zum Nachweis nichtklassischer Eigenschaften wird die Kreuzkorrelation bestimmt. Diese wird anschließend mit den gemessenen Werten der Autokorrelation verglichen. Die beobachtete Verletzung der Cauchy-Schwarzschen Ungleichung um einen Faktor 97(24) entspricht einer Überschreitung der klassischen Schranke um etwa vier Standardabweichungen. Durch die Nutzung kalter Atome können intrinsisch schmalbandige Photonenpaare erzeugt werden. Durch die gemessene Linienbreite von $2\pi\times6.5\,\mathrm{MHz}$ sind die erzeugten Photonen direkt kompatibel mit Quantenspeichern basierend auf atomaren Ensemblen. Die beobachteten Linienbreiten sind vergleichbar mit Freistrahlexperimenten. Photonenpaarquellen können auch als Einzelphotonenquellen mit Ankündigungsmechanismus (engl. *heralding*) interpretiert werden. Messungen der bedingten Autokorrelation von $0.16 \ll 0.5$ erbringen hier den Nachweis einer unterdrückten Mehrphotonenkomponente (engl. *anti-bunching*). Die hohe Ankündigungseffizienz von 50 % wird durch die optimale Modenanpassung der erzeugten Felder an die geführte Mode im Kern der Hohlfaser begünstigt. Beim Vergleich der bedingten Autokorrelation mit der Kreuzkorrelation wurde eine gute Übereinstimmung mit dem theoretisch erwarteten Zusammenhang für einen zweimodigen gequetschten Vakuumzustand (engl. *two-mode squeezed vacuum*) beobachtet.

Durch eine Optimierung der experimentellen Parameter konnte eine Photonenerzeugungsrate pro Frequenz und Pumpleistung von bis zu $2\times10^9\,\mathrm{s^{-1}\,MHz^{-1}\,mW^{-1}}$ bei Pumpleistungen unterhalb von 100 nW und einer Kreuzkorrelation $\geq$3 erreicht

werden. Diese Ergebnisse entsprechen eine Verbesserung um eine Größenordnung gegenüber dem bislang höchsten publizierten Wert [19], welcher in einem Experiment basierend auf einem Mikroringresonator beobachtet wurde. Die im Rahmen der vorliegenden Arbeit erzeugten Photonenpaare haben eine 10-fach geringere spektrale Bandbreite und es wurde eine 100-fach geringere Pumpleistung benötigt. Bei einer weiteren Erhöhung der Photonenerzeugungsrate beginnen die einzelnen Photonenpaare zeitlich zu überlappen. Unter diesen Bedingungen konvergiert die Kreuzkorrelation gegen den erwarteten Wert für thermische Photonenstatistik.

Zusätzlich wurde in einem separaten Experiment superfluoreszente Streuung in kalten Atomen im inneren der Hohlkernfaser untersucht. Durch die starke Kopplung von Licht und Materie können in diesem Medium kooperative Effekte bereits mit einer vergleichsweise kleinen Anzahl an Atomen realisiert werden. Mithilfe eines vorgestellten Modells, kann die relative Anzahl der am kollektiven Prozess beteiligten Atome bestimmt werden. Bei Verwendung dieser skaliert sowohl das Verhältnis aus superfluoreszenter und Ein-Atom-Streurate als auch die Intensität des superfluoreszenten Signals entsprechend der etablierten Theorie.

Appendix A

Polarization-Resolved Spatio-Temporal Simulation of SFWM

In this section we describe a numerical simulation developed by by S. Stryzhenko [15] that models the SFWM process taking into account a total of 16 magnetic sublevels of the involved hyperfine states as well as light field polarizations. This simulation served to confirm the polarizations of the generated S and AS fields for varying polarization configurations ($\parallel$ and $\perp$) of the pump and control fields. This was necessary as we are currently unable to prepare the population in a single Zeeman state and use arbitrary polarizations configurations as in free-space setups due to the HCPBGF's birefringence, which requires the use of linear polarizations.

We assume classical fields, use a plane-wave approximation and describe the atom-field interactions using a density matrix approach in rotating wave approximation. We simulate the process of SFWM by solving a system of partial differential equations which represent light propagation and time evolution of the density matrix operator $\hat{\rho}$ with appropriate random initial conditions.

Denoting the set of magnetic sublevels of the ground states $|1\rangle$ and $|2\rangle$ by the index g and a similar set of magnetic sublevels of the excited states by the index e we can write the density matrix equations in the short matrix form. In this notation all quantum operators are spelled as block matrices:

$$\hat{O} = \begin{bmatrix} O_{gg} & O_{ge} \\ O_{eg} & O_{ee} \end{bmatrix}. \tag{A.1}$$

Then the propagation equations read

$$\frac{\partial E_m(z,t)}{\partial z} = -4\pi \mathrm{i} k_m \mathcal{N} \,\mathrm{tr}[\hat{\mu}^m_{ge} \cdot \rho_{eg}(z,t)]. \tag{A.2}$$

Here E_m is the complex amplitude of the electric field in mode m, k_m is its wavenumber, and $\hat{\mu}^m$ is the mode's dipole moment operator where the matrix elements are taken from [84]. The mode index m runs across all fields we take into account (pump, control, Stokes, and anti-Stokes), as well as their respective polarizations, where we use $\sigma^{\pm}$ as a polarization basis.

The time evolution matrix equations for the density matrix read (here and below we assume $\Gamma_{D1} \simeq \Gamma_{D2} \simeq \Gamma$)

$$\begin{aligned}
\frac{\partial \rho_{gg}}{\partial t} &= \mathrm{i}[\rho_{gg}, \Delta_g] + \frac{\mathrm{i}}{2}(\rho_{ge} \cdot \Omega_{eg} - \Omega_{ge} \cdot \rho_{eg}) + \Gamma R_g \circ C_{ge} \cdot \rho_{ee} \cdot C_{eg} - \gamma \circ \rho_{gg}, \\
\frac{\partial \rho_{eg}}{\partial t} &= \mathrm{i}(\rho_{eg} \cdot \Delta_g - \Delta_e \cdot \rho_{eg}) + \frac{\mathrm{i}}{2}(\rho_{ee} \cdot \Omega_{eg} - \Omega_{eg} \cdot \rho_{gg}) - \frac{\Gamma}{2}(C_{eg} \cdot C_{ge}) \cdot \rho_{eg}, \\
\frac{\partial \rho_{ee}}{\partial t} &= \mathrm{i}[\rho_{ee}, \Delta_e] + \frac{\mathrm{i}}{2}(\rho_{eg} \cdot \Omega_{ge} - \Omega_{eg} \cdot \rho_{ge}) - \frac{\Gamma}{2}\{C_{eg} \cdot C_{ge}, \rho_{ee}\}.
\end{aligned} \tag{A.3}$$

Here, Δ_g and Δ_e are diagonal matrices with the summed detunings of the considered modes on the diagonal. $\Omega_{ge} = \Omega_{eg}^{\dagger}$ are submatrices of the Rabi frequency operator defined by $\hbar\hat{\Omega} = \sum_m E_m \hat{\mu}^m$. The matrices $C_{ge} = C_{eg}^{\dagger}$ contain the Clebsch-Gordan coefficients as follows:

$$\left\langle \begin{matrix} F_e \\ M_e \end{matrix} \middle| C_{eg} \middle| \begin{matrix} F_g \\ M_g \end{matrix} \right\rangle = \langle F_e, M_e | F_g, M_g; 1, M_e - M_g \rangle . \tag{A.4}$$

R_g is the Kronecker delta of the F quantum number:

$$\left\langle \begin{matrix} F_1 \\ M_1 \end{matrix} \middle| R_g \middle| \begin{matrix} F_2 \\ M_2 \end{matrix} \right\rangle = \delta_{F_1 F_2} \tag{A.5}$$

and the operation $\circ$ stands for the element-wise multiplication of matrices. This way, R_g prevents coherence between $|1\rangle$ and $|2\rangle$ being generated when population is transferred from the excited to the ground levels.

The matrix γ describes decoherence effects in the ground states:

$$\left\langle \begin{matrix} F_1 \\ M_1 \end{matrix} \middle| \gamma \middle| \begin{matrix} F_2 \\ M_2 \end{matrix} \right\rangle = \begin{cases} 0 \text{ if } F_1 = F_2 \text{ and } M_1 = M_2, \\ \gamma_{12} \text{ otherwise.} \end{cases} \tag{A.6}$$

To imitate the vacuum fluctuations we set the Stokes field at the beginning of the fiber to a random value with correlation time $1/\Gamma$ in the following way:

$$\begin{aligned}
&E_{S\pm}(z = 0, t = 0) = 0, \\
&E_{S\pm}(z = 0, t + \delta t) = E_{S\pm}(z = 0, t) e^{-\frac{\Gamma_{D2}}{2}\delta t} + \nu_{\pm} E_{\text{vacuum}} \sqrt{1 - e^{-\Gamma_{D2}\delta t}},
\end{aligned} \tag{A.7}$$

where $\delta t \ll 1/\Gamma$ is the time step, $\nu_{\pm}$ is a random complex number from the normalized complex Gaussian distribution, and the field E_{vacuum} corresponds to the Rabi frequency of $\sim 10^{-5}\Gamma$. The sign $\pm$ in the index points out that we use these initial conditions both for the left and the right polarization components.

The time evolution Equation (A.3) with initial conditions (A.7) were solved numerically using the Kutta-Merson method. On each Kutta-Merson step we solved the propagation Equation (A.2) by integrating its right-hand side using Simpson's rule[138].

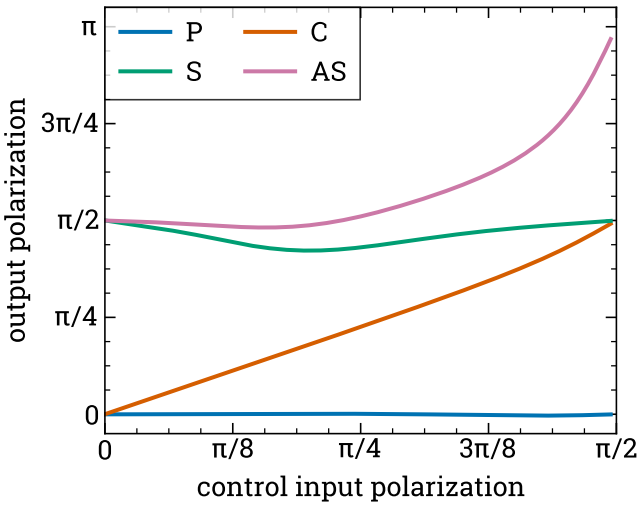

Figure A.1: Simulated dependence of the polarization of the pump (P), control (C), Stokes (S) and anti-Stokes (AS) fields polarization at the output side of the medium versus the control polarization on the input side. The input pump polarization remains fixed. The coupling scheme is shown in Figure 4.1. Simulation parameters are $\Omega_P = \Omega_C = 6\,\Gamma$ and $N = 150 \times 10^3$.

Figure A.1 shows the results of this simulation. We confirm that the generated S and AS fields exhibit orthogonal linear polarizations with respect to the injected pump and control fields of also linear orthogonal polarizations. Therefore it was experimentally possible to use polarization filtering (see Section 4.2.1) in addition to frequency filtering and obtain a sufficiently high extinction ratio for the strong colinear pump and control fields.

Appendix B

Model for the Detected Cross-Correlation

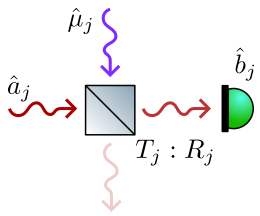

Figure B.1: Beamsplitter transformation to include noise and detection efficiency.

In this section we present a simple single-mode model [139] that incorporates loss and detector inefficiencies for the fit of the cross-correlation function $g^{(2)}_{\mathrm{S,AS}}$. The model was derived by E. Giese [15]. We start by introducing the bosonic annihilation operator

$$\hat{b}_j = t_j \hat{a}_j + r_j \hat{\mu}_j \tag{B.1}$$

of photons detected in channel $j = \mathrm{S,AS}$. Here, $\hat{a}_j$ denotes the (bosonic) annihilation operator of Stokes or anti-Stokes photons generated during SFWM and $\hat{\mu}_j$ the (bosonic) annihilation operator of noise photons in channel j. Imperfect detection is introduced in Equation (B.1) though the beamsplitter transformation illustrated in Figure B.1 with $T_j + R_j = |t_j|^2 + |r_j|^2 = 1$. Hence, T_j is the efficiency of the detector including all loss in channel j.

If we assume no correlation between the noise and the generated photons, i. e., $\langle \hat{a}_j^\dagger \hat{\mu}_j \rangle = 0$, we can connect the detected photon numbers $N_j = \langle \hat{b}_j^\dagger \hat{b}_j \rangle = T_j n_j + \mathcal{N}_j$ to the number of generated Stokes and anti-Stokes photons $n_j = \langle \hat{a}_j^\dagger \hat{a}_j \rangle$. We furthermore introduced the noise detected in channel j through $\mathcal{N}_j = R_j \langle \hat{\mu}_j^\dagger \hat{\mu}_j \rangle$.

The detected cross-correlation function $g^{(2)}_{\mathrm{S,AS}} = \langle \hat{b}_\mathrm{S}^\dagger \hat{b}_\mathrm{AS}^\dagger \hat{b}_\mathrm{S} \hat{b}_\mathrm{AS} \rangle / (N_\mathrm{S} N_\mathrm{AS})$ takes the form

$$g^{(2)}_{\mathrm{S,AS}} = \frac{\langle \hat{a}_\mathrm{S}^\dagger \hat{a}_\mathrm{AS}^\dagger \hat{a}_\mathrm{S} \hat{a}_\mathrm{AS} \rangle}{n_\mathrm{S} n_\mathrm{AS}} \frac{T_\mathrm{S} n_\mathrm{S} T_\mathrm{AS} n_\mathrm{AS}}{N_\mathrm{S} N_\mathrm{AS}} + \frac{\mathcal{N}_\mathrm{S} \mathcal{N}_\mathrm{AS}}{N_\mathrm{S} N_\mathrm{AS}}. \tag{B.2}$$

Here, we have again assumed no correlation between the noise and the generated photons, i. e., $\langle \hat{a}_\mathrm{S}^\dagger \hat{a}_\mathrm{AS}^\dagger \hat{\mu}_\mathrm{S} \hat{\mu}_\mathrm{AS} \rangle = 0$ and uncorrelated noise in both channels, i. e., $R_\mathrm{S} R_\mathrm{AS} \langle \hat{\mu}_\mathrm{S}^\dagger \hat{\mu}_\mathrm{AS}^\dagger \hat{\mu}_\mathrm{S} \hat{\mu}_\mathrm{AS} \rangle = \mathcal{N}_\mathrm{S} \mathcal{N}_\mathrm{AS}$.

If there is perfect correlation between Stokes and anti-Stokes fields, the number of photons generated in each channel corresponds to the number of generated pairs $n = n_\mathrm{S} = n_\mathrm{AS}$. We have verified that both the Stokes and anti-Stokes fields exhibit close to thermal statistics, which directly implies $\langle \hat{a}_\mathrm{S}^\dagger \hat{a}_\mathrm{AS}^\dagger \hat{a}_\mathrm{S} \hat{a}_\mathrm{AS} \rangle / (n_\mathrm{S} n_\mathrm{AS}) = 2 + 1/n$ for perfectly correlated fields. In this case, the cross-correlation function takes the form

$$g^{(2)}_{\mathrm{S,AS}} = \frac{2 + \frac{1}{n} + \frac{\mathcal{N}_\mathrm{S} \mathcal{N}_\mathrm{AS}}{T_\mathrm{S} T_\mathrm{AS} n^2}}{\left[1 + \frac{\mathcal{N}_\mathrm{S}}{T_\mathrm{S} n}\right]\left[1 + \frac{\mathcal{N}_\mathrm{AS}}{T_\mathrm{AS} n}\right]} \tag{B.3}$$

and reduces to the ideal case for negligible noise. For dominant noise, however, the cross-correlation approaches the limit of $1 + 1/(n + \mathcal{N})$. Note that in a multi-mode model the number 2 has to be replaced by $1 + 1/M$, where M is the number of detected modes [140].

To determine the noise for the fits in Figures 5.3 and 5.8 we use the noise model introduced in Section 4.2.1 and make the ansatz $\mathcal{N}_j(P) = \mathfrak{R}_j(P)\tau_c$ for the noise contribution on the characteristic time scale of our biphotons, i. e., $\tau_c = 24\,\mathrm{ns}$, obtained from the data in Figure 5.1. Moreover, we use $T_S = T_{AS} = 0.08$ in accordance with the measured transmission losses and specified detector efficiencies.

Appendix C

Model for the Collective Number of Atoms Contributing to Superfluorescence

In this section we present the model developed by T. Peters and S. Stryzhenko to determine the collective number of atoms N_{coll} that contribute to the SF emission within the HCPBGF. We include the radial dependence of the atomic density and the pump Rabi frequency as well as the longitudinal attenuation of the pump field within the medium. Note, that our theory is derived in a rather phenomenological way and might not be analytically rigorous.

To estimate the effect of the radial inhomogenities, we first approximate the excitation bandwidth of the pump field as $\sigma_{\text{exc}} \approx 2\pi \times 1.3\,\text{MHz}$ determined by the rise time of the pump pulse of about 120 ns. We have to compare this to the inhomogeneous line width σ_{inh} of of our medium to estimate the fraction of atoms that are coupled by our pump field. To account for inhomogeneous broadening by the Gaussian pump profile and the Gaussian radial atomic density distribution (compare Figure 3.8(b)) we calculate the variance of the ground state Stark shift $S = \Omega_{\text{P}}^2/(4\Delta)$ as $\text{var}(S) = \langle (S - \langle S \rangle_r)^2 \rangle_r \lesssim (2\,\Gamma_{\text{D1}})^2$ and the Raman scattering rate $\text{var}(\Gamma_{\text{R}}) = \langle (\Gamma_{\text{R}} - \langle \Gamma_{\text{R}} \rangle_r)^2 \rangle_r \lesssim (10^{-2}\,\Gamma_{\text{D1}})^2$. The estimated inhomogeneous line width $\sigma_{\text{inh}} = \sqrt{\text{var}(S)} + \sqrt{\text{var}(\Gamma_{\text{R}})}$ is thus dominated by the Stark shift. We clip the ratio $\sigma_{\text{exc}}/\sigma_{\text{inh}}$ to values ≤ 1 to avoid artificial enhancement and find ratios between 0.2 and 1 for our experimental parameters.

We now turn to the longitudinal effects along the propagation axis that change the pump intensity $I_{\text{P}}(z)$. For media of high optical depth, even at detunings $\Delta \gg \Gamma_{\text{D1}}$, we have significant residual absorption. Atoms positioned at large $z \sim L$ interact only with a weakened "shadow" of the pump field that is attenuated due to absorption in the initial part of the medium $z \ll L$. We include this *shadow effect* [141] as $I_{\text{P}}(z) = I_{\text{P}}^{(0)} \exp^{-\alpha(\Delta) z}$. In addition to absorption, we include pump depletion due to conversion into the Stokes field [27]. It can be shown [60, 142] that the Intensity of the generated Stokes field increases as $I_R^{(0)} \propto e^{G_{\text{R}}}$ with the Raman Gain for $\gamma \gg \Gamma_{\text{R}}$ given by

$$G_{\text{R}} \propto \alpha_0 \frac{2\Gamma_{\text{R}}}{\gamma}, \tag{C.1}$$

where α_0 is the resonant absorption coefficient proportional to the number of atoms N. In the decoherence rate $\gamma = \gamma_{12} + \sqrt{\text{var}(S)} + \langle \Gamma_{\text{R}} \rangle_r$ we include the the radially inhomogeneous Stark shift and scattering rate in addition to the intrinsic ground state decoherence rate $\gamma_{12} = 0.057\,\Gamma_{\text{D1}}$ measured by EIT LS (see Section 3.5). For the majority of experimental parameters, the decoherence rate is dominated by the contribution of the inhomogeneous Stark shift of the order of Γ_{D1} while $\langle \Gamma_{\text{R}} \rangle_r \lesssim 0.05\,\Gamma_{\text{D1}}$. We further assume that the pump field is attenuated by the same factor, i. e., it is only converted into the Stokes field and we can write

$I_\mathrm{P}(z) \propto \exp(-\beta G_\mathrm{R})$ with a scaling factor β to account for any spatial and temporal dependence of the Raman gain that we otherwise neglect in our approximation. We combine the effects of absorption and pump conversions into an effective absorption coefficient

$$\alpha_\mathrm{eff} = \alpha_0 \frac{\Gamma_\mathrm{D1}^2 + \beta\Gamma_\mathrm{D1}\langle\Omega_\mathrm{P}^2\rangle_r/\gamma}{\Gamma_\mathrm{D1}^2 + 4(\Delta + \langle S\rangle_r)^2 + 2\langle\Omega_\mathrm{P}^2\rangle_r}. \tag{C.2}$$

With the definition (C.2) we calculate the longitudinal average of the Raman scattering rate

$$\Gamma_R' = R_\mathrm{B}\Gamma_{D_1}\frac{1}{L}\int_0^L \mathrm{d}z \frac{\langle\Omega_\mathrm{P}^2\rangle_r \exp(-\alpha_\mathrm{eff} z)}{\Gamma_{D_1}^2 + 4(\Delta + \langle S\rangle_r)^2 + 2\langle\Omega_\mathrm{P}^2\rangle_r \exp(-\alpha_\mathrm{eff} z)}. \tag{C.3}$$

By calculating the ratio between this generalized scattering rate (C.3) and the basic definition (6.3), we can summarize all longitudinal effects into a *shadow factor* $\eta_\mathrm{s} = \Gamma_\mathrm{R}'/\Gamma_\mathrm{R}$. For our experimental parameters we obtain values between 0.1 and 0.7. Finally, we can incorporate both the radial and longitudinal corrections into the collective atom number

$$N_\mathrm{coll} = \frac{\sigma_\mathrm{exc}}{\sigma_\mathrm{inh}}\eta_\mathrm{S} N, \tag{C.4}$$

i. e., the effective number of atoms that take part in the collective enhancement of the emission process. We use this corrected N_coll in Chapter 6 when we compare our observations to the theory for traditional superradiance.

Bibliography

[1] M. A. Nielsen and I. L. Chuang. *Quantum Computation and Quantum Information: 10th Anniversary Edition* 1st ed. (Cambridge University Press, Cambridge, New York, 2012).

[2] T. D. Ladd *et al.* "Quantum Computers". Nature **464,** 45–53 (2010).

[3] A. K. Fedorov, N. Gisin, S. M. Beloussov, and A. I. Lvovsky. *Quantum Computing at the Quantum Advantage Threshold: A down-to-Business Review.* http://arxiv.org/abs/2203.17181v1 (Mar. 31, 2022). preprint.

[4] H. J. Kimble. "The Quantum Internet". Nature **453,** 1023–1030 (2008).

[5] S. Wehner, D. Elkouss, and R. Hanson. "Quantum Internet: A Vision for the Road Ahead". Science **362,** eaam9288 (2018).

[6] V. Scarani *et al.* "The Security of Practical Quantum Key Distribution". Reviews of Modern Physics **81,** 1301–1350 (2009).

[7] F. Flamini, N. Spagnolo, and F. Sciarrino. "Photonic Quantum Information Processing: A Review". Reports on Progress in Physics **82,** 016001 (2018).

[8] N. Sangouard, C. Simon, H. de Riedmatten, and N. Gisin. "Quantum Repeaters Based on Atomic Ensembles and Linear Optics". Reviews of Modern Physics **83,** 33–80 (2011).

[9] S. Slussarenko and G. J. Pryde. "Photonic Quantum Information Processing: A Concise Review". Applied Physics Reviews **6,** 041303 (2019).

[10] M. D. Eisaman, J. Fan, A. Migdall, and S. V. Polyakov. "Invited Review Article: Single-photon Sources and Detectors". Review of Scientific Instruments **82,** 071101 (2011).

[11] Y. Wang, K. D. Jöns, and Z. Sun. "Integrated Photon-Pair Sources with Nonlinear Optics". Applied Physics Reviews **8,** 011314 (2021).

[12] A. Anwar, C. Perumangatt, F. Steinlechner, T. Jennewein, and A. Ling. "Entangled Photon-Pair Sources Based on Three-Wave Mixing in Bulk Crystals". Review of Scientific Instruments **92,** 041101 (2021).

[13] C.-S. Chuu and S. Du. *Narrowband Biphotons: Generation, Manipulation, and Applications.* in *Engineering the Atom-Photon Interaction* (eds A. Predojević and M. W. Mitchell) 145–182 (Springer, Cham, Heidelberg, New York, 2015).

[14] O. Slattery, L. Ma, K. Zong, and X. Tang. "Background and Review of Cavity-Enhanced Spontaneous Parametric Down-Conversion". Journal of Research of the National Institute of Standards and Technology **124,** 124019 (2019).

[15] A. Bruns *et al.* "Ultrabright and Narrowband Intra-Fiber Biphoton Source at Ultralow Pump Power". Quantum Science and Technology **8,** 015002 (2023).

[16] M. Cordier, P. Delaye, F. Gérôme, F. Benabid, and I. Zaquine. “Raman-Free Fibered Photon-Pair Source”. Scientific Reports **10,** 1650 (2020).

[17] S. Lopez-Huidobro, M. Lippl, N. Y. Joly, and M. V. Chekhova. “Fiber-Based Biphoton Source with Ultrabroad Frequency Tunability”. Optics Letters **46,** 4033–4036 (2021).

[18] N. V. Corzo *et al.* “Waveguide-Coupled Single Collective Excitation of Atomic Arrays”. Nature **566,** 359–362 (2019).

[19] T. J. Steiner *et al.* “Ultrabright Entangled-Photon-Pair Generation from an AlGaAs-On-Insulator Microring Resonator”. PRX Quantum **2,** 010337 (2021).

[20] R. H. Dicke. “Coherence in Spontaneous Radiation Processes”. Physical Review **93,** 99–110 (1954).

[21] R. Bonifacio and L. A. Lugiato. “Cooperative Radiation Processes in Two-Level Systems: Superfluorescence”. Physical Review A **11,** 1507–1521 (1975).

[22] M. Gross and S. Haroche. “Superradiance: An Essay on the Theory of Collective Spontaneous Emission”. Physics Reports **93,** 301–396 (1982).

[23] W. Guerin, M. Rouabah, and R. Kaiser. “Light Interacting with Atomic Ensembles: Collective, Cooperative and Mesoscopic Effects”. Journal of Modern Optics **64,** 895–907 (2017).

[24] F. Couny, O. Carraz, and F. Benabid. “Control of Transient Regime of Stimulated Raman Scattering Using Hollow-Core PCF”. Journal of the Optical Society of America B **26,** 1209–1215 (2009).

[25] E. Paradis, B. Barrett, A. Kumarakrishnan, R. Zhang, and G. Raithel. “Observation of Superfluorescent Emissions from Laser-Cooled Atoms”. Physical Review A **77,** 043419 (2008).

[26] A. Goban *et al.* “Superradiance for Atoms Trapped along a Photonic Crystal Waveguide”. Physical Review Letters **115,** 063601 (2015).

[27] M. G. Raymer and J. Mostowski. “Stimulated Raman Scattering: Unified Treatment of Spontaneous Initiation and Spatial Propagation”. Physical Review A **24,** 1980–1993 (1981).

[28] H. Edlbauer *et al.* “Semiconductor-Based Electron Flying Qubits: Review on Recent Progress Accelerated by Numerical Modelling”. EPJ Quantum Technology **9,** 1–36 (2022).

[29] R. Bedington, J. M. Arrazola, and A. Ling. “Progress in Satellite Quantum Key Distribution”. npj Quantum Information **3,** 1–13 (2017).

[30] H.-J. Briegel, W. Dür, J. I. Cirac, and P. Zoller. “Quantum Repeaters: The Role of Imperfect Local Operations in Quantum Communication”. Physical Review Letters **81,** 5932–5935 (1998).

[31] C. Simon *et al.* “Quantum Memories”. The European Physical Journal D **58,** 1–22 (2010).

[32] E. Meyer-Scott, C. Silberhorn, and A. Migdall. “Single-Photon Sources: Approaching the Ideal through Multiplexing”. Review of Scientific Instruments **91,** 041101 (2020).

[33] S. Chen *et al.* “Deterministic and Storable Single-Photon Source Based on a Quantum Memory”. Physical Review Letters **97,** 173004 (2006).

[34] C. Gerry and P. Knight. *Introductory Quantum Optics* (Cambridge University Press, Cambridge, New York, 2005).

[35] R. Hanbury Brown and R. Q. Twiss. “Correlation between Photons in Two Coherent Beams of Light”. Nature **177,** 27–29 (1956).

[36] R. Loudon. *The Quantum Theory of Light* 3rd ed. (Oxford University Press, Oxford, New York, 2000).

[37] P. Grangier, G. Roger, and A. Aspect. “Experimental Evidence for a Photon Anticorrelation Effect on a Beam Splitter: A New Light on Single-Photon Interferences”. Europhysics Letters **1,** 173–179 (1986).

[38] P. Grünwald. “Effective Second-Order Correlation Function and Single-Photon Detection”. New Journal of Physics **21,** 093003 (2019).

[39] J. F. Clauser. “Experimental Distinction between the Quantum and Classical Field-Theoretic Predictions for the Photoelectric Effect”. Physical Review D **9,** 853–860 (1974).

[40] X. Cao, M. Zopf, and F. Ding. “Telecom Wavelength Single Photon Sources”. Journal of Semiconductors **40,** 071901 (2019).

[41] G. Heinze, C. Hubrich, and T. Halfmann. “Stopped Light and Image Storage by Electromagnetically Induced Transparency up to the Regime of One Minute”. Physical Review Letters **111,** 033601 (2013).

[42] M. Afzelius, C. Simon, H. de Riedmatten, and N. Gisin. “Multimode Quantum Memory Based on Atomic Frequency Combs”. Physical Review A **79,** 052329 (2009).

[43] E. Saglamyurek *et al.* “Broadband Waveguide Quantum Memory for Entangled Photons”. Nature **469,** 512–515 (2011).

[44] B. Albrecht, P. Farrera, X. Fernandez-Gonzalvo, M. Cristiani, and H. de Riedmatten. “A Waveguide Frequency Converter Connecting Rubidium-Based Quantum Memories to the Telecom C-band”. Nature Communications **5,** 3376 (2014).

[45] N. Maring *et al.* “Photonic Quantum State Transfer between a Cold Atomic Gas and a Crystal”. Nature **551,** 485–488 (2017).

[46] B. Lounis and M. Orrit. “Single-Photon Sources”. Reports on Progress in Physics **68,** 1129 (2005).

[47] I. Aharonovich, D. Englund, and M. Toth. “Solid-State Single-Photon Emitters”. Nature Photonics **10,** 631–641 (2016).

[48] H. Mäntynen, N. Anttu, Z. Sun, and H. Lipsanen. “Single-Photon Sources with Quantum Dots in III–V Nanowires”. Nanophotonics **8,** 747–769 (2019).

[49] E. Brambila, R. Gómez, R. Fazili, M. Gräfe, and F. Steinlechner. “Ultrabright Polarization-Entangled Photon Pair Source for Frequency-Multiplexed Quantum Communication in Free-Space”. Optics Express **31,** 16107–16117 (2023).

[50] C.-H. Wu *et al.* “Bright Single Photons for Light-Matter Interaction”. Physical Review A **96,** 023811 (2017).

[51] P.-J. Tsai and Y.-C. Chen. “Ultrabright, Narrow-Band Photon-Pair Source for Atomic Quantum Memories”. Quantum Science and Technology **3,** 034005 (2018).

[52] C.-Y. Hsu *et al.* “Generation of Sub-MHz and Spectrally-Bright Biphotons from Hot Atomic Vapors with a Phase Mismatch-Free Scheme”. Optics Express **29,** 4632–4644 (2021).

[53] Y.-S. Wang *et al.* “Temporally Ultralong Biphotons with a Linewidth of 50 kHz”. APL Photonics **7,** 126102 (2022).

[54] L.-M. Duan, M. D. Lukin, J. I. Cirac, and P. Zoller. “Long-Distance Quantum Communication with Atomic Ensembles and Linear Optics”. Nature **414,** 413–418 (2001).

[55] P. Farrera *et al.* “Generation of Single Photons with Highly Tunable Wave Shape from a Cold Atomic Ensemble”. Nature Communications **7,** 13556 (2016).

[56] C. Laplane, P. Jobez, J. Etesse, N. Gisin, and M. Afzelius. “Multimode and Long-Lived Quantum Correlations Between Photons and Spins in a Crystal”. Physical Review Letters **118,** 210501 (2017).

[57] K.-H. Luo *et al.* “Direct Generation of Genuine Single-Longitudinal-Mode Narrowband Photon Pairs”. New Journal of Physics **17,** 073039 (2015).

[58] J.-M. Chen *et al.* “Room-Temperature Biphoton Source with a Spectral Brightness near the Ultimate Limit”. Physical Review Research **4,** 023132 (2022).

[59] D. A. Braje, V. Balić, S. Goda, G. Y. Yin, and S. E. Harris. “Frequency Mixing Using Electromagnetically Induced Transparency in Cold Atoms”. Physical Review Letters **93,** 183601 (2004).

[60] V. Balić, D. A. Braje, P. Kolchin, G. Y. Yin, and S. E. Harris. “Generation of Paired Photons with Controllable Waveforms”. Physical Review Letters **94,** 183601 (2005).

[61] S. Du, J. Wen, and M. H. Rubin. “Narrowband Biphoton Generation near Atomic Resonance”. Journal of the Optical Society of America B **25,** C98–C108 (2008).

[62] M. Fleischhauer, A. Imamoglu, and J. P. Marangos. “Electromagnetically Induced Transparency: Optics in Coherent Media”. Reviews of Modern Physics **77,** 633–673 (2005).

[63] C. Shu *et al.* “Subnatural-Linewidth Biphotons from a Doppler-broadened Hot Atomic Vapour Cell”. Nature Communications **7,** 12783 (2016).

[64] R. J. Glauber. “The Quantum Theory of Optical Coherence”. Physical Review **130,** 2529–2539 (1963).

[65] P. Kolchin. “Electromagnetically-Induced-Transparency-Based Paired Photon Generation”. Physical Review A **75,** 033814 (2007).

[66] S. Du, P. Kolchin, C. Belthangady, G. Y. Yin, and S. E. Harris. “Subnatural Linewidth Biphotons with Controllable Temporal Length”. Physical Review Letters **100,** 183603 (2008).

[67] P. Russell. “Photonic Crystal Fibers”. Science **299,** 358–362 (2003).

[68] F. Poletti, M. N. Petrovich, and D. J. Richardson. “Hollow-Core Photonic Bandgap Fibers: Technology and Applications”. Nanophotonics **2,** 315–340 (2013).

[69] B. Debord, F. Amrani, L. Vincetti, F. Gérôme, and F. Benabid. “Hollow-Core Fiber Technology: The Rising of “Gas Photonics””. Fibers **7,** 16 (2019).

[70] F. Blatt, T. Halfmann, and T. Peters. “One-Dimensional Ultracold Medium of Extreme Optical Depth”. Optics Letters **39,** 446–449 (2014).

[71] J. T. Kristensen, A. Houmann, X. Liu, and D. Turchinovich. “Low-Loss Polarization-Maintaining Fusion Splicing of Single-Mode Fibers and Hollow-Core Photonic Crystal Fibers, Relevant for Monolithic Fiber Laser Pulse Compression”. Optics Express **16,** 9986–9995 (2008).

[72] T. Peters, L. P. Yatsenko, and T. Halfmann. “Loading and Spatially Resolved Characterization of a Cold Atomic Ensemble inside a Hollow-Core Fiber”. Physical Review A **103,** 063302 (2021).

[73] J. D. Joannopoulos, S. G. Johnson, J. N. Winn, and R. D. Meade. *Photonic Crystals: Molding the Flow of Light* 2nd ed. (Princeton University Press, Princeton, 2008).

[74] R. F. Cregan *et al.* “Single-Mode Photonic Band Gap Guidance of Light in Air”. Science **285,** 1537–1539 (1999).

[75] F. Couny, F. Benabid, and P. S. Light. “Large-Pitch Kagome-Structured Hollow-Core Photonic Crystal Fiber”. Optics Letters **31,** 3574–3576 (2006).

[76] A. Hilton *et al.* “High-Efficiency Cold-Atom Transport into a Waveguide Trap”. Physical Review Applied **10,** 044034 (2018).

[77] M. Langbecker *et al.* “Highly Controlled Optical Transport of Cold Atoms into a Hollow-Core Fiber”. New Journal of Physics **20,** 083038 (2018).

[78] F. Amrani *et al.* “Low-Loss Single-Mode Hybrid-Lattice Hollow-Core Photonic-Crystal Fibre”. Light: Science & Applications **10,** 7 (2021).

[79] W. Belardi. “Design and Properties of Hollow Antiresonant Fibers for the Visible and Near Infrared Spectral Range”. Journal of Lightwave Technology **33,** 4497–4503 (2015).

[80] M. S. Habib, O. Bang, and M. Bache. “Low-Loss Single-Mode Hollow-Core Fiber with Anisotropic Anti-Resonant Elements”. Optics Express **24,** 8429–8436 (2016).

[81] W. Ni *et al.* “Recent Advancement of Anti-Resonant Hollow-Core Fibers for Sensing Applications”. Photonics **8,** 128 (2021).

[82] T. Peters, T.-P. Wang, A. Neumann, L. S. Simeonov, and T. Halfmann. “Single-Photon-Level Narrowband Memory in a Hollow-Core Photonic Bandgap Fiber”. Optics Express **28,** 5340–5354 (2020).

[83] F. Poletti, N. G. R. Broderick, D. J. Richardson, and T. M. Monro. “The Effect of Core Asymmetries on the Polarization Properties of Hollow Core Photonic Bandgap Fibers”. Optics Express **13,** 9115–9124 (2005).

[84] D. A. Steck. *Rubidium 87 D Line Data.* revision 2.2.2. http://steck.us/alkalidata (July 9, 2021).

[85] W. Demtröder. *Experimentalphysik 3: Atome, Moleküle Und Festkörper* 5th ed. (Springer, Berlin, Heidelberg, 2016).

[86] T. Mayer-Kuckuk. *Atomphysik* (Vieweg+Teubner Verlag, Wiesbaden, 1997).

[87] F. Blatt. “Stationäre Lichtpulse und Lichtspeicherung in einem eindimensionalen kalten atomaren Ensemble hoher optischer Dichte”. Dissertation, TU Darmstadt (2016).

[88] F. Blatt, L. S. Simeonov, T. Halfmann, and T. Peters. “Stationary Light Pulses and Narrowband Light Storage in a Laser-Cooled Ensemble Loaded into a Hollow-Core Fiber”. Physical Review A **94,** 043833 (2016).

[89] L. Ricci *et al.* “A Compact Grating-Stabilized Diode Laser System for Atomic Physics”. Optics Communications **117,** 541–549 (1995).

[90] E. C. Cook, P. J. Martin, T. L. Brown-Heft, J. C. Garman, and D. A. Steck. “High Passive-Stability Diode-Laser Design for Use in Atomic-Physics Experiments”. Review of Scientific Instruments **83,** 043101 (2012).

[91] K. B. MacAdam, A. Steinbach, and C. Wieman. “A Narrow-band Tunable Diode Laser System with Grating Feedback, and a Saturated Absorption Spectrometer for Cs and Rb”. American Journal of Physics **60,** 1098–1111 (1992).

[92] W. Demtröder. *Laser Spectroscopy 2: Experimental Techniques* 5th ed. (Springer, Berlin, Heidelberg, 2015).

[93] G. Genov, T. E. Lellinger, T. Halfmann, and T. Peters. “Laser Frequency Stabilization by Bichromatic Saturation Absorption Spectroscopy”. Journal of the Optical Society of America B **34,** 2018–2030 (2017).

[94] R. W. P. Drever *et al.* “Laser Phase and Frequency Stabilization Using an Optical Resonator”. Applied Physics B **31,** 97–105 (1983).

[95] E. D. Black. “An Introduction to Pound–Drever–Hall Laser Frequency Stabilization”. American Journal of Physics **69,** 79–87 (2001).

[96] S. C. Bell, D. M. Heywood, J. D. White, J. D. Close, and R. E. Scholten. “Laser Frequency Offset Locking Using Electromagnetically Induced Transparency”. Applied Physics Letters **90,** 171120 (2007).

[97] A. Korpel. “Acousto-Optics—A Review of Fundamentals”. Proceedings of the IEEE **69,** 48–53 (1981).

[98] E. A. Donley, T. P. Heavner, F. Levi, M. O. Tataw, and S. R. Jefferts. “Double-Pass Acousto-Optic Modulator System”. Review of Scientific Instruments **76,** 063112 (2005).

[99] W. J. Schwenger and J. M. Higbie. “High-Speed Acousto-Optic Shutter with No Optical Frequency Shift”. Review of Scientific Instruments **83,** 083110 (2012).

[100] H. J. Metcalf and P. van der Straten. *Laser Cooling and Trapping* (Springer, New York, 1999).

[101] T. M. Brzozowski, M. Maczynska, M. Zawada, J. Zachorowski, and W. Gawlik. “Time-of-Flight Measurement of the Temperature of Cold Atoms for Short Trap-Probe Beam Distances”. Journal of Optics B: Quantum and Semiclassical Optics **4,** 62 (2002).

[102] W. Ketterle, K. B. Davis, M. A. Joffe, A. Martin, and D. E. Pritchard. “High Densities of Cold Atoms in a Dark Spontaneous-Force Optical Trap”. Physical Review Letters **70,** 2253–2256 (1993).

[103] M. H. Anderson, W. Petrich, J. R. Ensher, and E. A. Cornell. “Reduction of Light-Assisted Collisional Loss Rate from a Low-Pressure Vapor-Cell Trap”. Physical Review A **50,** R3597–R3600 (1994).

[104] R. Grimm, M. Weidemüller, and Y. B. Ovchinnikov. “Optical Dipole Traps for Neutral Atoms”. Advances in Atomic, Molecular, and Optical Physics **42,** 95–170 (2000).

[105] J. A. West, C. M. Smith, N. F. Borrelli, D. C. Allan, and K. W. Koch. “Surface Modes in Air-Core Photonic Band-Gap Fibers”. Optics Express **12,** 1485–1496 (2004).

[106] T. A. Savard, K. M. O’Hara, and J. E. Thomas. “Laser-Noise-Induced Heating in Far-off Resonance Optical Traps”. Physical Review A **56,** R1095–R1098 (1997).

[107] T. Peyronel *et al.* “Switching and Counting With Atomic Vapors in Photonic-Crystal Fibers”. IEEE Journal of Selected Topics in Quantum Electronics **18,** 1747–1753 (2012).

[108] R. Sulzbach, T. Peters, and R. Walser. “Optimal Pulse Propagation in an Inhomogeneously Gas-Filled Hollow-Core Fiber”. Physical Review A **100,** 013847 (2019).

[109] S. Friebel, C. D’Andrea, J. Walz, M. Weitz, and T. W. Hänsch. “CO2-laser Optical Lattice with Cold Rubidium Atoms”. Physical Review A **57,** R20–R23 (1998).

[110] Y.-C. Chen, Y.-A. Liao, L. Hsu, and I. A. Yu. “Simple Technique for Directly and Accurately Measuring the Number of Atoms in a Magneto-Optical Trap”. Physical Review A **64,** 031401 (2001).

[111] S. Ghosh *et al.* “Low-Light-Level Optical Interactions with Rubidium Vapor in a Photonic Band-Gap Fiber”. Physical Review Letters **97,** 023603 (2006).

[112] T. Peters, Y.-H. Chen, J.-S. Wang, Y.-W. Lin, and I. A. Yu. "Optimizing the Retrieval Efficiency of Stored Light Pulses". Optics Express **17,** 6665–6675 (2009).

[113] M. Hain. "EIT Light Storage of Weak Coherent Pulses in a Doped Solid". Dissertation, TU Darmstadt (2021).

[114] P. Palittapongarnpim, A. MacRae, and A. I. Lvovsky. "Note: A Monolithic Filter Cavity for Experiments in Quantum Optics". Review of Scientific Instruments **83,** 066101 (2012).

[115] A. Ahlrichs, C. Berkemeier, B. Sprenger, and O. Benson. "A Monolithic Polarization-Independent Frequency-Filter System for Filtering of Photon Pairs". Applied Physics Letters **103,** 241110 (2013).

[116] W. Demtröder. *Laserspektroskopie: Grundlagen und Techniken* (Springer, Berlin, Heidelberg, 2007).

[117] B. Albrecht, P. Farrera, G. Heinze, M. Cristiani, and H. de Riedmatten. "Controlled Rephasing of Single Collective Spin Excitations in a Cold Atomic Quantum Memory". Physical Review Letters **115,** 160501 (2015).

[118] S. Fasel *et al.* "High-Quality Asynchronous Heralded Single-Photon Source at Telecom Wavelength". New Journal of Physics **6,** 163–163 (2004).

[119] A. Seri *et al.* "Laser-Written Integrated Platform for Quantum Storage of Heralded Single Photons". Optica **5,** 934–941 (2018).

[120] L. Zhao *et al.* "Shaping the Biphoton Temporal Waveform with Spatial Light Modulation". Physical Review Letters **115,** 193601 (2015).

[121] D. Rieländer, A. Lenhard, M. Mazzera, and H. de Riedmatten. "Cavity Enhanced Telecom Heralded Single Photons for Spin-Wave Solid State Quantum Memories". New Journal of Physics **18,** 123013 (2016).

[122] M. Gündoğan, P. M. Ledingham, K. Kutluer, M. Mazzera, and H. de Riedmatten. "Solid State Spin-Wave Quantum Memory for Time-Bin Qubits". Physical Review Letters **114,** 230501 (2015).

[123] J. Guo *et al.* "High-Performance Raman Quantum Memory with Optimal Control in Room Temperature Atoms". Nature Communications **10,** 148 (2019).

[124] E. Saglamyurek, T. Hrushevskyi, A. Rastogi, K. Heshami, and L. J. LeBlanc. "Coherent Storage and Manipulation of Broadband Photons via Dynamically Controlled Autler–Townes Splitting". Nature Photonics **12,** 774–782 (2018).

[125] M. Hain, M. Stabel, and T. Halfmann. "Few-Photon Storage on a Second Timescale by Electromagnetically Induced Transparency in a Doped Solid". New Journal of Physics **24,** 023012 (2022).

[126] C. W. Chou, S. V. Polyakov, A. Kuzmich, and H. J. Kimble. "Single-Photon Generation from Stored Excitation in an Atomic Ensemble". Physical Review Letters **92,** 213601 (2004).

[127] A. Hilton, C. Perrella, A. Luiten, and P. Light. “Dual-Color Magic-Wavelength Trap for Suppression of Light Shifts in Atoms”. Physical Review Applied **11,** 024065 (2019).

[128] T. Yoon and M. Bajcsy. “Laser-Cooled Cesium Atoms Confined with a Magic-Wavelength Dipole Trap inside a Hollow-Core Photonic-Bandgap Fiber”. Physical Review A **99,** 023415 (2019).

[129] R. A. Maruf and M. Bajcsy. “On-Chip Splicer for Coupling Light between Photonic Crystal and Solid-Core Fibers”. Applied Optics **56,** 4680–4684 (2017).

[130] Y. Wang *et al.* “Enhancing Fiber Atom Interferometer by In-Fiber Laser Cooling”. Physical Review Research **4,** L022058 (2022).

[131] N. Skribanowitz, I. P. Herman, J. C. MacGillivray, and M. S. Feld. “Observation of Dicke Superradiance in Optically Pumped HF Gas”. Physical Review Letters **30,** 309–312 (1973).

[132] R. W. Hellwarth. “Theory of Stimulated Raman Scattering”. Physical Review **130,** 1850–1852 (1963).

[133] S. Okaba, D. Yu, L. Vincetti, F. Benabid, and H. Katori. “Superradiance from Lattice-Confined Atoms inside Hollow Core Fibre”. Communications Physics **2,** 1–10 (2019).

[134] D. J. Heinzen, J. E. Thomas, and M. S. Feld. “Coherent Ringing in Superfluorescence”. Physical Review Letters **54,** 677–680 (1985).

[135] D. Polder, M. F. H. Schuurmans, and Q. H. F. Vrehen. “Superfluorescence: Quantum-mechanical Derivation of Maxwell-Bloch Description with Fluctuating Field Source”. Physical Review A **19,** 1192–1203 (1979).

[136] F. T. Arecchi and E. Courtens. “Cooperative Phenomena in Resonant Electromagnetic Propagation”. Physical Review A **2,** 1730–1737 (1970).

[137] J. Stenzel. “Setup for Frequency Conversion of Single Photons in a PPLN-Waveguide, Driven by an OPO”. Master’s Thesis, TU Darmstadt (2021).

[138] L. V. Blake. “A Modified Simpson’s Rule and Fortran Subroutine for Cumulative Numerical Integration of a Function Defined by Data Points”. Technical Report, Defense Technical Information Center, Fort Belvoir (1971).

[139] P. P. Rohde and T. C. Ralph. “Modelling Photo-Detectors in Quantum Optics”. Journal of Modern Optics **53,** 1589–1603 (2006).

[140] O. A. Ivanova, T. S. Iskhakov, A. N. Penin, and M. V. Chekhova. “Multiphoton Correlations in Parametric Down-Conversion and Their Measurement in the Pulsed Regime”. Quantum Electronics **36,** 951 (2006).

[141] K. J. Kemp *et al.* “Optical-Depth Scaling of Light Scattering from a Dense and Cold Atomic 87Rb Gas”. Physical Review A **101,** 033832 (2020).

[142] R. W. Boyd. *Nonlinear Optics* 4th ed. (Academic Press, Amsterdam, Boston, 2020).

Publications and Contributions to Conferences

Work directly related to this Dissertation

Publications in Peer-Reviewed Journals

- A. Bruns, C.-Y. Hsu, S. Stryzhenko, E. Giese, L. Yatsenko, I. Yu, T. Halfmann, and T. Peters.
  Ultrabright and Narrowband Intra-Fiber Biphoton Source at Ultralow Pump Power.
  Quantum Science and Technology **8**, 015002 (2023)

Manuscripts in Preparation

- S. Stryzhenko, A. Bruns, T. Halfmann, L. Yatsenko, and T. Peters.
  Scaling of Large Sample Superfluorescence in Inhomogeneous Ensembles.

Contributions to National and International Conferences

- A. Bruns, C.-Y. Hsu, S. Stryzhenko, E. Giese, L. Yatsenko, I. Yu, T. Halfmann, and T. Peters.
  Bright and Narrowband Intra-Fiber Biphoton Source at Low Pump Power.
  Talk at CAMEL (Nessebar, Bulgaria, 2023)
- A. Bruns, C.-Y. Hsu, S. Stryzhenko, E. Giese, L. Yatsenko, I. Yu, T. Halfmann, and T. Peters.
  Ultrabright and Narrowband Intra-Fiber Biphoton Source at Ultralow Pump Power.
  Talk at DPG Frühjahrstagung SAMOP (Hannover, Germany, 2023)
- A. Bruns, C.-Y. Hsu, S. Stryzhenko, L. Yatsenko, I. Yu, T. Halfmann, and T. Peters.
  Narrowband Biphoton Source of Maximal Spectral Brightness at Ultralow Pump Power.
  Poster at ICAP (Toronto, Canada, 2022)

Further Work not directly related to this Dissertation

Publications in Peer-Reviewed Journals

- A. Bruns, G. T. Genov, M. Hain, N. V. Vitanov and T. Halfmann.
  Experimental Demonstration of Composite Stimulated Raman Adiabatic Passage.
  Physical Review A **98**, 053413 (2018)

Contributions to National and International Conferences

- T. Peters, T.-P. Wang, A. Neumann, L. S. Simeonov, A. Bruns, and T. Halfmann.
  Stopped and Stationary Light at the Single-Photon Level inside a Hollow-Core Fiber.
  Poster at DPG Herbsttagung (Freiburg, Germany, 2019)
- A. Bruns, G. T. Genov, M. Hain and T. Halfmann.
  Experimental Demonstration of Composite Stimulated Raman Adiabatic Passage.
  Poster at ICAP (Barcelona, Spain, 2018)
- A. Bruns, G. T. Genov, M. Hain and T. Halfmann.
  Experimental Demonstration of Composite Stimulated Raman Adiabatic Passage.
  Poster at DPG QUANET Seminar (Bad Honef, Germany, 2018)
- A. Bruns, G. T. Genov, M. Hain, N. V. Vitanov and T. Halfmann.
  Experimental Demonstration of Composite Stimulated Raman Adiabatic Passage.
  Talk at Rare Earth Ion Workshop (Karlsruhe, Germany, 2017)

Supervisions and Contributions to Teaching

Master's Projects

- Jakob Stenzel. *Setup for Frequency Conversion of Single Photons in a PPLN-Waveguide, driven by an OPO*. (2021)

Bachelor's Projects

- Viet Hoang. *Erhöhung der Photonenrate durch dynamische Sequenzen an einer DLCZ Einzelphotonenquelle*. (2020)
- Jonas Moos. *Aktive Magnetfeldstabilisierung im Milligaußbereich für quantenoptische Experimente*. (2020)

Laboratory Courses and Internships

- Supervision of Laboratory Internship (*Miniforschungen*)
  - Lisa Kaul. *Aufbau und Charakterisierung eines durchstimmbaren Etalons*. (2021)
  - Tobias Neumann. *Temperaturstabilisierung an einem optisch parametrischen Oszillator*. (2022)
- Supervision of Basic Laboratory Courses
  - Electricity: *Elektrostatische Felder, Millikan-Versuch* (SS2015)
  - Mechanics: *Fallbeschleunigung, Elastischer Stoß* (SS2014)

Contributions to Teaching

- Supervision of the talk *Frequenzstabilisierung von Lasersystemen* in the seminar *Laserphysik & Lasertechnologie*. (2020)
- Supervision of Exercise Groups
  - *Physik I* (SS 2017)
  - *Moderne Optik* (WS2016/17)
  - *Computational Physics* (SS2016)
  - *Physik III* (WS2015/16)
  - *Physik II* (SS15)
  - *Physik I* (WS2014/15)
  - *Naturwissenschaften II* (SS2013)
- Labtours (2017-2023)

Erklärungen laut Promotionsordnung

§8 Abs. 1 lit. c PromO
Ich versichere hiermit, dass die elektronische Version meiner Dissertation mit der schriftlichen Version übereinstimmt.

§8 Abs. 1 lit. d PromO
Ich versichere hiermit, dass zu einem vorherigen Zeitpunkt noch keine Promotion versucht wurde.

§9 Abs. 1 PromO
Ich versichere hiermit, dass die vorliegende Dissertation selbstständig und nur unter Verwendung der angegebenen Quellen verfasst wurde.

§9 Abs. 2 PromO
Die Arbeit hat bisher noch nicht zu Prüfungszwecken gedient.

Darmstadt, 16. Juni 2023

_____
(Alexander Bruns)